Black Hole Greybody Factors in a Non-commutative Space-time

by

Zachary Kirk Arthur Taylor Cox

A thesis submitted in partial fulfillment of the requirements for the degree of

Master of Science

Department of Physics

University of Alberta

Abstract

Non-commutative geometries motivated by string theory have enabled calculations of black hole properties distinctly different from those of classical gravity, such as a finite maximum temperature and a minimum mass, and horizon radius at which Hawking evaporation may terminate. In this thesis, we investigate the greybody factors arising from higher dimensional spherically symmetric and static black holes in non-commutative geometry inspired space-times.

Greybody factors are computed for massless fields of spin 0, 1/2, 1 and 2 on the brane, and spin 0 and 2 in the bulk emitted from higher dimensional non-commutative geometry inspired black holes. The results are compared to the commutative cases. The Teukolsky equation describing the various field perturbations is decoupled into angular and radial parts. The radial equation is cast into the form of a one-dimensional Schrödinger-like equation with an effective short-ranged potential barrier. We use the product calculus formalism of path-ordered exponentials to numerically compute the transmission coefficients. The corresponding absorption cross sections and emission spectra are also presented. The results presented here will be useful in Monte Carlo simulations required for searches of microscopic non-commutative black holes produced in proton-proton collisions, such as those with the ATLAS and CMS experiments at the Large Hadron Collider.

Preface

The work presented in this thesis is the author's own, unless otherwise denoted by citation. The work presented in Chapter 4 and Appendix C was published in Ref. [1] in collaboration with Doug Gingrich.

Acknowledgements

I would like to express my sincere appreciation to my supervisor Doug Gingrich for the opportunity to work on this project and for his invaluable mentorship over the past year. His patient supervision, guidance, and many insightful discussions have been essential in shaping this research.

I am also extremely grateful to Peichun Amy Tsai for providing me with many amazing research opportunities, and supporting me throughout my academic career.

Finally, I would like to thank my family and friends for their continuous support and encouragement. To my Mom, Dad, and Julien, your support means everything to me. Thank you for always being there.

Table of Contents

List of Tables

List of Figures

Chapter 1

Introduction

1.1 Black Holes

A black hole is a region of space characterized by an event horizon, beyond which nothing can escape due to the extreme curvature of the space-time. Laplace was one of the first to predict the concept of a black hole in the eighteenth century using only Newtonian mechanics [2]. Laplace used the term non-luminous bodies, referring to the idea that gravity could prevent light from escaping an object sufficiently dense such that the escape velocity at its surface exceeds the speed of light [2]. In 1915 Albert Einstein published his theory of general relativity which transformed our understanding of gravity. In 1916, Karl Schwarzschild found the first vacuum solution to the Einstein field equations describing the space-time surrounding a spherically symmetric and static point-like mass, now commonly referred to as the Schwarzschild solution [3]. The Schwarzschild solution predicts the existence of a black hole for objects whose radius is smaller than some critical radius known as the horizon radius. Remarkably, the definition given by Laplace for the radius of his non-luminous bodies is the same as that found by Schwarzschild for a static and spherically symmetric black hole.

In four dimensions, it is well known that the space-time surrounding a black hole according to general relativity is uniquely defined in terms of its mass M, charge Q, and angular momentum J. This is referred to as the no hair theorem, with

the hair being other independent characteristics [4]. The Schwarzschild solution is the case for $Q = J = 0$. A black hole with charge Q is defined by the Reissner-Nordström solution and a black hole with angular momentum J is described by the Kerr solution. The Kerr-Newman solution describes a black hole with both charge and angular momentum.

The Schwarzschild solution contains two singularities, with one being a coordinate singularity at the horizon which can be removed through a change of coordinates. The second singularity is a true singularity at the centre of the black hole where the curvature, or Ricci scalar goes to infinity. According to general relativity, this singularity is also thought to contain the entire mass of the black hole. In a static black hole, the singularity is a point singularity, while the singularity of a rotating back hole is smeared out to form a ring singularity which lies in the plane of rotation. The appearance of these singularities is often interpreted as indicators of the breakdown of the theory. This breakdown is indeed expected, since it occurs in regions where the energy density approaches the Planck density and a quantum mechanical description is required. The singularity is really just a region where the radius of curvature is of the order of the Planck length [5]. Hawking theorized that the matter that enters this region might reemerge in another universe [5]. To date, there is no such theory capable of unifying quantum mechanics with a theory of gravity, though a complete theory of quantum gravity is not expected to contain singularities. Among others, two major areas of research which attempt to resolve this problem are string theories which incorporate extra spatial dimensions, and loop quantum gravity. Both are rooted in the idea that there exists a minimum length scale. While such theories are mathematically very rich, direct experimental support has proven difficult to obtain. This is due to the fact that we don't yet have the means to peer into the high energy scales at which quantum gravity effects start to become significant. The revival of the idea of the existence of extra space-like dimensions at the turn of the twenty-first century allows for the possibility to significantly lower the fundamental scale of

quantum gravity. This led to the idea that microscopic black holes could be produced in high energy particle collisions at the Large Hadron Collider (LHC) or in the Earth's atmosphere [6].

1.2 Gravity in Higher Dimensions

One of the motivations for considering models which incorporate extra spatial dimensions is the hierarchy problem. The hierarchy problem is an underlying question with regard to our modern understanding of physics, reflective of the idea that a complete model of particle physics should have a common energy scale. There are different versions of the hierarchy problem, however perhaps most relevant to us is the so-called aesthetic hierarchy problem which compares two fundamental energy scales: the Planck scale and the electroweak scale. It is not understood why the Planck scale $M_P \sim 10^{16}$ TeV, the scale at which gravitational interactions become strong, is so many orders of magnitude higher than the electroweak scale ~ 0.1 TeV [7].

Models of higher dimensions attempt to resolve this matter by postulating that the apparent weakness of gravity is due to the presence of extra spatial dimensions. In such models, the hypothetical graviton is generally allowed to propagate in the full $(4 + n)$-dimensional space-time, otherwise known as the bulk, where n is the number of extra spatial dimensions. All standard model fields are constrained to the 4-dimensional brane which avoids contradictions with precise particle physics measurements. Since the gravitational force may propagate in the full higher dimensional space-time, its strength is effectively diluted on the brane, resulting in gravity appearing weaker than the other standard model forces which only propagate on the brane. In this thesis, we will focus on the Arkani-Dimopoulos-Dvali (ADD) model of large extra dimensions [8], in which the extra dimensions are flat and toroidally compactified with a compactification radius R. The compactification radius is typically considered to be large when compared to the Planck length but small enough such that it agrees with limits from searches for deviations from Newton's law.

In the context of higher dimensions, the Planck scale becomes an effective scale as seen on the brane, and is related to the higher D-dimensional Planck scale, M_D, which is defined by the Particle Data Group as [9]

$$M_P^2 = M_D^{n+2} R^n. \tag{1.1}$$

Here, and throughout the remainder of this thesis, a system of units will be used such that $\hbar = c = k_B = G = 1$, as well as the metric signature $(-+++)$ unless otherwise specified. We use the Particle Data Group definition of the higher dimensional Planck scale since this is usually the quantity that high energy particle physics experiments set limits on [9]. We note that $M_*^{n+2} = 8\pi/(2\pi)^n M_D^{n+2}$ is sometimes used in literature. The particular choice of convention used to define the higher dimensional Planck scale can have a significant impact on computations. For example, it was shown in Ref. [10] that the choice of definition of the higher dimensional Planck scale leads to different n-dependencies of the proton-proton black hole production cross section. Therefore we expect that some results presented in this thesis may be dependent on our particular choice of convention for the higher dimensional Planck scale M_D.

Setting M_D near the electroweak scale at around $\sim$ 1 TeV allows us to make predictions for R using Eq. (1.1) as shown in Table 1.1.

Table 1.1: Estimation of the compactification radii R versus the number of extra dimensions n for $M_D \sim 1$ TeV.

n	R [m]
1	10^{11}
2	10^{-3}
3	10^{-8}
4	10^{-11}
5	10^{-12}
6	10^{-13}
7	10^{-14}

The possibility of a single extra dimension is ruled out based on the grounds that the compactification radius is on the order of the distance from the Earth to the Sun

which would lead to observable modifications of Newtons law [9]. For $n \geq 2$ we find that $R < 1$ mm and thus are not ruled out [9]. Evidence of extra dimensions of space can be obtained by looking for events with missing energy arising from gravitons escaping into the bulk. Results from accelerator experiments and searches for deviations from Newton's law have set lower bounds on M_D [9]. Nevertheless, the possibility of a lower fundamental energy scale in the ADD model provides the possibility to probe the quantum nature of black holes at energies accessible to current particle physics experiments. As a result, the possible production and decay of microscopic black holes at the LHC or in the Earth's atmosphere would offer insight into the nature of a quantum theory of gravity. Such black holes are expected to decay through the emission of Hawking radiation which may be detected by particle detectors at the LHC or the Fermi Gamma-ray Space Telescope [11]. We will describe in detail the Hawking radiation process in the next section.

In this thesis we will assume that the black hole horizon radius is much smaller than the compactification radius so that the physics is not sensitive to the finite size of the compactified dimensions [12]. In addition we use the probe-brane approximation [6] where we neglect the gravitational field produced by the brane. In this case, the only effect of the brane field is to bind the black hole to the brane, and the black hole may be treated as an isolated object where the centre of the black hole coincides with the world sheet of the brane and extends into the higher dimensions [13, 14]. A schematic of this scenario is shown in Figure 1.1 which is reproduced from Ref. [6].

We note that we also ignore the possibility for the black hole to escape the brane via the recoil effect [15]. The emission of gravitons into the bulk may cause the black hole to recoil into the bulk if there is no symmetry which suppresses the recoil [15]. By making the probe-brane approximation we ignore the possibility for the black hole to recoil into the bulk. In summary, we are interested in black holes with mass greater than the Planck mass but with a horizon radius smaller than the compactification radius. These conditions are generally satisfied when considering black holes produced

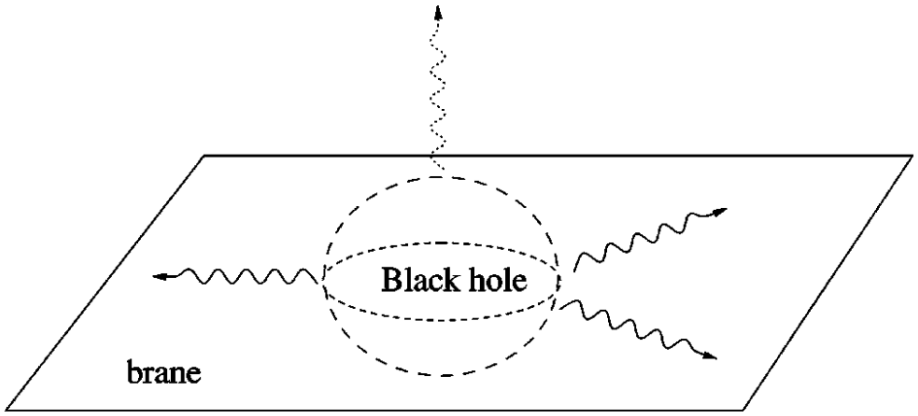

Figure 1.1: Schematic of a D-dimensional black hole bound to the 4-dimensional brane and extending into the higher dimensions. Standard model fields (solid lines) are restricted to propagate on the brane while the graviton (dashed line) may propagate in the full higher dimensional bulk. Image reproduced from Ref. [6].

at the LHC [6].

In general, the horizons of black holes in extra dimensional space-times do not need to be spherical, and thus more complicated black hole like objects may arise [16]. In this thesis, we consider only black holes with a spherical event horizon topology.

1.3 Hawking Radiation

A consequence of applying quantum mechanics to a static black hole background is that black holes may emit thermal radiation like a blackbody. The idea that black holes emit radiation was first proposed by Stephen Hawking in 1974 [17]. Hawking showed through a series of papers [5, 17] that black holes behave as thermal systems, with a characteristic temperature, $T_{\rm H}$ proportional to their surface gravity. The explicit definition of this temperature will be provided in later sections.

Treating black holes as thermal systems, Hawking proposed that black holes should emit radiation with a characteristic blackbody spectrum dependent on their temperature. This is counter-intuitive, since using the argument that nothing, not even light can escape black holes might suggest that black holes should only grow as matter falls into their event horizon. However, Hawking showed that such radiation is

possible by taking into account quantum mechanical effects at the horizon. In Hawking's analogy [17], the mechanism by which this occurs is through the production of particle/anti-particle pairs by the gravitational field at the horizon. Due to the geometry of space-time near the horizon, these particle pairs can become separated with one falling into the black hole and one escaping from it, leading to a net decrease in mass [7]. This phenomenon is now known as Hawking radiation. Hawking radiation may also be described as a tunneling process, for which we refer the reader to Ref. [18] for further details. For an observer at the event horizon, Hawking showed that the emission spectrum of a static, uncharged and spherically symmetric black hole is that of a blackbody.

The space-time surrounding a black hole acts as a potential barrier which effectively filters the radiation escaping from the black hole. A fraction will penetrate through the barrier and escape to infinity which will constitute the thermal emission seen by an observer at spatial infinity [5]. The remaining particles will be reflected by the potential barrier and cross the horizon. Consequently, an observer at spatial infinity from the black hole will measure a different emission spectrum than one at the horizon by a factor $\Gamma_{s,\ell}(M;\omega)$ called the greybody factor. The greybody factor for a given spin s and angular momentum quantum number ℓ, is in general dependent on the frequency ω, and represents the probability of a particle to escape from the horizon to spatial infinity. As such, the blackbody spectrum of the black hole is modified by the greybody factor.

The flux of radiation leaving the black hole will cause a net decrease in the mass of the black hole, and so the black hole will not be a stationary state. Hawking addresses this by considering a quasi-stationary approach where after the emission of a particle, the black hole is allowed to reach equilibrium at a new temperature before the emission of subsequent particles [5]. Hawking argued that as long as the mass of the black hole is large in comparison to the Planck mass, the rate of particle emission will be slow such that it is reasonable to approximate the black hole to be in

a quasi-stationary state when performing calculations. When the mass of the black hole is near the Planck mass, the quasi-stationary approximation will break down and one cannot use the classical arguments of general relativity [5]. This is due to the fact we are using a semi-classical description of gravity. The description of the spacetime surrounding the black hole is a classical theory as described by Einsteins theory of general relativity. However the process of Hawking radiation considers quantum fields propagating on a static black hole background. Therefore any dynamical changes in the metric due to the propagation of quantum fields is not taken into consideration. Hence we are ignoring the back reaction of the quantum fields on the space-time. A complete theory of quantum gravity would be necessary to consider the complete dynamical system.

Detection of Hawking radiation is of considerable interest as it may carry information about the nature of quantum gravity. Unfortunately, detection of Hawking radiation from astronomical black holes, such as Sagittarius A* at the centre of the Milky Way has proven difficult since black holes of astronomical scale are relatively cold. Indeed the emitted radiation is found to increase with a rise in temperature, or as we will show in later sections a decrease in mass. As a result, Hawking radiation from astronomical black holes is negligible when compared to the background radiation such as that coming from their accretion discs [19].

Primordial black holes (PBHs) are black holes theorized to have formed in the early stages of the universe at the end of the inflation era [20]. Unlike stellar black holes which form from the collapse of stars, PBHs may exist which are smaller, hotter and thus may prove more promising candidates for emitting detectable Hawking radiation. In addition, PBHs have attracted considerable interest as dark matter candidates as their mass density can contribute to the missing dark matter energy density of the universe [20]. Still, the detection of such black holes has not been possible, and the lack of evidence has placed constraints on the lower mass range. For example, isolated PBHs with an initial mass of an asteroid would be currently nearing the end of their

life, evaporating away through Hawking radiation, while smaller PBHs would have already evaporated away [19]. A thorough investigation of the evaporation of PBHs through Hawking radiation is presented in Ref. [19].

The LHC, which began operation in 2008, has provided the exciting possibility of producing microscopic black holes from high energy proton collisions. For a black hole to be produced at the LHC, the impact parameter of a collision between two particles with centre of mass energy $\sqrt{s}$ must be smaller than the horizon radius [7]. If the fundamental Planck scale is on the order of $\sim$ 1 TeV, which is allowed in some theories incorporating extra spatial dimensions as discussed in Section 1.2, the centre of mass energy reached at the LHC of $\sqrt{s} = 14$ TeV would be large enough to produce classical black holes [6]. The decay of classical black holes produced at the LHC would be governed by the emission of Hawking radiation which is generally described by the following process [6]. The first stage after the formation of the black hole is the balding phase, in which the black hole emits mostly gravitational radiation, while shedding any asymmetries inherited during the production process [7]. It then enters a spin-down phase where the black hole loses angular momentum, mass and charge through Hawking radiation. After losing most of its angular momentum and charge, the black hole enters the Schwarzschild phase where it loses mass through Hawking radiation. The Schwarzschild phase continues until the mass of the black hole approaches the Planck mass. At this point, a theory of quantum gravity is needed to explain the final stage of the black hole.

Although a complete theory of quantum gravity has not yet been realized, we may be able to probe some phenomenological aspects by postulating a non-commutative geometry.

1.4 Arrangement of Thesis

The aim of this thesis will be to extend the results of Ref. [11] to calculate the greybody factors for all spin fields from higher dimensional non-commutative black holes. The

results presented here may be of use in Monte Carlo simulations at the LHC or future colliders in searches for microscopic non-commutative geometry inspired black holes. Chapter 2 introduces some of the aspects of non-commutative geometries relevant for the computation of greybody factors. In Chapter 3, we give an overview of the theoretical framework required to compute greybody factors, as well as the numerical techniques. In Chapter 4 we present the greybody factors, absorption cross sections, and emission spectra for various massless spin fields on the brane from higher dimensional non-commutative geometry inspired black holes. Much of the work in Chapter 4 has been published in Ref. [1] in collaboration with Doug Gingrich. In Chapter 5 we present the greybody factors, absorption cross sections, and emission spectra for spin 0 and 2 massless fields in the bulk from higher dimensional non-commutative inspired black holes for the first time. In Chapter 6 we summarize our key results and provide some possible directions for future work.

Chapter 2

Aspects of Non-commutative Geometry

In this section we will introduce the formalism of non-commutative geometry, and briefly introduce some of the developments of non-commutative geometry in general relativity. There is a vast amount of literature concerning non-commutative geometry, however it is still a developing field. We do not hope to provide a complete overview of the literature, only to introduce the basic relations necessary to compute black hole greybody factors. To do so, we would ideally like to construct a non-commutative equivalent of general relativity, however no such theory exists as of yet. As we will show below, we can approximate the effect of non-commutativity by considering the average effect of non-commutative fluctuations and the corresponding modifications to the metric [11]. We will begin by introducing some basic commutation relations, and describe how non-commutative geometry is implemented in quantum field theory. Then we will cover some of the developments of non-commutative geometry as applied to general relativity and discuss some properties of non-commutative geometry inspired black holes.

2.1 Incompatible Observables

It is important that we understand some basic properties of commutative operations before we dive in to the properties of non-commutative geometries. In mathematics,

an operation is said to be commutative if the order of the operands does not matter. Addition and multiplication of two numbers are perhaps some of the most elementary examples of commutative operations. Multiplication of two numbers say A and B, gives the same results no matter the order in which you multiply them. Thus multiplication of two numbers is said to be a commutative operation. However the same cannot be said about division, A/B is in general not equal to B/A. Thus we conclude that division is not a commutative operation. Another example of a non-commutative operation are rotations in three or higher dimensional space.

In quantum mechanics, physical observables A, B become operators $\hat{A}, \hat{B}$. An observable $\hat{A}$ in some state has an associated expectation (mean) value $\langle \hat{A} \rangle$. Attempting to measure two physical observables in a state simultaneously leads to a generalized uncertainty principle given in terms of the commutator $\left[\hat{A}, \hat{B}\right] = \hat{A}\hat{B} - \hat{B}\hat{A}$ and

$$\sigma_A \sigma_B \geq \left| \frac{1}{2i} \langle [\hat{A}, \hat{B}] \rangle \right|, \tag{2.1}$$

where $\sigma_A = \sqrt{\langle \hat{A}^2 \rangle - \langle \hat{A}^2 \rangle^2}$ is the standard deviation which is a measure of the uncertainty, or lack of knowledge about a particular quantity. If two observables commute, then they are said to be compatible variables, which means they can be measured simultaneously. If two observables do not commute, they are said to be incompatible or conjugate variables. Incompatible observables cannot be measured simultaneously with certainty as described by the uncertainty principle. The classic example of two such observables are position, $\hat{x}$ and momentum, $\hat{p}$, which leads to the canonical commutation relation

$$[\hat{x_i}, \hat{p_j}] = i\delta_{ij}. \tag{2.2}$$

It has been argued that at the Planck scale, the fundamental assumption of locality may not hold, and a similar commutation relation between the position operators may arise [21]. The momentum and energy required to make a measurement near the Planck scale would itself modify the geometry, and one might expect there to

be a commutation relation preventing measurements of position to accuracy's better than the Planck length [22]. In both general relativity and quantum field theories, space is defined to be commutative. Theories of quantum gravity, such as string theory and loop quantum gravity propose the idea of a quantized space-time. Non-commutative geometries were first investigated by Snyder [23] in 1947, concerning the quantization of space-time. This idea was for the most part set aside until the mathematics community developed the idea of non-commutative geometry in the 80's as a generalization of differential geometry [22, 24], and became of particular interest to physicists after Seiberg and Witten showed that string theory reduces to a quantum field theory on a non-commutative space [25]. In particular, the coordinate endpoints of open strings ending on D-branes become non-commutative [26].

2.2 Non-commutativity in Quantum Field Theory

The general idea in non-commutative quantum field theory is that the space-time coordinates, which are now thought of as operators, fail to commute [27]. There are different representations of non-commutativity used throughout literature [28]. Here we introduce the simplest type: canonical non-commutativity by imposing the following commutation relation in D-dimensional space-time

$$[\hat{x}^A, \hat{x}^B] = i\theta^{AB}, \tag{2.3}$$

where θ^{AB} is a real anti-symmetric $D \times D$ matrix (not a tensor). To avoid issues with causality and unitarity we only consider non-commutativity between spatial coordinates, hence the elements corresponding to time are set to zero [29]. It is convenient to write θ^{AB} in the following form

$$\theta^{AB} = \frac{\epsilon^{AB}}{\Lambda_{NC}^2}, \tag{2.4}$$

to separate the mass scale Λ_{NC} which has units of inverse length from the dimensionless matrix ϵ^{AB}. Here we have taken Λ_{NC}^{-2} to be an average magnitude of the elements

of θ^{AB} and thus assume that elements of ϵ^{AB} are of $\mathcal{O}(1)$ [27]. We further define the non-commutative parameter $\theta = \Lambda_{NC}^{-2}$ which has units of length squared.

We can think of the above commutation relation as introducing a fuzziness into our coordinates. The matrix θ^{AB} represents the fundamental discretization of space-time, similar to how $\hbar$ represents the discretization of phase-space in quantum mechanics [22]. The notion of a point in non-commutative space is no longer meaningful as there is an inherent uncertainty in the position with respect to more than one coordinate. In analogy to how the position-momentum commutator in Eq. (2.2) leads to the canonical uncertainty principle, we can write a similar relation for the coordinate-coordinate uncertainty [22]

$$\sigma_{\hat{x}_A}\sigma_{\hat{x}_B} \geq \frac{1}{2}|\theta_{AB}|. \tag{2.5}$$

It is argued that the loss of resolution described by the above relation can be interpreted as an effective ultraviolet cutoff [30].

Intuitively, one may associate the non-commutative scale with the Planck scale, however we stress here that the the non-commutative scale is not the Planck scale. The idea is that Λ_{NC} is a new scale that may be greater than the Planck scale where one may observe the effects of non-commutativity [11, 27]. However throughout the remainder of this thesis and to allow comparisons with literature, we will take the common values $M_D \sim \sqrt{\theta}^{-1} \sim 1$. For $n = 0$, the units are $M_D \sim 10^{16}$ TeV and $\sqrt{\theta} \sim 10^{-35}$ m. For $n > 0$, units can be chosen as $M_D \sim 1$ TeV and $\sqrt{\theta} \sim 10^{-4}$ fm.

It has been shown to be rather difficult to perform explicit computations when working directly with non-commutative coordinates [31]. For quantum mechanical computations, one can usually define new commuting coordinates in terms of a combination of phase-space coordinates. In this scenario, non-commutativity can be thought of physically as an external magnetic field (see Refs. [32, 33] for further details). This procedure does not translate to the Lagrangian formalism of quantum field theory. Instead, non-commutative quantum field theories are formulated with

ordinary commuting coordinates, and the non-commutativity enters through a Moyal $*$-product multiplication law [30]. However it has been argued that the $*$-product prescription of non-commutative quantum field theory does not cure the UV-divergences that one would expect from a successful theory of non-commutative geometry and also leads to violations of Lorentz invariance and unitarity [30, 31].

An alternative approach to non-commutative quantum field theory was introduced in Ref. [30] based on a coherent state formalism. The coherent state approach introduces a natural cutoff in the propagator for a free particle as determined by the non-commutative parameter θ which leads to a theory that is UV finite [31]. The result is that point-like structures represented by Dirac-delta functions of positions are eliminated in favour of Gaussian smeared matter distributions of width $\sqrt{2\theta}$ [34]. Non-commutativity is intrinsic to the manifold, rather than some superimposed geometrical structure, so we would expect not to just extend classical concepts, but rather to obtain entirely new phenomenon [34]. Indeed this is the case as we will show in subsequent sections.

2.3 Non-commutative Black Holes

One method in which we might observe the effects of a non-commutative geometry are through the properties of black holes. We may anticipate that the fuzziness of spacetime introduced by non-commutativity of the spatial coordinates may lead to deviations from standard general relativity. Given that non-commutative geometry has been shown to cure the bad short-distance behaviour in quantum field theory [30], we might hope that non-commutativity would cure the divergence that appears in general relativity, particularly the curvature singularity at the centre of a black hole. To investigate this scenario, we would ideally like to construct a full non-commutative equivalent of general relativity. Despite numerous studies in the field, no such complete formulation exists at the present time. Nevertheless we can still study non-commutative effects on the properties of black holes through modifications to typical

black hole metrics. A nice review of the developments of non-commutative inspired black holes is given by [22]. The non-commutative inspired Schwarzschild black hole was first introduced by Nicolini [34], and extended to the case of higher dimensional black holes by Rizzo [12], and later to charged black holes by Ansoldi [35]. A charged rotating solution was developed by applying the Newman-Janis algorithm in Ref. [36]. The Hawking effect and other thermodynamical aspects have been studied in Ref. [37–39]. Quasi-normal modes were calculated for massless scalar fields in Refs. [40, 41]. Tunneling of massive scalar fields was considered in Ref. [42]. A Monte Carlo event generator for the LHC was implemented in Ref. [27]. The discovery potential at the LHC with the ATLAS experiment was studied in Ref. [43]. Greybody factors were calculated for massless spin 0 fields in Ref. [11].

Since a full theory of non-commutative (NC) general relativity has not as of yet been worked out, the best we can do is leave the standard form of the Einstein tensor unchanged, and only consider NC effects on the matter source [34]. As stated above, the effect of non-commutativity is that the point like sources typically represented by Dirac delta functions of position are replaced with Gaussian smeared matter distributions of width $\sqrt{2\theta}$ [34]. The mass density of a static spherically symmetric source can then be represented as

$$\rho(r) = \frac{M}{(4\pi\theta)^{(n+3)/2}} e^{-\frac{r^2}{4\theta}}. \tag{2.6}$$

In principle, one is not restricted to use a Gaussian, and could instead use another form of smeared matter distribution, see for example Ref. [44]. The goal is then to find the higher dimensional NC modified metric that is spherically symmetric and exhibits the Schwarzschild-like property that $-g_{tt} = g_{rr}^{-1}$. This was first derived in four dimensions by Nicolini [34] and extended to the higher dimensional case by Rizzo [12], by using Eq. (2.6) with the additional condition of covariant conservation of the energy momentum tensor which generates the following solution

$$ds^2 = -h(r)dt^2 + h(r)^{-1}dr^2 + r^2 d\Omega_{n+2}^2, \tag{2.7}$$

where $d\Omega_{n+2}^2$ is the metric of $(n+2)$-dimensional unit sphere

$$d\Omega_{n+2}^2 = d\theta_{n+1}^2 + \sin^2\theta_{n+1}\left(d\theta_n^2 + \sin^2\theta_n^2\left(\cdots + \sin^2\theta_2\left(d\theta_1^2 + \sin^2\theta_1 d\phi^2\right)\right)\right). \quad (2.8)$$

The metric function $h(r)$ is defined as

$$h_{NC} = 1 - \frac{1}{k_n}\frac{M}{M_D}\frac{1}{(M_D r)^{n+1}} P\left(\frac{n+3}{2}, \frac{r^2}{4\theta}\right), \quad (2.9)$$

where

$$k_n = \frac{n+2}{2^n \pi^{(n-3)/2}\Gamma\left(\frac{n+3}{2}\right)}, \quad (2.10)$$

and P is the normalized lower incomplete gamma function γ

$$P\left(\frac{n+3}{2}, \frac{r^2}{4\theta}\right) = \frac{1}{\Gamma\left(\frac{n+3}{2}\right)}\gamma\left(\frac{n+3}{2}, \frac{r^2}{4\theta}\right) = \frac{1}{\Gamma\left(\frac{n+3}{2}\right)}\int_0^{\frac{r^2}{4\theta}} dt e^{-t} t^{\frac{n+3}{2}-1}. \quad (2.11)$$

In the limit of $\theta \to 0$ or $P \to 1$, we recover the higher dimensional commutative metric, also known as the Schwarzschild-Tangherlini (ST) solution [45]. In Figure 2.1 we plot the metric function against the radial coordinate r for different black hole masses. For large r, or more specifically $r \gg \sqrt{\theta}$, the metric function has asymptotic behaviour which approaches the usual ST case. In the vicinity of $r = 0$, the metric function remains finite which as we will show later is a signature of the regularity of the manifold at short scales [11].

Depending on the mass of the black hole, there can be no horizon, a single degenerate horizon, or two horizons. A novel feature of NC black holes is the existence of a minimum mass below which a horizon will not form. The horizon radius $r_{\rm H}$ is defined by $g^{rr}(r_{\rm H}) = 0$, which for $\theta \neq 0$ leads to the transcendental equation

$$r_{\rm H} = \frac{1}{M_D}\left[\frac{M}{k_n M_D} P\left(\frac{n+3}{2}, \frac{r_{\rm H}^2}{4\theta}\right)\right]^{\frac{1}{n+1}}. \quad (2.12)$$

We are unaware of a closed from solution to this equation and so have solved it numerically for $r_{\rm H}$. In the commutative limit of $\theta = 0$, the horizon reduces to the usual higher dimensional ST case

$$r_{\rm H}|_{\theta=0} = \frac{1}{M_D}\left[\frac{M}{k_n M_D}\right]^{\frac{1}{n+1}}. \quad (2.13)$$

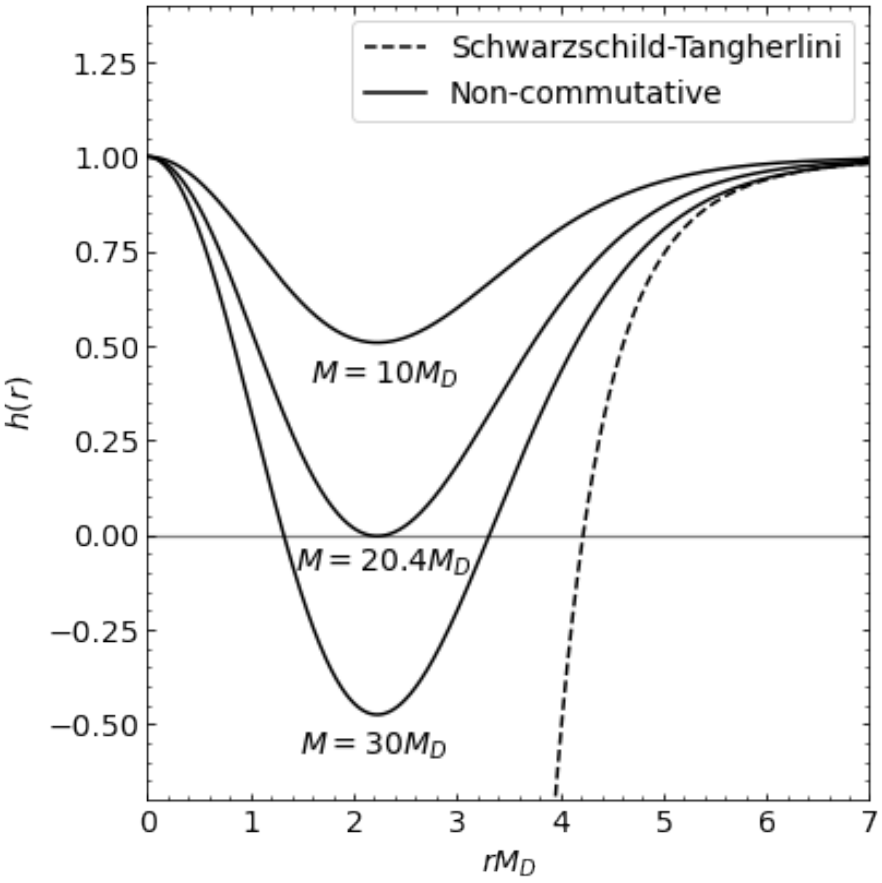

Figure 2.1: The metric function $h(r)$ for various black hole masses in $n = 7$ extra dimensions and $M_D = \sqrt{\theta} = 1$. The solid curves are for non-commutative cases depicting the possibility of $0, 1$, or 2 horizons with masses corresponding to $30M_D$, $20.4M_D$ and $10M_D$, respectively. The dashed curve represents the Schwarzschild-Tangherlini case with a mass of $30M_D$ for comparison.

The difference between the NC and ST horizon radius for a given mass is maximum at the NC minimum mass. This is clearly seen for $n = 7$ case in Figure 2.1. In Table 2.1 we give the NC minimum mass $M_{\rm min}$ and corresponding horizon radius $r_{\rm H}$ for each number of extra dimensions n with $M_D = \sqrt{\theta} = 1$.

Table 2.1: Non-commutative inspired black hole minimum mass $M_{\rm min}$ for which there exists a single degenerate horizon, as well as the horizon radius r_H for different number of extra dimensions n with $M_D = \sqrt{\theta} = 1$.

	n							
	0	1	2	3	4	5	6	7
$M_{\rm min}/M_D$	47.9	63.2	65.3	58.9	48.7	37.9	28.3	20.4
$r_{\rm H}M_D$	3.05	2.71	2.52	2.43	2.35	2.32	2.29	2.26

For masses greater than the minimum mass, we observe in addition to the outer event horizon, the existence of an inner Cauchy horizon. The existence of a Cauchy horizon potentially leads to instabilities similar to those found in the Reissner-Nordstrom or Kerr metrics, though further investigation into this instability is required before a definite conclusion can be made [46, 47].

The finite behaviour of the metric function in Eq. (2.9) as $r \to 0$ is a particularly interesting result arising from the NC geometry. To further investigate the regularity of the metric, it is of interest to compute the Kretschmann scalar which is defined as

$$K = R_{abcd}R^{abcd}, \tag{2.14}$$

where here we make use of the Einstein summation convention, and $R_{abcd} = g_{ae}R^{e}{}_{bcd}$ where $R^{e}{}_{bcd}$ is the Riemann curvature tensor. The Kretschmann scalar is useful for determining the regularity of the metric as well as distinguishing real singularities from coordinate singularities. For a static and spherically symmetric space-time defined in terms of a single metric function $h(r)$ as described by Eq. (2.7), the Kretschmann scalar simplifies to the following general form

$$K = (h'')^2 + 4\frac{(h')^2}{r^2} + 4\frac{(h-1)^2}{r^4}, \tag{2.15}$$

where a prime denotes a derivative with respect to r. For this we require the first derivative of the metric function with respect r

$$h'(r) = \frac{M}{k_n \Gamma\left(\frac{n+3}{2}\right) M_D^{n+2}} \left[(n+1) \frac{1}{r^{n+2}} \gamma\left(\frac{n+3}{2}, \frac{r^2}{4\theta}\right) - \frac{2r}{(4\theta)^{\frac{n+3}{2}}} e^{-\frac{r^2}{4\theta}} \right], \tag{2.16}$$

where we used the definition

$$\gamma'\left(\frac{n+3}{2}, \frac{r^2}{4\theta}\right) = 2 \frac{r^{n+2}}{(4\theta)^{\frac{n+3}{2}}} e^{-\frac{r^2}{4\theta}}. \tag{2.17}$$

We also require the second derivative of the metric function with respect to r

$$\begin{aligned} h''(r) &= \frac{M}{k_n \Gamma\left(\frac{n+3}{2}\right) M_D^{n+2}} \left[-(n+1)(n+2) \frac{1}{r^{n+3}} \gamma\left(\frac{n+3}{2}, \frac{r^2}{4\theta}\right) \right. \\ &\left. + \frac{4(n+1)}{(4\theta)^{\frac{n+3}{2}}} e^{-\frac{r^2}{4\theta}} - \frac{2}{(4\theta)^{\frac{n+3}{2}}} e^{-\frac{r^2}{4\theta}} \left((n+2) - \frac{r^2}{2\theta} \right) \right]. \end{aligned} \tag{2.18}$$

We find that in the NC case, the Kretschmann scalar remains finite over all r for $n \leq 7$ and for the case of $0, 1$ and 2 horizons thus verifying the regularity of the metric described by Eq. (2.9). As a representative example, we plot the Kretschmann scalar for the case of $n = 7$ with $M_D = \sqrt{\theta} = 1$ for each of the possible horizon scenarios in Figure 2.2. In contrast to the ST case which diverges as $r \to 0$, the NC case remains finite.

As shown in Figure 2.2, the Kretschmann scalar in the NC case approaches a finite value as $r \to 0$. It may be interesting to derive the analytic form the Kretschmann scalar in the limiting case of $r \to 0$. Using the series representation of the lower incomplete gamma function

$$\gamma(s, z) = z^s \Gamma(s) e^{-z} \sum_{k=0}^{\infty} \frac{z^k}{\Gamma(s+k+1)}, \tag{2.19}$$

which for $z \to 0$ behaves like

$$\gamma(s, z) \overset{z \to 0}{=} z^s \frac{\Gamma(s)}{\Gamma(s+1)} = \frac{z^s}{s}, \tag{2.20}$$

we find that the Kretschmann scalar for the NC metric takes on the following finite value for $r \to 0$

$$K|_{r \to 0} = \left(\frac{M}{k_n \Gamma\left(\frac{n+3}{2}\right) M_D^{n+2}} \right)^2 \frac{1}{(4\theta)^{n+3}} \frac{96}{(n+3)^2}. \tag{2.21}$$

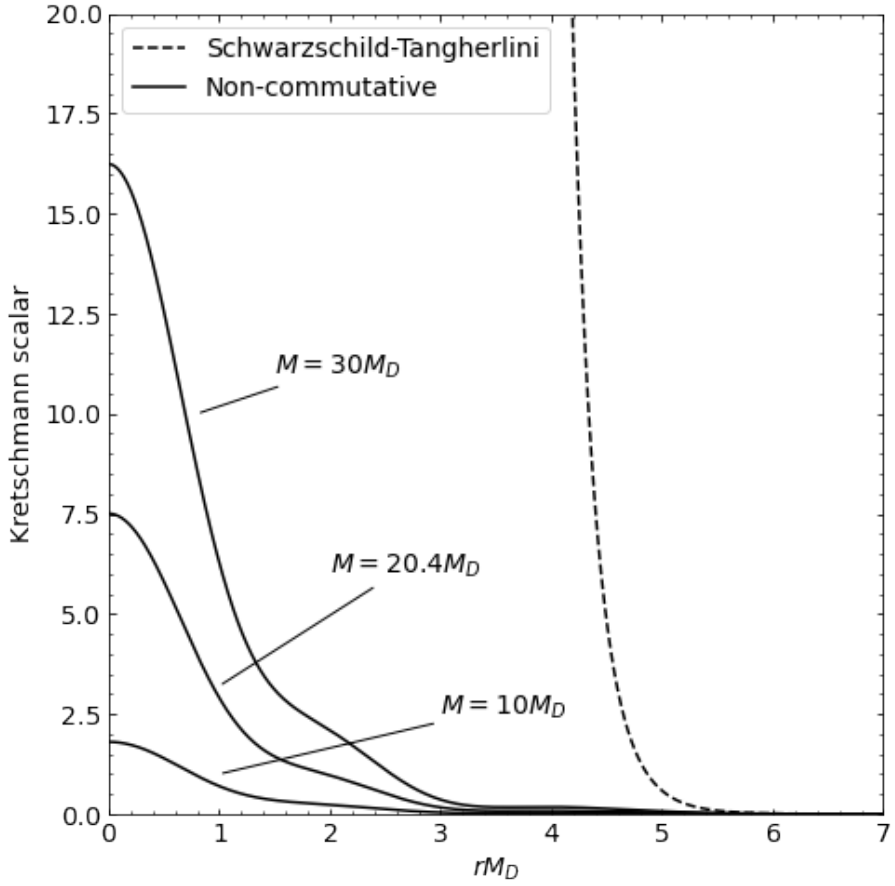

Figure 2.2: Kretschmann scalar versus the radial coordinate for $n = 7$ extra dimensions and with $M_D = \sqrt{\theta} = 1$. The solid lines depict the finite behaviour of the non-commutative metric as $r \to 0$ increasing from bottom to top with masses of $10M_D$, $20.4M_D$ and $30M_D$ corresponding to geometries with no horizon, one degenerate horizon and two horizons, respectively. The dashed line represents the Schwarzschild-Tangherlini metric for a mass of $30M_D$ which diverges as $r \to 0$.

For completeness, we also give the analytic form of the Kretschmann scalar for the ST case

$$K = \left(\frac{M}{k_n \Gamma\left(\frac{n+3}{2}\right) M_D^{n+2}} \right)^2 \frac{1}{r^{2n+6}} \left[(n+1)^2(n+2)^2 + 4(n+1)^2 + 4 \right]. \tag{2.22}$$

Perhaps the most striking feature of NC black holes are their thermodynamic properties. The Hawking temperature for a higher dimensional NC black hole is given by [34]

$$T_{\rm H} = \left(\frac{1}{4\pi} \frac{dg_{00}}{dr} \right)\Big|_{r=r_{\rm H}} = \frac{n+1}{4\pi r_{\rm H}} \left[1 - \frac{2}{n+1} \left(\frac{r_{\rm H}^2}{4\theta} \right)^{\frac{n+3}{2}} \frac{e^{\frac{-r_{\rm H}^2}{4\theta}}}{\gamma\left(\frac{n+3}{2}, \frac{r_{\rm H}^2}{4\theta}\right)} \right]. \tag{2.23}$$

We note that the temperature is dependent on the mass through the horizon radius as described in Eq. (2.12). The quantity in square brackets modifies the usual higher dimensional commutative form of the temperature. In Figure 2.3 we plot the temperature against the horizon radius with $M_D = \sqrt{\theta} = 1$. We observe that in contrast to the ST case, there exists a maximum temperature, and also that the temperature vanishes at the minimum mass.

In later sections when computing the greybody factors and comparing the emission to the ST case, of interest to us will be the NC black hole maximum temperature $T_{\rm max}$ and mass M_{eM} at which the maximum temperature occurs. To separate the effect of temperature on the emission spectra from the non-commutative effects, we will also use values of the ST black hole mass at equal temperature to the NC black hole maximum temperature M_{eT}. These values are shown in Table 2.2.

To give us a better understanding of the unique thermodynamical characteristics of NC black holes, we study the heat capacity (at constant pressure) C, which is defined as [12]

$$C = \frac{\partial M}{\partial T_{\rm H}} = \frac{\partial M}{\partial r_{\rm H}} \left(\frac{\partial T_{\rm H}}{\partial r_{\rm H}} \right)^{-1}. \tag{2.24}$$

For NC black holes, the heat capacity takes on the following form

$$C = -\frac{4\pi k_n \left(M_D r_{\rm H}\right)^{n+2} \left(1 - \frac{2}{n+1} u_n(r_{\rm H})\right)}{P\left(\frac{n+3}{2}, \frac{r_{\rm H}^2}{4\theta}\right) \left[1 + \frac{2}{n+1} u_n(r_{\rm H}) \left(n + 2 - \frac{2r_{\rm H}^2}{4\theta} - 2u_n(r_{\rm H})\right)\right]}, \tag{2.25}$$

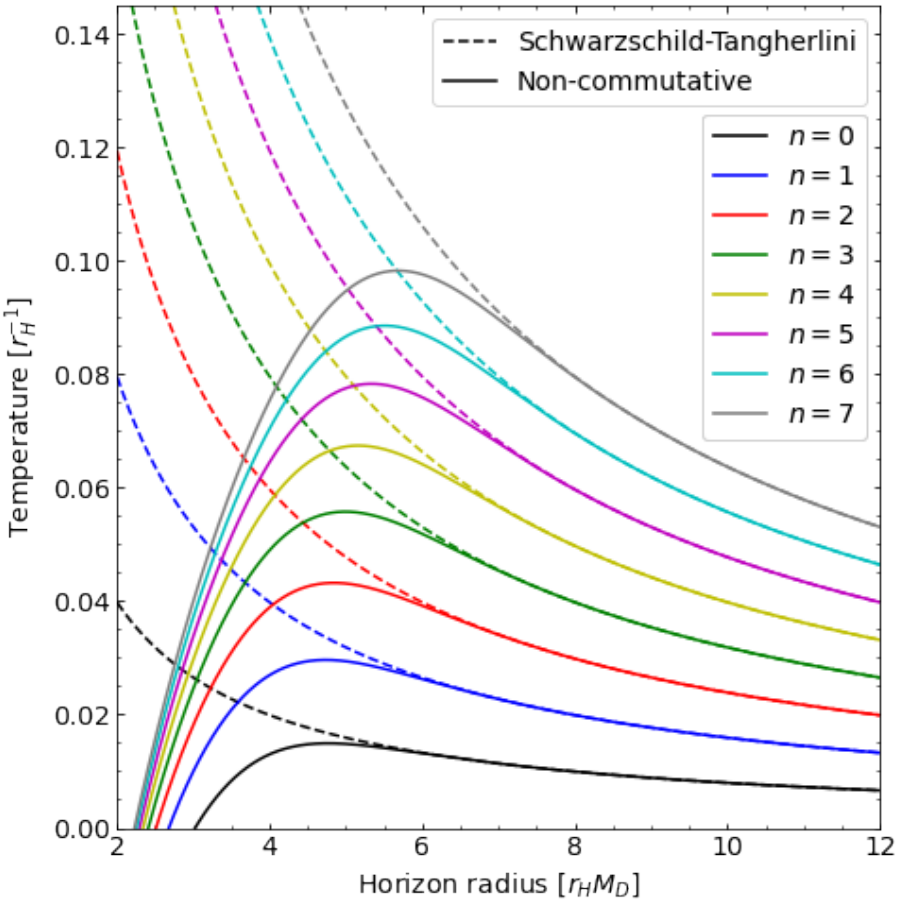

Figure 2.3: Black hole temperature versus the horizon radius for a different number of extra dimensions with $M_D = \sqrt{\theta} = 1$. The solid lines are for non-commutative black holes and the dashed lines are for Schwarzschild-Tangherlini black holes.

Table 2.2: Non-commutative inspired black hole maximum temperature $T_{\max}$, mass at which the maximum temperature occurs M_{eM}, and mass M_{eT} of a Schwarzschild-Tangherlini black hole that has temperature equal to the NC black hole maximum temperature $T_{\max}$, for different number of extra dimensions n with $M_D = \sqrt{\theta} = 1$.

	n							
	0	1	2	3	4	5	6	7
$T_{\max}[r_{\rm H}^{-1}]$	0.015	0.030	0.043	0.056	0.067	0.078	0.089	0.098
M_{eM}/M_D	60.47	108.3	157.5	204.9	249.1	289.4	325.6	357.7
M_{eT}/M_D	66.95	136.0	224.8	332.0	456.4	597.0	753.0	923.7

where for convenience we have defined

$$u_n(r_{\rm H}) = \left(\frac{r_{\rm H}^2}{4\theta}\right)^{\frac{n+3}{2}} e^{-\frac{r_{\rm H}^2}{4\theta}} \left[\gamma\left(\frac{n+3}{2}, \frac{r_{\rm H}^2}{4\theta}\right)\right]^{-1}. \tag{2.26}$$

When $\theta \to 0$, we recover the commutative form of $C_{ST} = -4\pi k_n \left(M_D r_{\rm H}\right)^{n+2}$. In Figure 2.4 we plot the heat capacity versus the horizon radius with $M_D = \sqrt{\theta} = 1$. For large $r_{\rm H}$ we find that C is negative and asymptotes to the commutative value. At $r_{\rm H}$ corresponding to the maximum temperature, there is a phase transition and C changes sign. This means that for NC black holes with a horizon radius less than the maximum temperature horizon radius, we find that $C > 0$ and the system is thermodynamically stable. The heat capacity vanishes as the temperature goes to zero corresponding to the minimum mass.

For a NC black hole evaporating via Hawking radiation, as the mass approaches the minimum mass, the temperature approaches zero and the heat capacity vanishes which may terminate Hawking radiation leaving behind a remnant mass [34]. These properties are in clear contradistinction to the classical black hole with temperature becoming infinite as the black hole approaches zero mass and horizon radius. The emergence of a remnant mass has appeared in other quantum gravity motivated theories such as in loop quantum gravity [48], and the thermodynamical stability near the end of the black hole evaporation has been argued to be a general property of quantum gravity inspired black holes [11, 49]. A unique feature of NC black holes is that the minimum mass remains above the Planck scale [22].

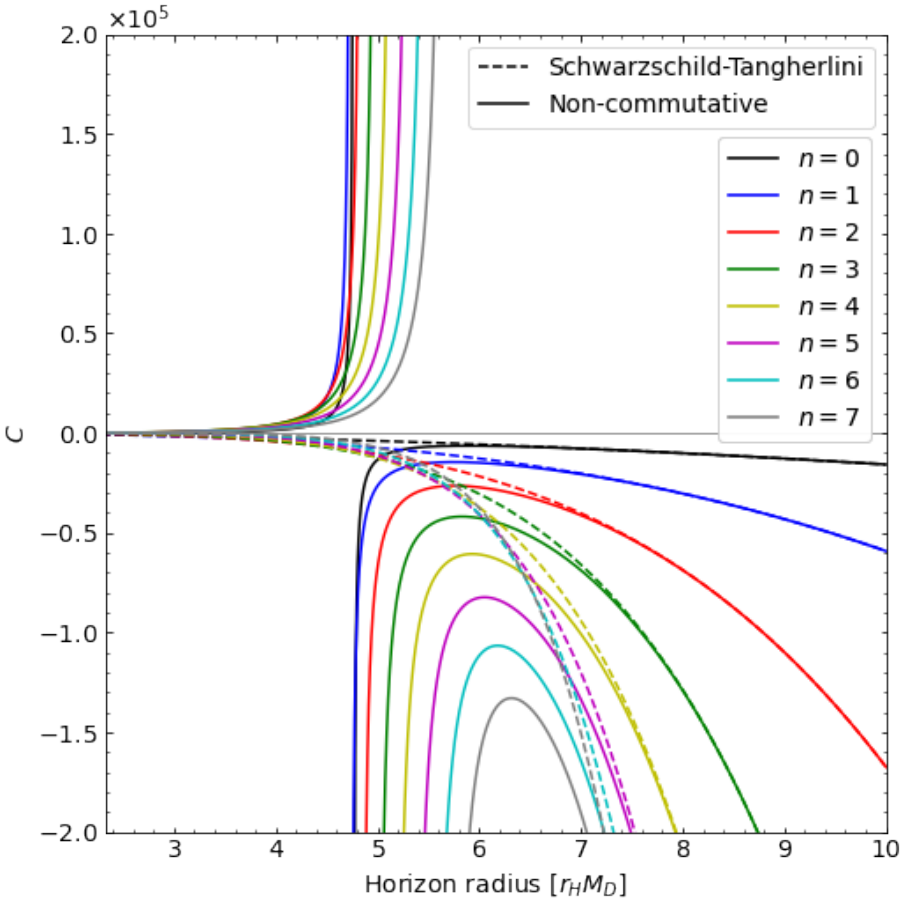

Figure 2.4: Black hole heat capacity at constant pressure versus the horizon radius for a different number of extra dimensions with $M_D = \sqrt{\theta} = 1$. The solid lines are for non-commutative black holes and the dashed lines are for Schwarzschild-Tangherlini black holes.

To conclude our analysis of the thermodynamic properties of NC black holes, we may also consider the entropy which is defined as [12]

$$S = \int \frac{1}{T_{\rm H}} \frac{\partial M}{\partial r_{\rm H}} dr_{\rm H}. \tag{2.27}$$

For NC black holes it is natural to define the lower limit of integration such that the entropy vanishes at the horizon radius corresponding to the minimum mass. In Figure 2.5 we plot the black hole entropy versus the horizon radius $M_D = \sqrt{\theta} = 1$. For large horizon radii we recover the commutative limit of $S = 4\pi k_n M_D^{n+2} r_{\rm H}^{n+2}/(n+2)$.

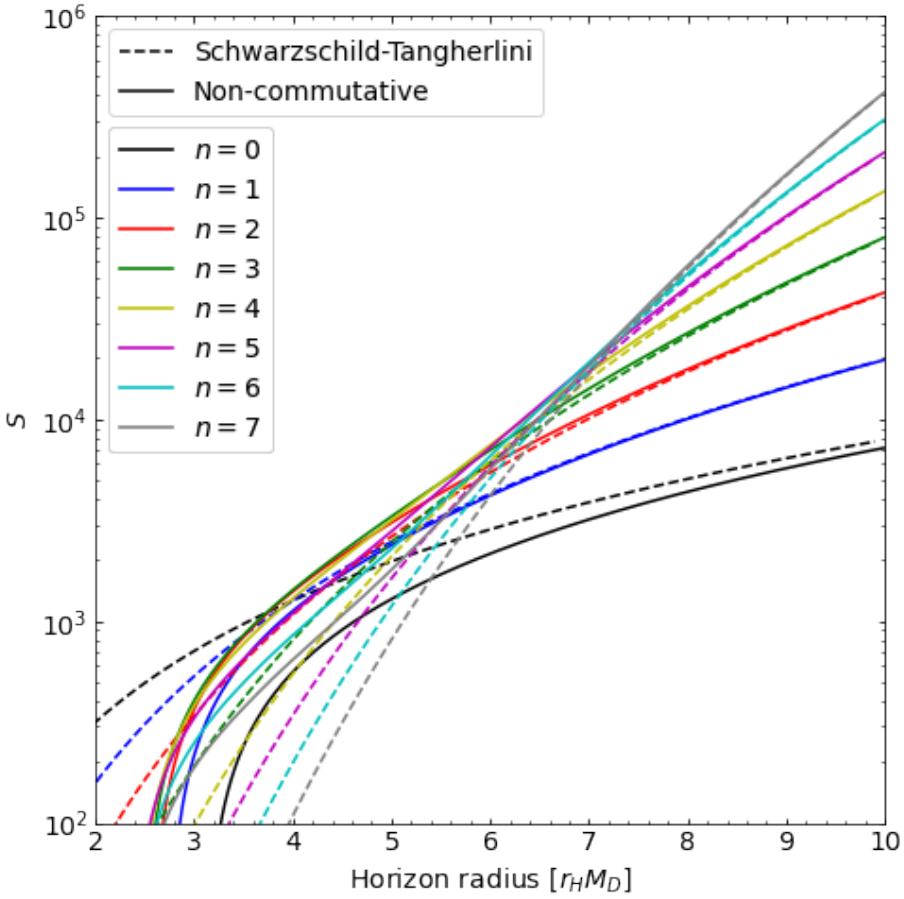

Figure 2.5: Black hole entropy versus the horizon radius for a different number of extra dimensions with $M_D = \sqrt{\theta} = 1$. The solid lines are for non-commutative black holes and the dashed lines are for Schwarzschild-Tangherlini black holes. The number of dimensions increases from bottom to top at large horizon radii.

Chapter 3

Theoretical Overview

In order to compute the Hawking radiation emitted from black holes, one needs to compute the relevant greybody factors. Black hole greybody factors are typically studied in the context of a perturbation problem by examining the response to perturbations of various spin fields. For a treatment of the problem in the context of tunneling through a potential barrier, we refer the reader to [18]. Physically, the greybody factors represent the transmission coefficients between the ingoing and outgoing waves at the horizon as viewed by an observer at spatial infinity. Gravitational perturbations of a black hole were first studied by Regge and Wheeler for the axial or odd parity modes of a Schwarzschild black hole [50]. The polar or even parity modes were later derived by Zerilli [51]. Bardeen and Press used the Newman-Penrose formalism to derive the perturbations of Schwarzschild black hole which can be transformed to either the axial or polar equations [52]. Teukolsky and Press applied similar concepts to the Kerr geometry to derive a master equation for spin $0, 1/2, 1$ and 2 perturbations of a rotating black hole [53–55]. Teukolsky's formalism has since been applied to a number of different black hole metrics, such as the Myers-Perry metric for higher dimensional rotating black holes with a single angular momentum parameter by Kanti [56].

In this section, we will introduce the relevant mathematical tools necessary to compute greybody factors for massless spin fields from spherically symmetric metrics on

the brane and in the bulk. Throughout, we will keep our derivation as general as possible to allow for the possible extension to other spherically symmetric metrics. We will separate the Teukolsky equation into angular and radial parts. We solve for the eigenvalues of the angular equation and insert them into the radial equation. The radial equation turns out be a second order differential equation which we cast into the form of a one-dimensional Schrödinger equation with the appropriate Chandrasekhar transformation. Finally we introduce the transfer matrix formalism with which we numerically compute the greybody factors. Since a metric describing a rotating black hole in a NC geometry does not yet exist, we will restrict our attention to NC black holes only in the non-rotating case. For an outline of the procedure for higher dimensional rotating black holes, see Appendix A.

3.1 Black Hole Perturbation Theory

The computation of both greybody factors and quasi-normal modes is rooted within the framework of black hole perturbation theory. Black hole perturbation theory governs the propagation of fields in the background space-time of the black hole background. Generally one considers external perturbations by adding a test field to the black hole background space-time and determining the resulting equation of motion [57]. For gravitational perturbations, one could also perturb the metric itself and proceed with linearizing the Einstein equations. In four dimensions there are two types of gravitational perturbations, scalar perturbations (also known as polar or even) and vector perturbations (also known as axial or odd). Scalar perturbations are invariant under a reversal of the azimuthal direction whereas vector perturbations are not [58]. In the case of Schwarzschild black holes, the scalar and vector perturbations give rise to the same greybody factors and quasi-normal modes, a property known as isospectrality. This was first discovered by Chandrasekhar and Detweiler who related the two types of perturbations through a transformation [59]. Isospectrality is not guaranteed for all metrics, and analytical proof is difficult to obtain [60]. In higher

dimensions, a third kind of gravitational perturbation arises which is called a tensor perturbation [61].

3.1.1 Spherically Symmetric Metrics

Let us begin by considering a general spherically symmetric and static metric in a $(4+n)$-dimensional space-time

$$ds^2 = -G(r)dt^2 + \frac{1}{F(r)}dr^2 + H(r)d\Omega_{n+2}^2. \tag{3.1}$$

Further, we are interested in asymptotically flat space-times such that at spatial infinity $r \to \infty$ we have

$$G(r) \to 1, \quad F(r) \to 1, \quad \text{and} \quad H(r) \to r^2. \tag{3.2}$$

For the non-commutative and Schwarzschild-Tangherlini black holes for which we are interested in, the metrics exhibit time-radial symmetry such that $F(r) = G(r) = h(r)$ and $H(r) = r^2$. Ordinary matter is restricted to propagate on the brane, while scalars and gravitons may propagate in the full higher dimensional bulk. The 4-dimensional brane can be represented as a slice of the higher dimensional space-time [11]. The metric for brane-localized modes can be obtained by fixing the values of the extra angular coordinates, θ_i for $i > 1$

$$ds^2 = -G(r)dt^2 + \frac{1}{F(r)}dr^2 + H(r)d\Omega^2, \tag{3.3}$$

where now $d\Omega^2 = (d\theta^2 + \sin\theta d\phi^2)$ is the metric of the 2-dimensional unit sphere.

For scalar fields, it is straightforward to write the Klein-Gordon equation in curved space-time [62, 63]. The Klein-Gordon equation for a massive scalar field Φ is

$$\left(\Box - m_\Phi^2\right)\Phi = \frac{1}{\sqrt{-g}}\partial_\mu\left(g^{\mu\nu}\sqrt{-g}\partial_\nu\Phi\right) - m_\Phi^2 = 0, \quad \text{and} \quad \sqrt{-g} = \sqrt{\frac{G}{F}}H\sin\theta, \tag{3.4}$$

where m_Φ is the mass of the field. Evaluating each of the components gives

$$\begin{aligned}
\frac{1}{\sqrt{-g}}\partial_t\left(g^{tt}\sqrt{-g}\partial_t\Phi\right) &= -\frac{1}{G}\frac{\partial^2\Phi}{\partial t^2}, && (3.5)\\
\frac{1}{\sqrt{-g}}\partial_r\left(g^{rr}\sqrt{-g}\partial_r\Phi\right) &= \frac{1}{H}\sqrt{\frac{F}{G}}\frac{\partial}{\partial r}\left(H\sqrt{FG}\frac{\partial\Phi}{\partial r}\right), && (3.6)\\
\frac{1}{\sqrt{-g}}\partial_\theta\left(g^{\theta\theta}\sqrt{-g}\partial_\theta\Phi\right) &= \frac{1}{H\sin\theta}\frac{\partial}{\partial\theta}\left(\sin\theta\frac{\partial\Phi}{\partial\theta}\right), && (3.7)\\
\frac{1}{\sqrt{-g}}\partial_\phi\left(g^{\phi\phi}\sqrt{-g}\partial_\phi\Phi\right) &= \frac{1}{H\sin^2\theta}\frac{\partial^2\Phi}{\partial\phi^2}. && (3.8)
\end{aligned}$$

The equations of motion become

$$\begin{aligned}
-\frac{\partial^2\Phi}{\partial t^2} &+ \frac{G}{H}\left(\frac{1}{\sin\theta}\frac{\partial}{\partial\theta}\left(\sin\theta\frac{\partial\Phi}{\partial\theta}\right)+\frac{1}{\sin^2\theta}\frac{\partial^2\Phi}{\partial\phi^2}\right)+\frac{FG}{H}\frac{\partial}{\partial r}\left(H\sqrt{FG}\frac{\partial\Phi}{\partial r}\right)\\
&- Gm_\Phi^2\Phi = 0. \qquad (3.9)
\end{aligned}$$

For higher spin fields it is difficult to work directly with the metric due to the multiplicity of the components [63]. Instead, the Newman-Penrose formalism is often used, which relies on a reformulation of the equations of motion using a null tetrad field [64]. This approach was popularized by Teukolsky as applied to the study of perturbations of the Kerr metric [53]. The Newman-Penrose formalism has been well studied in the literature, and we only present the resulting equations of motion here. For a spherically symmetric and static metric, the equations of motion for a massless field ψ_s with spin s reads [63]

$$\begin{aligned}
&-\frac{\partial^2\psi_s}{\partial t^2}+s\frac{\sqrt{FG}}{H}\left(H\frac{G'}{G}-H'\right)\partial_t\psi_s+GF\partial_r^2\psi_s\\
&+\left(\frac{GF'}{2}+(2s+1)\frac{FG'}{2}+(s+1)\frac{GFH'}{H}\right)\partial_r\psi_s\\
&+\frac{G}{H}\left(\frac{1}{\sin\theta}\partial_\theta\left(\sin\theta\partial_\theta\right)+\frac{2is\cos\theta}{\sin^2\theta}\partial_\phi+\frac{1}{\sin^2\theta}\partial_\phi^2-s-s^2\cot^2\theta\right)\psi_s\\
&+\left(sFG''+\frac{3s-2s^2}{2}\frac{GFH''}{H}-\frac{sFG'^2}{2G}+\frac{2s^2-s}{4}GFH'^2+\frac{sF'G'}{2}\right.\\
&\left.+\frac{3s-2s^2}{4}\frac{GF'H'}{H}+\frac{2s^2+5s}{4}\frac{FG'H'}{H}\right)\psi_s=0, \qquad (3.10)
\end{aligned}$$

where a prime denotes a derivative with respect to the radial coordinate r. The

equations are separable into radial and angular parts by writing the ansatz

$$\psi_s = e^{-i\omega t} e^{im\phi}\, {}_sY_\ell^m(\theta) R_s(r), \tag{3.11}$$

where ${}_sY_\ell^m(\theta)$ are the spin-weighted spherical harmonics with eigenvalues ${}_s\lambda_\ell = \ell(\ell+1) - s(s+1)$. The resulting radial equation reads

$$\begin{aligned}
&\sqrt{\frac{F}{G}}\frac{1}{(GH)^s}\frac{d}{dr}\left(\sqrt{FG}(GH)^s H\frac{dR_s}{dr}\right) + \left(\frac{H}{G}\omega^2 + is\omega\sqrt{\frac{F}{G}}\left(H' - H\frac{G'}{G}\right)\right.\\
&+ s\frac{FG''H}{G} + s\frac{3-2s}{2}FH'' - s\frac{FG'^2H}{2G^2} + s\frac{2s-1}{4H}FH'^2 + s\frac{F'G'H}{2G}\\
&\left.+ s\frac{3-2s}{4}F'H' + s\frac{2s+5}{4G}FG'H' - 2s - {}_s\lambda_\ell\right)R_s = 0.
\end{aligned} \tag{3.12}$$

3.2 Short-ranged Potentials

The radial equation contains information about the transmission and reflection coefficients, and hence the greybody factors. The radial equation is a second order ODE for which there is no known analytic solution.

The trouble with the radial equation in the context of a scattering problem is that the first order radial derivatives create complex $is\,\omega$ terms which have a $1/r$ behaviour at infinity [65]. This eventually leads to problems in the numerical computations and introduces round-off errors and instability. In four dimensions, Chandrasekhar [66] found that the radial Teukolsky equation can be transformed into a one dimensional Schrödinger-like wave equation with an effective short-ranged potential

$$\left[\frac{d^2}{dr_*^2} + \omega^2\right] Z(r_*) - V(r(r_*))Z(r_*) = 0, \tag{3.13}$$

where r_* is a generalized tortoise coordinate. Similar transformations can be made for different types of metrics. The purpose of this transformation is that the potentials $V(r(r_*))$ are short-ranged, that is they die away faster than $1/r$ proving advantageous for numerical computations [65].

3.2.1 Short-ranged Potentials on the Brane

Short-ranged potentials for a general static and spherically symmetric metric on the brane were derived for massless spin 1 and 1/2 fields in Ref. [63] and for massless vector spin 2 fields in Ref. [67]. The scalar spin 2 potential was derived in Ref. [60]. The short-range potentials for a general spherically symmetric and static metric on the brane are

$$V_0 = {}_0\lambda_\ell \frac{G}{H} + \frac{1}{\sqrt{H}}\partial_*^2\sqrt{H}, \tag{3.14a}$$

$$V_{1/2} = ({}_{1/2}\lambda_\ell + 1)\frac{G}{H} \pm \sqrt{{}_{1/2}\lambda_\ell + 1}\,\partial_* \left(\sqrt{\frac{G}{H}}\right), \tag{3.14b}$$

$$V_1 = ({}_1\lambda_\ell + 2)\frac{G}{H}, \tag{3.14c}$$

$$V_2^V = ({}_2\lambda_\ell + 4)\frac{G}{H} + \frac{(\partial_* H)^2}{2H^2} - \frac{1}{\sqrt{H}}\partial_*^2\sqrt{H}, \tag{3.14d}$$

$$V_2^S = \frac{G({}_2\lambda_\ell + 4)^2}{({}_2\lambda_\ell + 4 + HU)^2}\left(\frac{{}_2\lambda_\ell + 6}{H} + U + \frac{HU^2}{({}_2\lambda_\ell + 4)^2}\left({}_2\lambda_\ell + 4 + \frac{HU}{3}\right)\right), \tag{3.14e}$$

where for the scalar spin 2 potential we have defined

$$U = \frac{2}{H} + \frac{1}{4H^2}\left((FG)' H' - 3F(H')^2 + 2FHH''\right). \tag{3.15}$$

The potentials are defined as functions of r, and the derivatives are with respect to r_*. Here, the tortoise coordinate is defined as

$$\frac{dr_*}{dr} = \frac{1}{\sqrt{FG}}, \tag{3.16}$$

such that $r_* \longrightarrow +\infty$ as $r \longrightarrow +\infty$ and $r_* \longrightarrow -\infty$ as $r \longrightarrow r_{\rm H}$. In some cases such as for the Schwarzschild-Tangherlini case, analytic expressions exist for $r_*(r)$. However in general and for the NC case, Eq. (3.16) must be numerically integrated. To solve for $r_*(r)$ numerically for NC black holes, we integrate Eq. (3.16) over the range $r/r_H = [\epsilon, 350]$. We take as an initial condition $r_*(r) = r_{*,ST}(r)$ for a large value of $r/r_H = 350$ approximating $+\infty$. Here we define $r_{*,ST}(r)$ as the tortoise coordinate for the ST case for which analytical solutions exist for any number of extra dimensions

and are given in Appendix B. In this way, the constant of integration is effectively chosen to be zero so that we asymptotically approach the ST case for $r \to \infty$. We then integrate backwards towards the horizon using a variable step size to a value of $r_H + \epsilon$ with $\epsilon \approx 10^{-16}$. This allows us to obtain $r_*(r)$ as close to $r_* \to -\infty$ as our machine precision will allow.

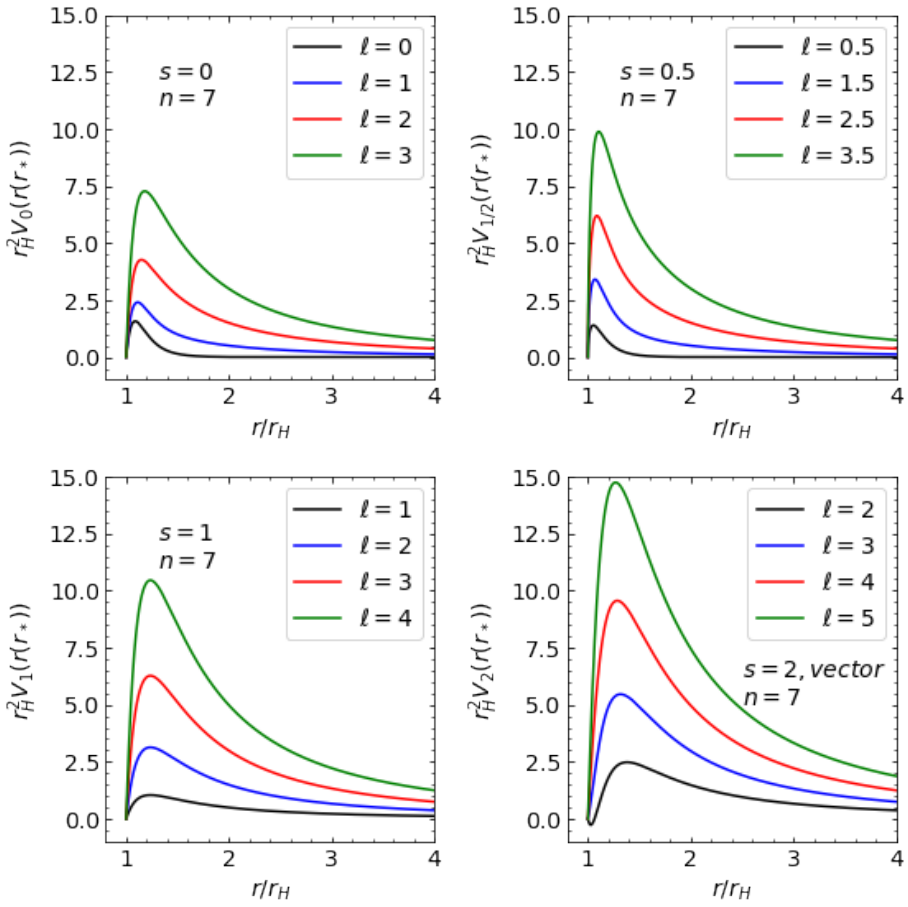

Figure 3.1: Effective potentials for non-commutative black holes versus the radial coordinate r for spin $0, 1/2, 1$ and 2 massless fields and $n = 7$. A black hole mass of $M = 358 M_D$ has been used corresponding to the non-commutative maximum temperature. $M_D = \sqrt{\theta} = 1$ has been taken.

In Figures 3.1 and 3.2 we show the behaviour of the potentials against r and r_*, respectively, for a NC black hole at the maximum temperature with $n = 7$ and $M_D = \sqrt{\theta} = 1$. For the spin 1/2 potential, one must take the positive sign in Eq. (3.14b) to get a positive potential for all r, although both potentials lead to

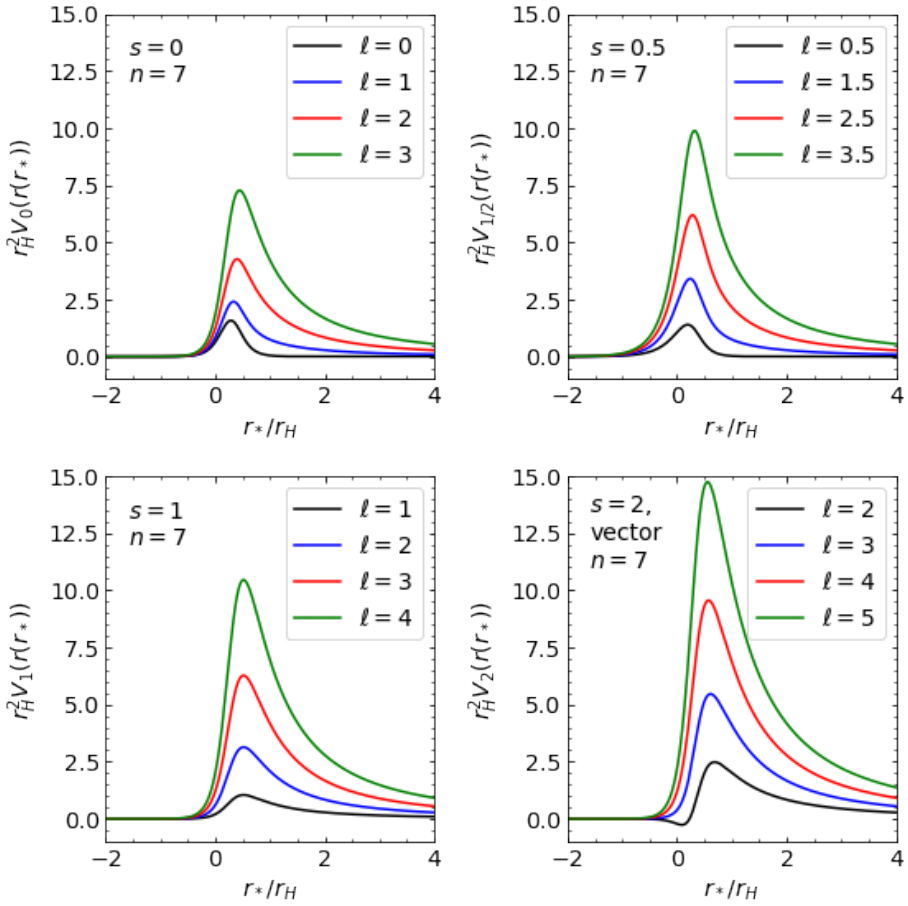

Figure 3.2: Effective potentials for non-commutative black holes versus the tortoise coordinate r_* for spin $0, 1/2, 1$ and 2 massless fields and $n = 7$. A black hole mass of $M = 358M_D$ has been used corresponding to the non-commutative maximum temperature $M = 358M_D$. $M_D = \sqrt{\theta} = 1$ has been taken.

the same transmission coefficients. For the spin-2 case, it is possible for the vector potential to become negative. This was first discussed in Ref. [67] for the ST case. For the ST case, for the potential to become negative we find that

$$n+3 > \ell(\ell+1). \tag{3.17}$$

Since we consider values of $n \leq 7$, we find that the potential only becomes negative when $\ell = 2$ and for $n > 3$. This condition is different than the one given in Ref. [67] as we use a different form of the potential. For the NC case, the condition for the potential to go negative is

$$n+3-2\frac{M}{k_n\Gamma\left(\frac{n+3}{2}\right)(M_D)^{n+2}}\frac{r_H^2}{(4\theta)^{\frac{n+3}{2}}}e^{\frac{-r_H^2}{4\theta}} > \ell(\ell+1). \tag{3.18}$$

We only get a negative potential when $\ell = 2$ and $M > 181.9M_D$ for $n = 4$, $M > 120.4M_D$ for $n = 5$, $M > 83.1M_D$ for $n = 6$, $M > 57.3M_D$ for $n = 7$. We will discuss the effect of the negative potential in further detail in later sections when describing the absorption cross section results. In Figure 3.3 we compare the behaviour of the vector and scalar spin 2 potentials against r_* for a NC black hole at the maximum temperature with $n = 7$ and $M_D = \sqrt{\theta} = 1$. We note that while the vector potential may go negative, the scalar potential is always positive.

3.2.2 Short-ranged Potentials in the Bulk

Emission of massless spin 0 and 2 fields in the bulk can be studied by finding the equation of motion on the full higher dimensional space-time given by Eq. (3.1). In the bulk we only present results for static and spherically symmetric metrics which exhibit time-radial symmetry with $F(r) = G(r) = h(r)$ and $H(r) = r^2$. In this case, spin 2 perturbations in the bulk decompose into three types: scalar, vector and tensor. In the bulk, it was found that the master equation for each type of perturbation is separable with [61]

$$\psi_s^{\text{bulk}} = e^{-i\omega t}R_s^{\text{bulk}}(r)\,{}_sY_{\ell,j}\left(\theta_1,...,\theta_{n+1},\phi\right), \tag{3.19}$$

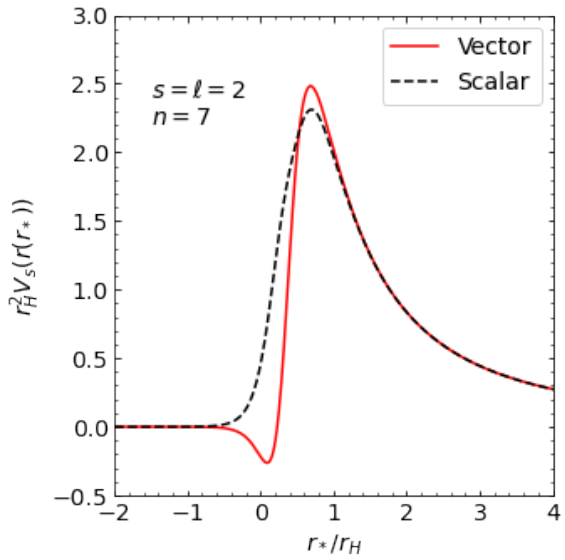

Figure 3.3: Scalar and vector spin 2 effective potentials for non-commutative black holes versus the tortoise coordinate r_* and for $n = 7$. A black hole mass of $M = 358M_D$ has been used corresponding to the non-commutative maximum temperature $M = 358M_D$. $M_D = \sqrt{\theta} = 1$ has been taken.

where $R_s^{\rm bulk}(r)$ is the bulk radial function and ${}_sY_{\ell,j}\left(\theta_1, ..., \theta_{n+1}, \phi\right)$ are the spin-weighted hyper-spherical harmonics which are a generalization of the spin-weighted spherical harmonics for higher dimensions of space [11, 68]. For each ℓ, there are N_ℓ hyper-spherical harmonics represented by the index j. The multiplicities for scalar N_ℓ^S, vector N_ℓ^V and tensor N_ℓ^T are

$$\begin{aligned} N_\ell^S &= \frac{(2\ell+n+1)(\ell+n)!}{\ell!(n+1)!}, \\ N_\ell^V &= \frac{\ell(\ell+n+1)(2\ell+n+1)(\ell+n-1)!}{n!(\ell+1)!}, \\ N_\ell^T &= \frac{n(n+3)(\ell+n+2)(\ell-1)(2\ell+n+1)(\ell+n-1)!}{2(\ell+1)!(n+1)!}. \end{aligned} \tag{3.20}$$

The scalar multiplicity N_ℓ^S reduces to the well known $2\ell+1$ for $n = 0$. Using the tortoise coordinate defined in Eq. (3.16), the bulk radial equation for massless spin 0 fields takes the form of that in Eq. (3.13) with the following short-ranged potential [69]

$$V_0^{\rm bulk} = h\left(\frac{\ell(\ell+n+1)}{r^2} + \frac{(n+2)}{2r}h' + \frac{n(n+2)}{4r^2}h\right). \tag{3.21}$$

The bulk spin 0 potential Eq. 3.21 reduces to the spin 0 potential on the brane for

$n = 0$. For massless spin 2 fields, short-ranged potentials for the scalar $V_2^{\text{bulk},S}$, vector $V_2^{\text{bulk},V}$ and tensor $V_2^{\text{bulk},T}$ modes are [61]

$$V_2^{\text{bulk},S} = h\frac{U}{16r^2\left[\ell(\ell+n+1)-(n+2)+\frac{1}{2}(n+2)(n+3)(1-h)\right]^2}, \tag{3.22a}$$

$$V_2^{\text{bulk},V} = h\left(\frac{\ell(\ell+n+1)-1-(n+1)}{r^2}-\frac{(n+2)}{2r}h'+\frac{(n+2)(n+4)}{4r^2}h\right), \tag{3.22b}$$

$$V_2^{\text{bulk},T} = h\left(\frac{\ell(\ell+n+1)}{r^2}+\frac{(n+2)}{2r}h'+\frac{n(n+2)}{4r^2}h\right), \tag{3.22c}$$

where for the scalar spin 2 potential we define

$$\begin{aligned} U =&(n+2)^4(n+3)^2(1-h)^3+(n+2)(n+3)\big[4(2(n+2)^2 \\ &-3(n+2)+4)\nu+n(n+2)(n-2)(n+3)\big](1-h)^2 \\ &-12(n+2)\left[(n-2)\nu+n(n+2)(n+3)\right]\nu(1-h)+16\nu^3 \\ &+4(n+2)(n+4)\nu^2, \end{aligned} \tag{3.23}$$

with $\nu = \ell(\ell+n+1)-(n+2)$. We note that the scalar potential given by Eq. (3.22a) is only applicable for the ST case and is not valid for a general metric function $h(r)$. Thus we cannot use Eq. (3.22a) to compute the emission of spin 2 scalar modes from NC black holes, nor are we aware of the general form of the potential. In four dimensions and for the ST case only, the scalar spin 2 potential reduces to the scalar spin 2 potential on the brane given in Eq. (3.14e). In four dimensions, the vector spin 2 potential reduces to the vector spin 2 potential on the brane given in Eq. (3.14d). There is no equivalent in four dimensions for the tensor spin 2 potential given in Eq. (3.22c). We note that the tensor spin 2 potential Eq. (3.22c) is identical to bulk spin 0 potential Eq. (3.14a). In Figures 3.4 and 3.5 we plot the spin 0 and vector and tensor spin 2 potentials for $n = 7$ and for various ℓ modes from a NC black hole. Black hole masses at the NC black hole maximum temperature are used.

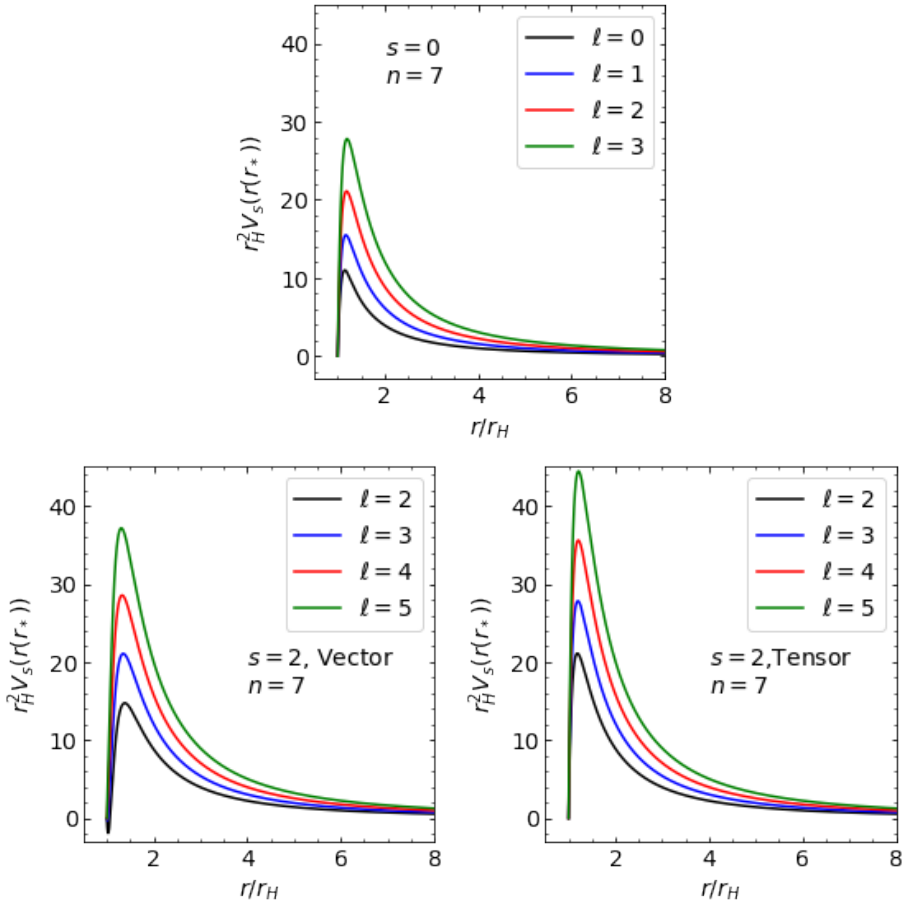

Figure 3.4: Effective potentials for non-commutative black holes in the bulk versus the radial coordinate for massless spin 0 and 2 fields versus the radial coordinate r and for $n = 7$. A black hole mass of $M = 358M_D$ has been used corresponding to the non-commutative maximum temperature. The peak of the potentials increases with increasing values of ℓ beginning at $\ell = s$. $M_D = \sqrt{\theta} = 1$ has been taken.

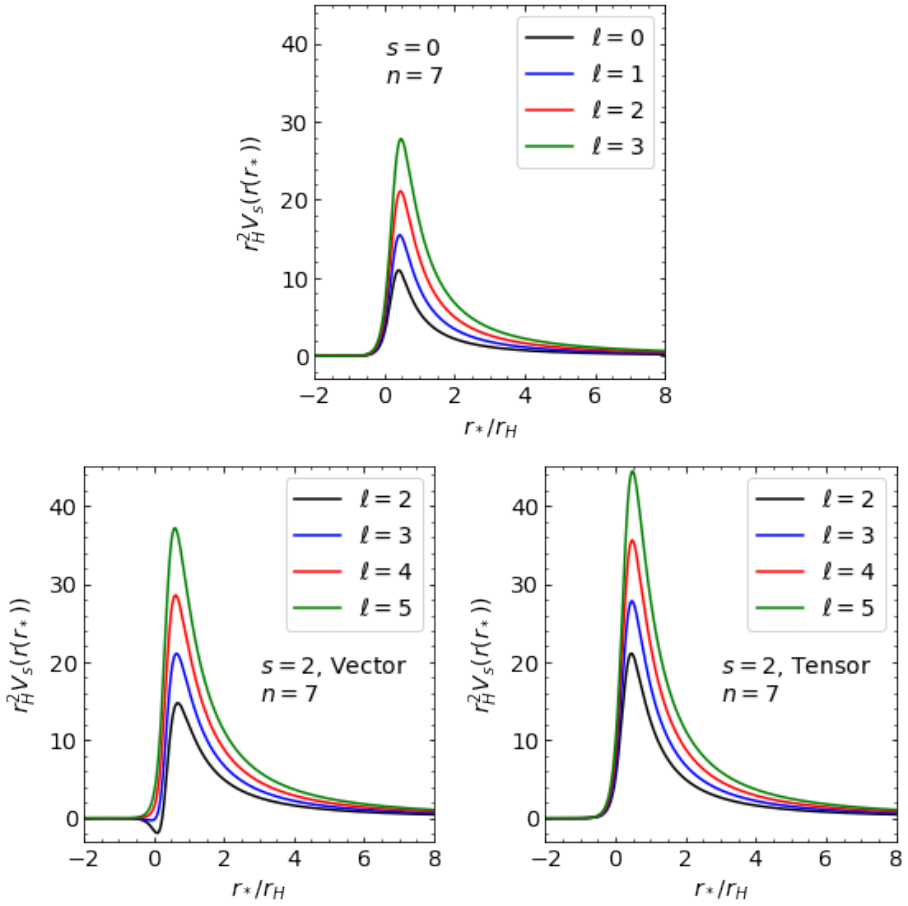

Figure 3.5: Effective potentials for non-commutative black holes in the bulk versus the tortoise coordinate r_* for massless spin 0 and 2 fields and for $n = 7$. A black hole mass of $M = 358M_D$ has been used corresponding to the non-commutative maximum temperature. The peak of the potentials increases with increasing values of ℓ beginning at $\ell = s$. $M_D = \sqrt{\theta} = 1$ has been taken.

3.3 Path-ordered Exponentials

Most attempts to solve the radial equation in the literature are done by using asymptotic matching with the appropriate boundary conditions. The boundary conditions on Eq. (3.13) for a spherically symmetric and static black hole are

$$Z(r_*) = A_{\text{in}} e^{-i\,\omega\, r_*} \quad \text{for } r \longrightarrow r_{\text{r}_\text{H}}, \tag{3.24}$$

and

$$Z(r_*) = B_{\text{in}} e^{-i\,\omega\, r_*} + B_{\text{out}} e^{i\,\omega\, r_*} \quad \text{for } r \longrightarrow \infty, \tag{3.25}$$

where at the horizon we consider only in-going modes to enforce that nothing can escape the black hole. Taking the normalization $A_{\text{in}} = 1$ without loss of generality, we may start with the solution at the horizon Eq. (3.24) and integrate Eq. (3.13) out to infinity where the transmission coefficient $\Gamma(\omega)$ is computed as

$$\Gamma(\omega) = 1 - \left| \frac{B_{\text{out}}}{B_{\text{in}}} \right|^2 . \tag{3.26}$$

Further details of this computation are given in Appendix A.

Alternatively, Gray and Visser [70] proposed a method which involves extracting the transmission coefficients directly via path-ordered exponentials. This is the method we will adopt here and extend it to the geometry of the ST and NC metrics.

Gray et al. showed that the Bogoliubov coefficients relating the incoming and outgoing waves can be directly obtained by the following path-ordered exponential [70]

$$\begin{bmatrix} \alpha & \beta^* \\ \beta & \alpha^* \end{bmatrix} = Pexp\left(-\frac{i}{2\,\omega} \int_{-\infty}^{+\infty} V_s(r_*) \begin{bmatrix} 1 & e^{-2i\,\omega\, r_*} \\ -e^{2i\,\omega\, r_*} & -1 \end{bmatrix} dr_* \right), \tag{3.27}$$

where P is a path ordering operator. Using the product calculus definition of path-ordered integrals, we may compute the Bogoliubov coefficients via the following product integral [70]

$$\begin{bmatrix} \alpha & \beta^* \\ \beta & \alpha^* \end{bmatrix} = \prod_{-\infty}^{+\infty} (I + A(r_*) dr_*), \tag{3.28}$$

where I is the identity matrix and $A(r_*)$ is called the transfer matrix given by

$$A(r_*) = -\frac{i}{2\,\omega} V(r_*) \begin{bmatrix} 1 & e^{-2i\,\omega\,r_*} \\ -e^{2i\,\omega\,r_*} & -1 \end{bmatrix}. \tag{3.29}$$

The path ordering operator P requires that the product integral be calculated such that

$$PA(x_1)A(x_2)... = A(x_{\sigma(1)})A(x_{\sigma(2)})..., \tag{3.30}$$

where $x_{\sigma(1)} \geq x_{\sigma(2)} \geq ...$, i.e. the order in which to multiply is such that the argument of A must be decreasing. The product integral can be approximated numerically by

$$\begin{bmatrix} \alpha & \beta^* \\ \beta & \alpha^* \end{bmatrix} = \lim_{N\to\infty} \left[(I + A(r_{*N-1})h)...(I + A(r_{*1})h)\right], \tag{3.31}$$

where $r_{*i} > r_{*i-1}$ and $h = (r_{*N-1} - r_{*1})/(N-1)$ is the step size. While this expression is straightforward to compute numerically, convergence can sometimes be slow. To improve convergence, we note that Gray [71] recommends using a fifth order approximation from Helton and Stuckwisch

$$\begin{bmatrix} \alpha & \beta^* \\ \beta & \alpha^* \end{bmatrix} = \prod_{k=1}^{N} \left(I + (28K_1 + 32K_2 + 6K_3 + 4K_4 + K_5)/360)\right), \tag{3.32}$$

where

$$K_1 = hA_4, \tag{3.33a}$$

$$K_2 = hA_3\left(4I + K_1)\right), \tag{3.33b}$$

$$K_3 = hA_2\left(8(I - K_1) + 3K_2)\right), \tag{3.33c}$$

$$K_4 = hA_1(32I + 18K_1 + 3hA_2(6I - K_1 + K_2) - 3K_2), \tag{3.33d}$$

$$K_5 = hA_0(28(I - K_1) - 3hA_2(16I + 4K_1 + K_2) + K_4 + 18K_2). \tag{3.33e}$$

The transmission probabilities $\Gamma(\omega)$, are related to the Bogoliubov coefficients by

$$\Gamma(\omega) = \frac{1}{|\alpha(\omega)|^2}. \tag{3.34}$$

Here we emphasize that through this procedure, one does not actually solve numerically a differential equation. Instead, the problem now becomes one of performing a single numerical product integral using finite differences, either Eq. (3.31) or

Eq. (3.32). Numerically for $N = 10^4$ we find that the convergence of Eq. (3.31) is sufficient and we do not require the higher order approximation of Eq. (3.32). We will give more detail on the convergence in later sections.

Chapter 4

Greybody Factors on the Brane

In this section we present the calculations of transmission coefficients, absorption cross sections, and spectra for spin 0, 1/2, 1, and 2 massless fields on the brane. The work in this section has previously been published in Ref. [1] in collaboration with Doug Gingrich. We have validated the method by comparing with well known results for four dimensional Schwarzschild and Kerr black holes, as well as the ST black holes [67, 69] that we use for comparison with the NC results. As noted in previous sections, there are both vector and scalar modes for spin 2 fields which must be treated separately. To allow for comparisons with literature, we only present results for the vector modes for spin 2 fields unless otherwise stated. We provide results for the scalar modes for spin 2 fields in our discussion of isospectrality.

For the NC results, we acknowledge that Ref. [11] inserts a damping factor of $e^{-\frac{1}{2}\theta\omega^2}$ in the equations for the emission rate Eq. (4.6) and number flux Eq. (4.5) as a way to model the effect of an ultra-violet cutoff in the frequency ω. Including this factor gives a subdominant effect [11] and is not particularly relevant to our discussions and will be ignored.

4.1 Parameter Selection

The model of NC geometry inspired black holes in higher dimensions has three unknown parameters n, M_D, and $\sqrt{\theta}$. Typically we present results for each extra dimen-

sion n. Usually it is necessary to fix the other two parameters. One possibility for fixing the parameters is to be guided by experimental constraints. Updating the approach taken in Ref. [27] (see Appendix C) restricts the values of $\sqrt{\theta}M_D$ that can be probed from 0.25 to 0.98, different for each number of extra dimensions. The allowed range in $\sqrt{\theta}M_D$ for any given number of extra dimensions is severely restricted. Calculations using values of $\sqrt{\theta}M_D < 1$ begin to probe the details of the matter smearing distribution and become model dependent. However, the primary goal in this thesis is to study the differences in Hawking emission from NC and ST black holes so we choose the usual condition $M_D = \sqrt{\theta} = 1$. This implies that our phenomenological predictions will not have particular consequence for the physics at the LHC.

We run into some complications when trying to choose dimensionless quantities due to the two scales M_D and $\sqrt{\theta}$ that appear in models of higher dimensional NC geometry inspired black holes. We note that the units in the following plots are not dimensionless and depend on our choice of mass. In general, we plot our results against the frequency ω with $\omega\, r_{\rm H}$ being the dimensionless quantity.

4.2 Transmission Coefficients

The fundamental calculated quantity is the transmission coefficient as a function of frequency for different black hole masses, number of extra dimensions, spin, and ℓ modes. The transmission coefficients are computed numerically using Eq. (3.31) with $N = 10^4$. For numerical stability, the lowest frequency we consider is $\omega = 0.001$, and we consider frequencies up to and including $\omega = 1$. In Figure 4.1 we plot the convergence of the transmission coefficients at various values of ω from NC black holes for the $s = \ell$ modes and for $n = 7$ extra dimensions. A black hole mass of $358M_D$ is used corresponding to the NC black hole maximum temperature. We have followed the procedure of Gray [70] by defining the relative error of the $N^{\rm th}$ approximation as

$$\delta\Gamma_{s,\ell}(\omega) = \frac{\left|\Gamma^{N}_{s,\ell}(\omega) - \Gamma^{N+1}_{s,\ell}(\omega)\right|}{\Gamma^{N}_{s,\ell}(\omega)}. \tag{4.1}$$

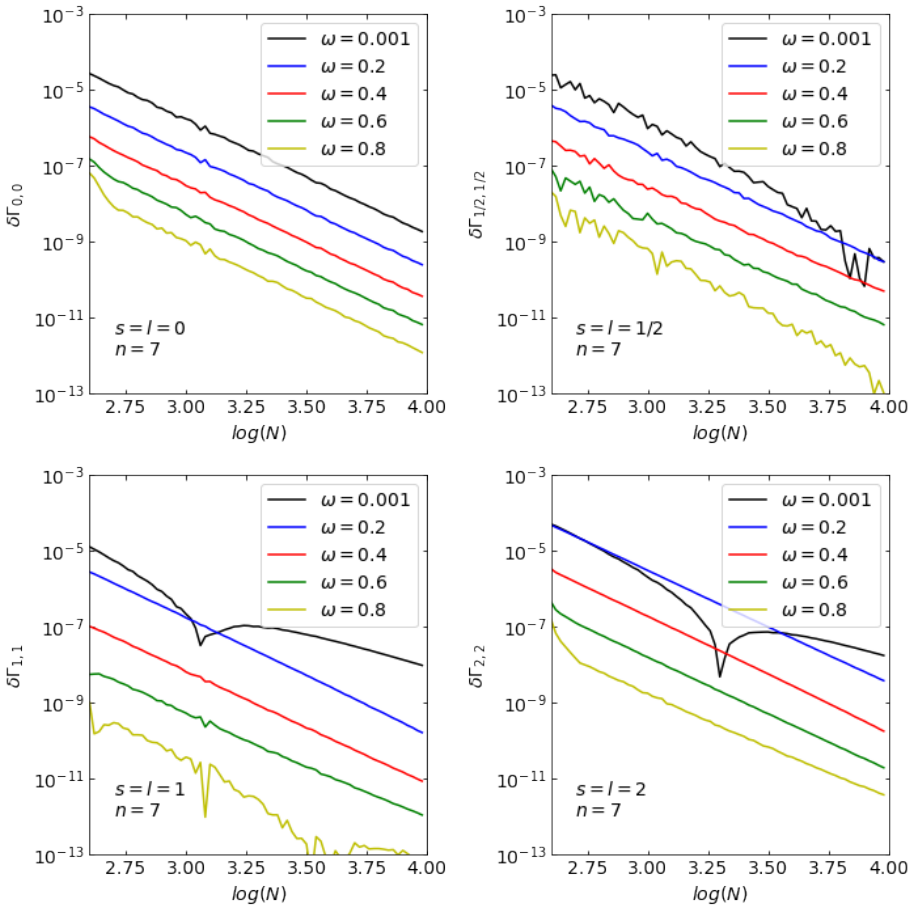

Figure 4.1: Relative error $\delta\Gamma^N_{s,\ell}(\omega)$ of the N^{th} approximation for the $s = \ell = 0, 1/2, 1, 2$ modes on the brane as a function of N for various values of the frequency ω. A black hole mass of $358M_D$ has been used corresponding to the non-commutative maximum temperature. $M_D = \sqrt{\theta} = 1$ has been taken.

Numerically for $N = 10^4$, we find that we introduce an error of at worst $\sim 10^{-8}$ for the $s = \ell$ modes. The convergence generally improves with increasing values of ω. For the lowest frequency that we consider of $\omega = 0.001$, we observe that the convergence for the spin 1 and 2 cases temporarily worsens past a certain value of N, and then continues to improve. This behaviour does not exist for the spin 0 and 1/2 cases. One reason as to which we may attribute this behaviour is due to the fact that the $s = \ell$ modes at $\omega = 0$ are non-zero for the spin 0 and 1/2 cases while they are zero for the spin 1 and 2 cases. Since the spin 1 and 2 cases are effectively zero, truncation errors may become more prominent in the product integral, leading to a temporary

reduction in the convergence.

Figure 4.2 shows transmission coefficients for $n = 7$ and $s = 0, 1/2, 1, 2$ as a function of frequency for different ℓ modes. The solid lines are for NC black holes and dashed lines for ST black holes. The quantum number ℓ increases from $\ell = s$ going from left to right. A black hole mass of $358M_D$ is used and corresponds to the NC black hole maximum temperature. We observe that the NC and ST black hole transmissions coefficients at this mass are very similar, differing slightly for higher ℓ. This is because they have a similar horizon radius at this mass of 5.68 for NC black holes and 5.76 for ST black holes.

If the horizon radius difference between NC and ST black holes is significantly different, the comparison changes. Figure 4.3 shows transmission coefficients for $n = 7$ and $s = 0, 1/2, 1, 2$ as a function of frequency for different ℓ modes. A black hole mass of $358M_D$ and $924M_D$ are used for the NC black hole and ST black hole, respectively, corresponding to the NC black hole maximum temperature. In this case, significant differences are observed for a horizon radius of 5.68 for NC black holes and 6.48 for ST black holes.

To examine more significant differences in transmission coefficients, a value for the black holes mass at the minimum NC black hole mass can be chosen and is shown in Figure 4.4. The horizon radius of the NC black hole is 2.32 and that of the ST black hole 4.02. We observe significant differences between NC and ST black hole transmission coefficients with increasing ℓ. The NC black hole transmission probabilities begin to rise at higher frequencies but rise more steeply than the ST transmission probabilities. This behaviour was first observed for spin 0 in Ref. [11].

The number of effective ℓ modes used in the calculations can vary. The total number of ℓ modes considered are 15, 15, 14, 13 for $s = 0, 1/2, 1, 2$, respectively. The number of effective ℓ modes giving a non-negligible contribution in the frequency range $0.001 \leq \omega \leq 1$ is different depending on M, n, and s. Typically, $s = 0$ and $1/2$ have the same number of effective modes, while $s = 1$ has one less and $s = 2$ has

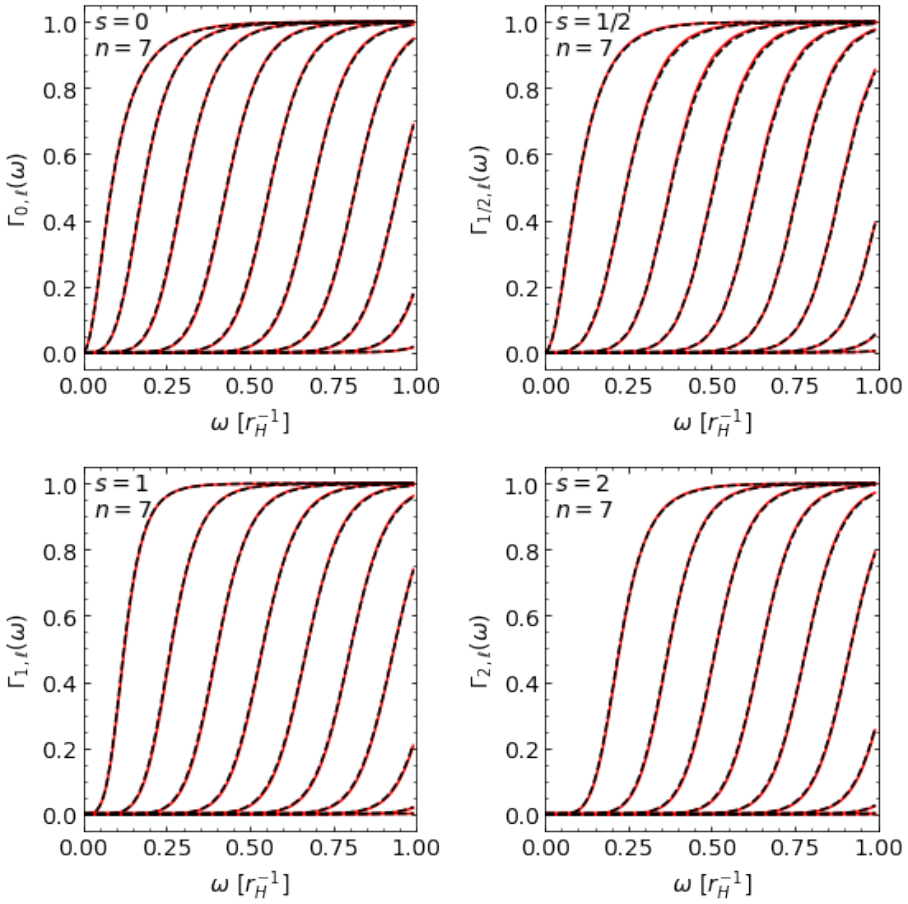

Figure 4.2: Transmission coefficients $\Gamma_{s,\ell}(\omega)$ on the brane for $s = 0, 1/2, 1, 2$ as a function of frequency ω. The quantum number ℓ increases from $\ell = s$ going from left to right. The red solid lines are for non-commutative black holes and the black dashed lines for Schwarzschild-Tangherlini black holes. A black hole mass of $358M_D$ has been used corresponding to the non-commutative maximum temperature. $M_D = \sqrt{\theta} = 1$ has been taken.

two less modes. The $s = 1$ and 2 cases have transmission coefficients that turn-on at higher frequencies relative to the $s = 0$ and $1/2$ cases, i.e. because of $\ell \geq s$, the higher spins are missing the lower ℓ modes. As n increases, the transmission coefficients become more spread out, and thus less modes will contribute to the given frequency range. The $n = 0$ case has about four more modes than $n = 7$. The lowest masses we consider will have about three less effective modes than the highest masses we consider. The number of effective modes that will fit into the frequency range is largely determined by the spacing of the transmission coefficients in frequency.

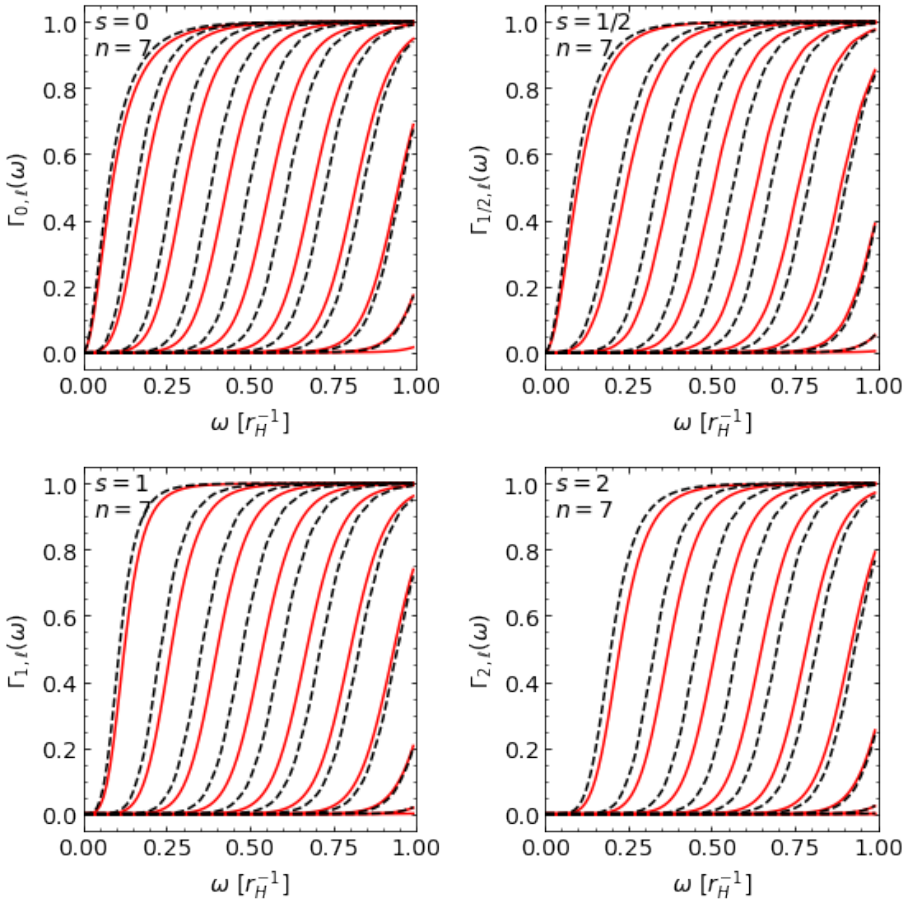

Figure 4.3: Transmission coefficients $\Gamma_{s,\ell}(\omega)$ on the brane for $s = 0, 1/2, 1, 2$ as a function of frequency ω. The quantum number ℓ increases from $l = s$ going from left to right. The red solid lines are for non-commutative black holes with $M = 358M_D$ corresponding to the non-commutative maximum temperature. The black dashed lines are for Schwarzschild-Tangherlini black holes with $M = 924M_D$ corresponding to a black hole with a temperature equal to the non-commutative maximum temperature. A black hole temperature of $0.098M_D$ has been used and $M_D = \sqrt{\theta} = 1$ taken.

Another important characteristic of the transmission coefficients is how steeply they rise with increasing frequency. In general, the turn-on steepness is largely independent of spin except for the $\ell = 0$ and 1 modes. The more effective number of modes, the steeper the turn-on. Visually, the turn-on is most steep for $s = 1$ and less step for $s = 2$.

The differences in transmission coefficients between NC and ST black holes depend significantly on their relative horizon radii. Typically a bigger horizon radius will give

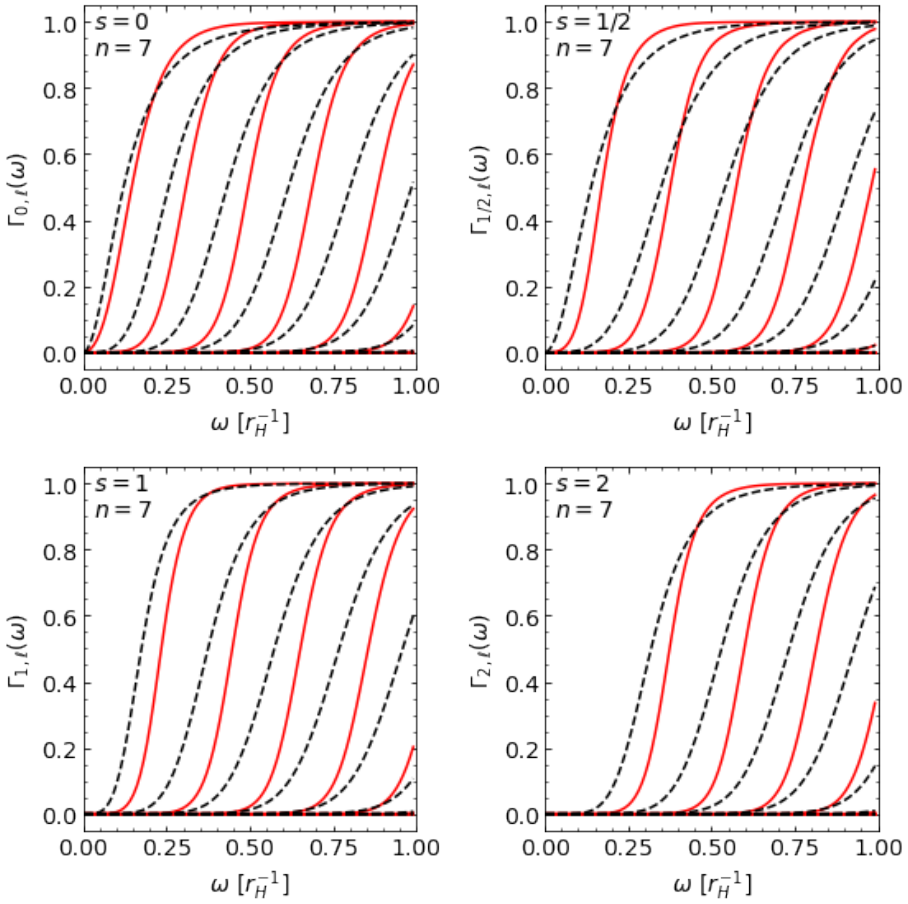

Figure 4.4: Transmission coefficients $\Gamma_{s,\ell}(\omega)$ on the brane for $s = 0, 1/2, 1, 2$ as a function of frequency ω. The quantum number ℓ increases from $\ell = s$ going from left to right. The red solid lines are for non-commutative black holes and black dashed lines for Schwarzschild-Tangherlini black holes. A black hole mass of $20.4M_D$ has been used corresponding to the non-commutative minimum temperature. $M_D = \sqrt{\theta} = 1$ has been taken.

transmission coefficients that turn-on lower in frequency; the difference becoming more pronounced as ℓ increases. In addition, it is observed that at lower masses although the ST black hole transmission coefficients turn-on sooner, the NC black hole coefficients rise steeper and become higher before plateauing to unity, especially for $s = 1/2$.

4.3 Absorption Cross Sections

Another physically important quantity concerning Hawking evaporation is the absorption cross section $\sigma(\omega)$, which represents an effective area embodying the likelihood of a particle to be scattered by the black hole [71]. On the brane, the absorption cross section depends on the weighted sum over ℓ of transmission coefficients and inversely as $1/\omega^2$

$$\sigma(\omega) = \frac{\pi}{\omega^2} \sum_{\ell \geq s} (2\ell + 1) \Gamma_{s,\ell}(M; \omega). \tag{4.2}$$

Figure 4.5 shows cross sections versus frequency for $s = 0, 1/2, 1, 2$. The solid lines are for NC black holes and dashed lines for ST black holes. Black hole masses corresponding to the NC black hole maximum temperature have been used; equal NC and ST black hole masses, M_{eM} in Table 2.2. Differences in cross sections are observed at low frequencies. These differences are most significant for $s = 1/2$ and less pronounced for $s = 2$.

Hawking radiation for spin-2 fields in the ST metric was first discussed by Park [67]. Direct comparison is not possible since we use a different effective potential which is taken from Ref. [63] but originally came from Ref. [72]. The difference in the general form of the potential appears significant but when substituting the particular ST metric, the difference is replacing the -1 coefficient of the second term in Eq. (3.14d) by $-(n+1)$. Noteworthy in Ref. [67] is the acknowledgement that the spin-2 potential can become negative – potential well – for some masses (or radii), number of extra dimensions, and ℓ modes. The potential well can occur in the region $r_* \sim 0$. For the ST metric, the condition for non-negative potential is $n \leq 3$. If $4 \leq n \leq 7$, the $\ell = 2$ mode feel a potential well. The depth of the potential well, and height of the barrier, increase with increasing number of extra dimensions. A trade-off can occur between barrier suppression and well enhancement. For the ST case, this causes the $n = 5$–7 spin-2 cross sections to rise slightly faster at low-frequency than the $n = 0$–4 cross sections. The same observations are made for the NC case. However, the effect is

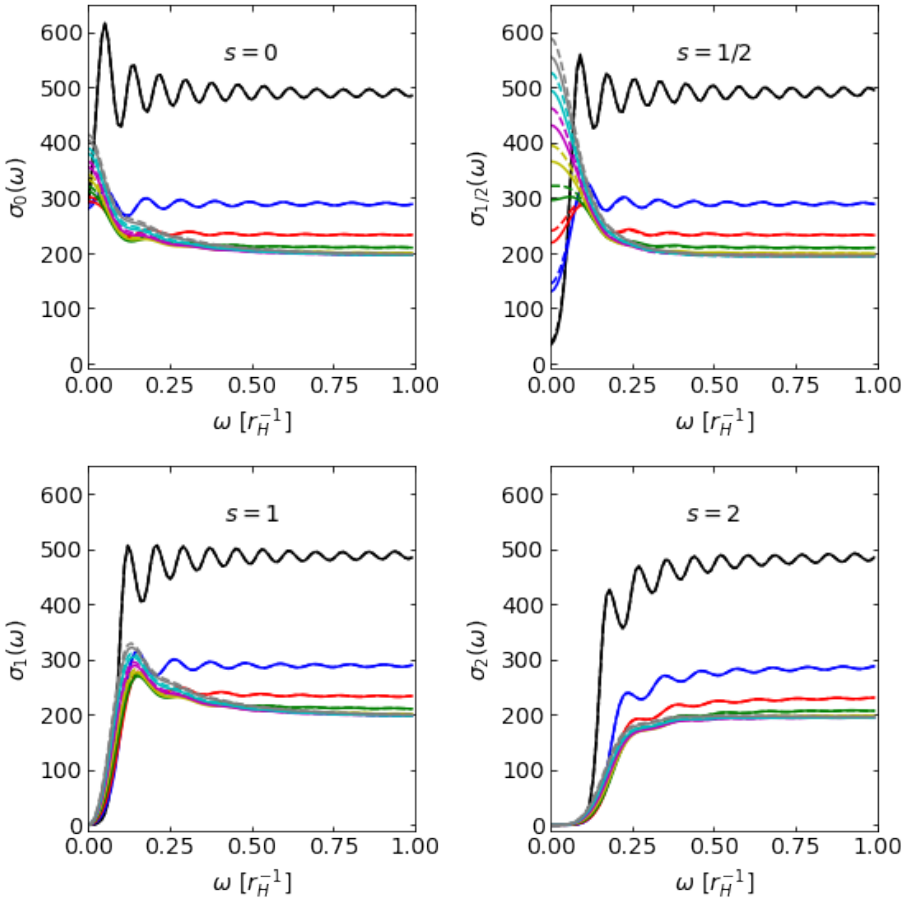

Figure 4.5: Absorption cross sections on the brane versus frequency ω for $s = 0, 1/2, 1, 2$. The solid lines are for non-commutative black holes and dashed lines for Schwarzschild-Tangherlini black holes. The number of extra dimensions increases from 0 to 7 as the curves moved from top to bottom at high ω. Black hole masses corresponding to the non-commutative black hole maximum temperature have been used. $M_D = \sqrt{\theta} = 1$ has been taken.

small and will not concern use for the remainder of this thesis.

The differences in Figure 4.5 at low frequency are predominately due to differences in horizon area. It is enlightening to effectively remove these by scaling the cross sections by $4\pi r_{\rm H}^2$ as shown in Figure 4.6. The cross sections are now in better agreement for $\omega \lesssim 0.25$ but have almost constant residual differences for $\omega \gtrsim 0.25$. These differences are due to the universal nature of the cross section – to be discussed later.

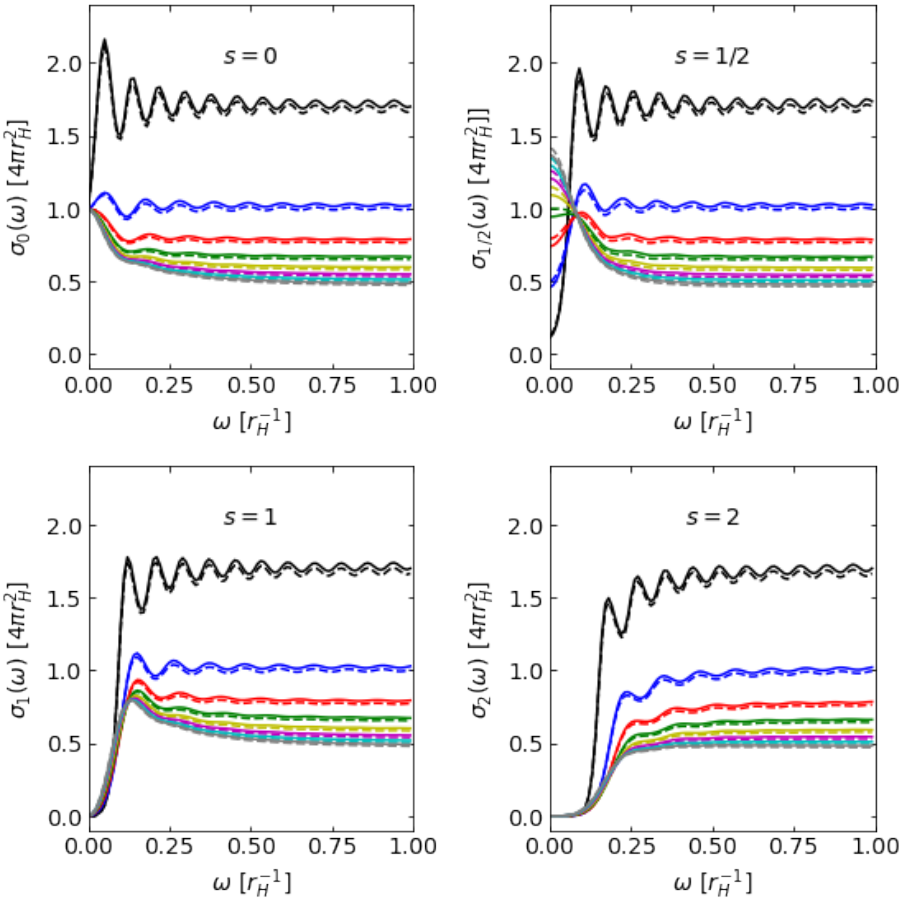

Figure 4.6: Normalized absorption cross sections on the brane versus frequency ω for $s = 0, 1/2, 1, 2$. The solid lines are for non-commutative black holes and dashed lines for Schwarzschild-Tangherlini black holes. The number of extra dimensions increases from 0 to 7 as the curves moved from top to bottom at high ω. Black hole masses corresponding to the non-commutative black hole maximum temperature have been used. $M_D = \sqrt{\theta} = 1$ has been taken.

At the mass giving maximum NC black hole temperature, the horizon radius of the NC and ST black holes are similar. To examine larger differences due to the

transmission coefficients, we take masses near the minimum NC back hole horizon as shown in Table 2.1. Figure 4.7 shows significant differences for all but the low n cases.

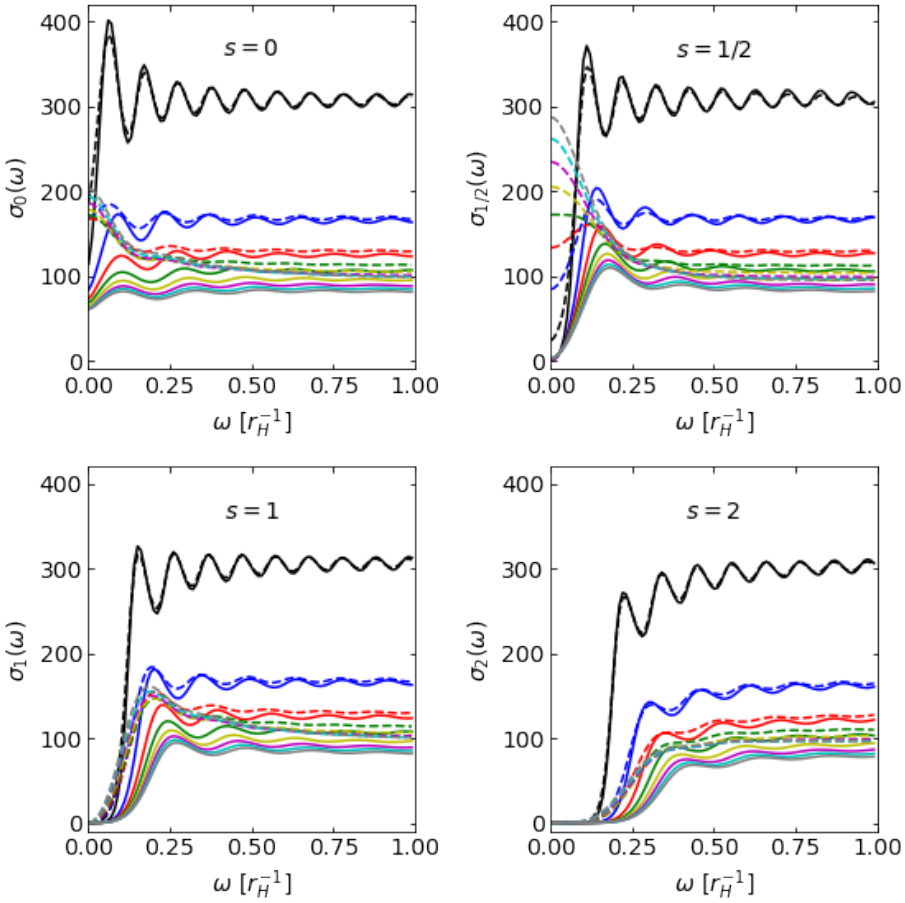

Figure 4.7: Absorption cross sections on the brane versus frequency ω for $s = 0, 1/2, 1, 2$. The solid lines are for non-commutative black holes and dashed lines for Schwarzschild-Tangherlini black holes. The number of extra dimensions increases from 0 to 7 as the curves moved from top to bottom at high ω. Black hole masses corresponding to the non-commutative black hole minimum mass $M_{\min}$ have been used. $M_D = \sqrt{\theta} = 1$ has been taken.

For ST black holes, the absorption cross section results are the same as Ref. [69]. Although the absorption cross section results for NC black holes and $s = 0$ agree qualitatively with Ref. [11], they are quantitatively different due to different units.

The transmission coefficients for spin 0 and 1/2 turn on immediately for low frequencies, leading to finite absorption cross sections at zero frequency. Transmission

coefficients for spin 1 and 2 are essentially zero at $\omega = 0$, leading to an absorption cross section of zero at zero frequency. The usual oscillations are seen and the number of peaks correspond to the number of ℓ modes. The oscillation are more predominate at low n where the transmission coefficients rise the steepest. After normalizing by the horizon radius, the absorption cross sections for NC black holes are higher than the ST back hole at high frequencies.

For spin 0, the low-frequency limit should correspond to the area of the black hole for both ST and NC black holes: $\sigma_0(0) = 4\pi r_{\rm H}^2$. Numerically, for $\omega = 0.001$, we obtain the black hole area to better than 0.9% for both ST and NC black holes for high and low mass and for all number of dimensions and spins; except for $n = 0$ for which it agrees to 1.7% for ST black holes of mass M_{eT}. For spin 1/2, the low-frequency limit for ST black holes is given by [73]

$$\sigma_{(1/2)}(0) = 2^{\frac{n-3}{n+1}} 4\pi r_{\rm H,ST}^2 \,, \tag{4.3}$$

where $r_{\rm H,ST}$ is the ST horizon radius. We are able to reproduce $\sigma_{(1/2)}(0)$ numerically to better than 0.4%, except for the $n = 0$ case in which we obtain 2% agreement. In the high-frequency limit, it has been shown that the absorption cross section approaches a universal geometrical optics limit of $\sigma_\infty = \pi b_c^2$, where $b_c = r_c/\sqrt{h(r_c)}$ and r_c is the radius of the photon sphere given by the solution to $r_c h'(r_c) - 2h(r_c) = 0$ [74]. Using the ST metric, one obtains

$$\sigma_\infty = \left(\frac{n+3}{2}\right)^{\frac{2}{n+1}} \frac{n+3}{n+1} \pi r_{\rm H,ST}^2. \tag{4.4}$$

This result was first obtained in Ref. [75]. In the case of the NC metric, we have calculated σ_∞ numerically. For $\omega = 1$, we obtain the optical cross section for ST and NC black holes to better than 3% for high mass, all number dimensions, and all spins. For low mass, the NC accuracy remains but the ST $n = 7$ and $s = 1$ case worsens by up to 5%. Visually, we already approach the geometrical limit for $\omega \gtrsim 0.25$. Reproducing these known analytical values is a good test of the numerical

validity of our calculations.

4.4 Particle Spectra

The particle spectra, or number of particles N emitted per unit time and per unit frequency on the brane is

$$\frac{d^2N}{dtd\omega} = \frac{1}{2\pi}\frac{1}{e^{\frac{\omega}{T_{\rm H}}} - (-1)^{2s}}\sum_{\ell \geq s}(2\ell+1)\,\Gamma_{s,\ell}(M;\omega). \tag{4.5}$$

The particle spectra have an additional dependence on temperature and the dependence on frequency is only indirectly through the sum of transmission coefficients and the statistical factor. This time it is not possible to take the minimum NC black hole mass (zero temperature) as the spectra will vanish due to the statistical factor. An interesting choice is to take the NC black hole mass at its maximum temperature. For the ST black hole comparison, logical choices are to take the same mass or the mass that gives the same temperature. If the same temperature is taken, the statistical factor in the particle spectra will be identical and the only difference will be the transmission coefficient sum part of the formula. First, we consider the case of equal mass which means the temperature of the ST black hole will be hotter, and hence lead to significantly more particle flux. Figure 4.8 shows particle spectra versus frequency for $s = 0, 1/2, 1$, and 2. The solid lines are for NC black holes and dashed lines for ST black holes. The number of extra dimensions increases from 0 to 7 as the curves move from bottom to top. Black hole masses $M_{\mathrm{e}M}$ corresponding to the NC black hole maximum temperature have been used, as shown in Table 2.2.

To remove the temperature dependence, different mass NC and ST black holes are compared. Figure 4.9 shows particle spectra versus frequency. Black hole masses $M_{\mathrm{e}M}$ for NC black holes and $M_{\mathrm{e}T}$ for ST black holes corresponding to the NC black hole maximum temperature have been used, as shown in Table 2.2.

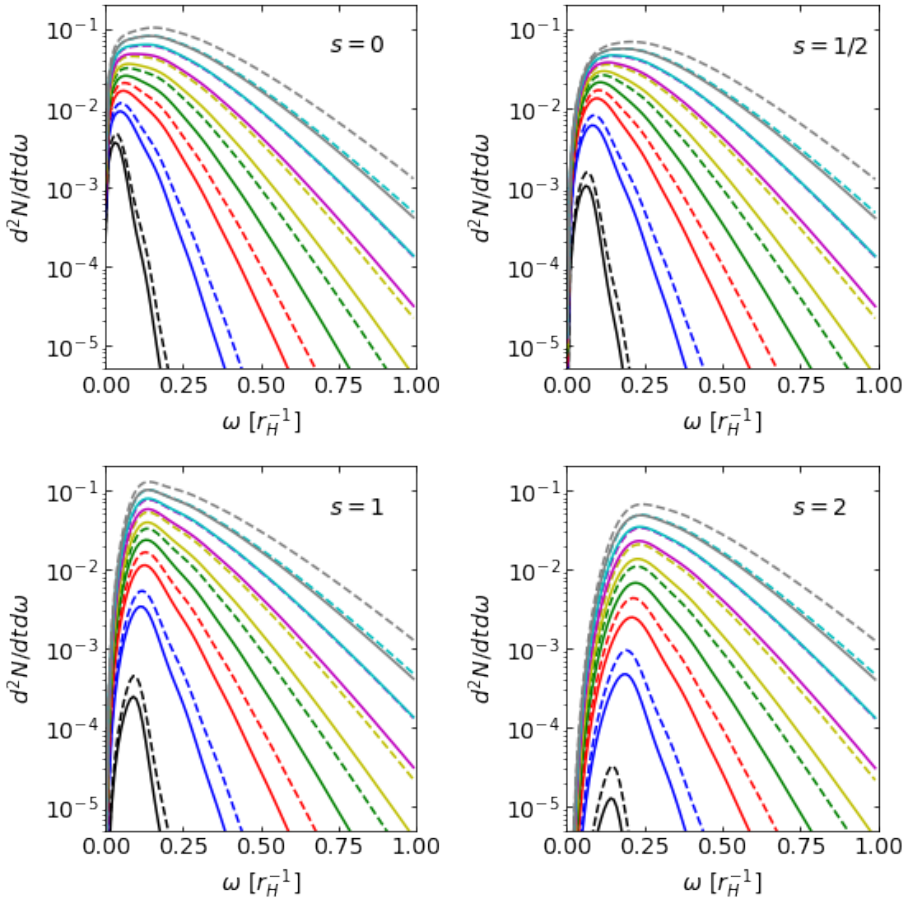

Figure 4.8: Particle spectra on the brane versus frequency ω for $s = 0, 1/2, 1, 2$. The solid lines are for non-commutative black holes and dashed lines for Schwarzschild-Tangherlini black holes. The number of extra dimensions increases from 0 to 7 as the curves move from bottom to top. Black hole masses corresponding to the non-commutative black hole maximum temperature have been used. $M_D = \sqrt{\theta} = 1$ has been taken.

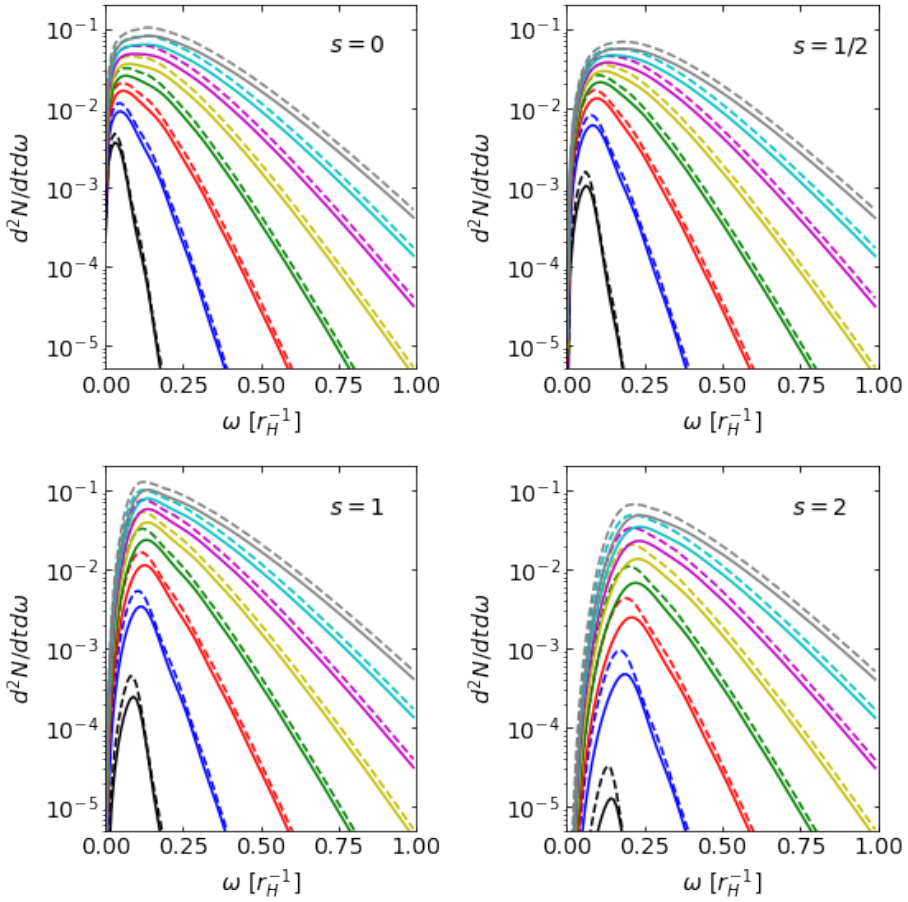

Figure 4.9: Particle spectra on the brane versus frequency ω for $s = 0, 1/2, 1, 2$. The solid lines are for non-commutative black holes and dashed lines for Schwarzschild-Tangherlini black holes. The number of extra dimensions increases from 0 to 7 as the curves move from bottom to top. Black hole masses corresponding the same temperature as the non-commutative black hole maximum temperature have been used. $M_D = \sqrt{\theta} = 1$ has been taken.

4.5 Energy Spectra

The energy E spectra are similar to the particle spectra but include a multiplicative frequency factor

$$\frac{d^2E}{dtd\omega} = \frac{\omega}{2\pi}\frac{1}{e^{\frac{\omega}{T_{\rm H}}} - (-1)^{2s}}\sum_{\ell\geq s}(2\ell+1)\,\Gamma_{s,\ell}(M;\omega). \tag{4.6}$$

Figure 4.10 shows energy spectra versus frequency for $s = 0, 1/2, 1$ and 2. The solid lines are for NC black holes and dashed lines for ST black holes. The number of extra dimensions increases from 0 to 7 as the curves move from bottom to top. Black hole masses $M_{{\rm e}M}$ corresponding to the NC black hole maximum temperature have been used, as shown in Table 2.2.

To remove the temperature dependence, different mass NC and ST black holes are compared. Figure 4.11 shows energy spectra versus frequency. Black hole masses $M_{{\rm e}M}$ for NC black holes and $M_{{\rm e}T}$ for ST black holes corresponding to the NC black hole maximum temperature have been used, as shown in Table 2.2.

4.6 Particle Flux and Total Power

To make the comparison quantitative, we integrate the particle spectra and energy spectra over frequency out to $\omega = 1$ to obtain the particle flux and power, respectively. Table 4.1 and Table 4.2 show the NC to ST particle flux ratios for the cases of equal mass and equal temperature, respectively. We observe the ratio of spin 0 and 1 fields are not very sensitive to number of extra dimensions for $n > 0$. The biggest change in particle flux ratio with number of dimensions is for spin 2.

Table 4.3 and Table 4.4 show the NC to ST power ratios for the cases of equal mass and equal temperature, respectively. The same observations can be made as for the particle fluxes.

Concentrating on NC geometry inspired black holes, we calculate the particle flux and total power for each number of extra dimensions and compare it to the $n = 0$

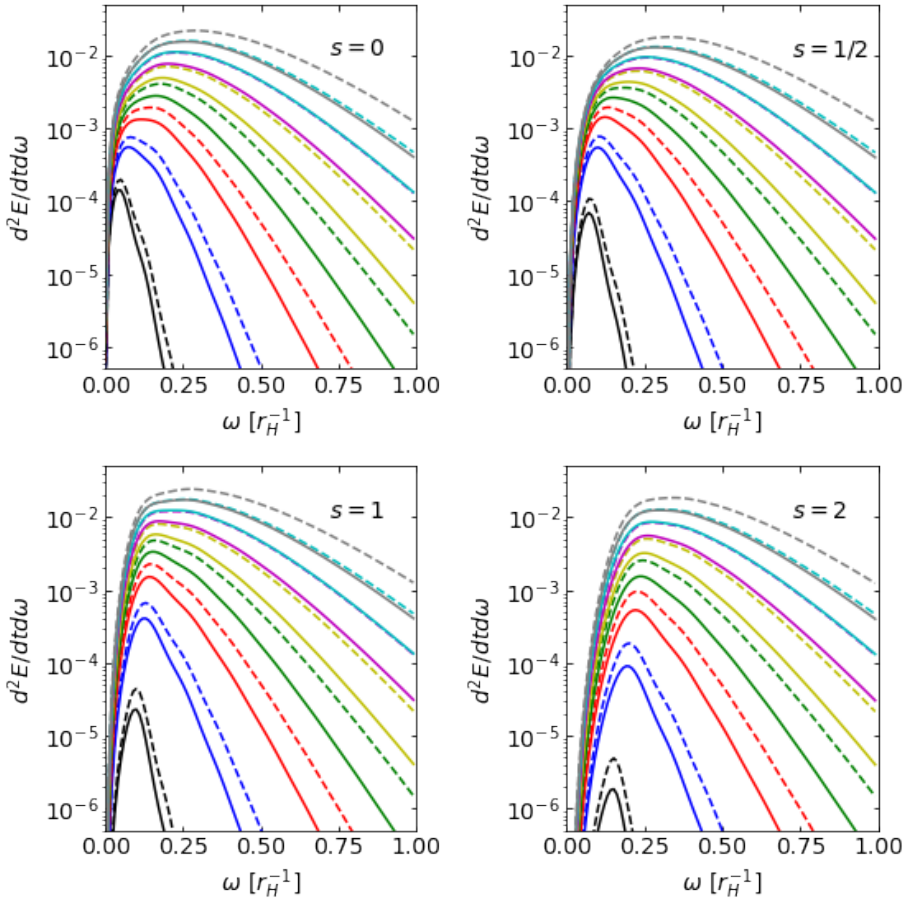

Figure 4.10: Energy spectra on the brane versus frequency ω for $s = 0, 1/2, 1, 2$. The solid lines are for non-commutative black holes and dashed lines for Schwarzschild-Tangherlini black holes. The number of extra dimensions increases from 0 to 7 as the curves move from bottom to top. Black hole masses corresponding to the non-commutative black hole maximum temperature have been used. $M_D = \sqrt{\theta} = 1$ has been taken.

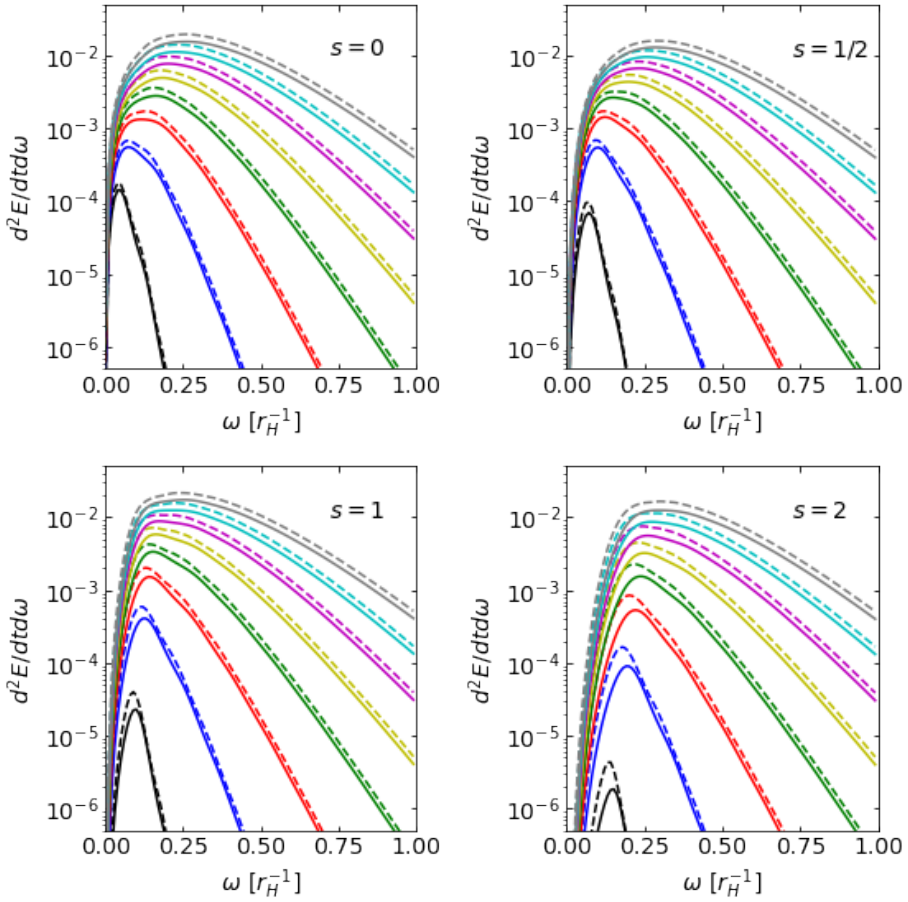

Figure 4.11: Energy spectra on the brane versus frequency ω for $s = 0, 1/2, 1, 2$. The solid lines are for non-commutative black holes and dashed lines for Schwarzschild-Tangherlini black holes. The number of extra dimensions increases from 0 to 7 as the curves move from bottom to top. Black hole masses corresponding to the same temperature as the non-commutative black hole maximum temperature have been used. $M_D = \sqrt{\theta} = 1$ has been taken.

Table 4.1: Ratio of particle flux from non-commutative to Schwarzschild-Tangherlini black holes on the brane versus spin s and number of extra dimensions n at the mass of the non-commutative black hole of maximum temperature, $M_{\mathrm{e}M}$.

	n							
s	0	1	2	3	4	5	6	7
0	0.73	0.71	0.70	0.70	0.70	0.70	0.70	0.71
1/2	0.65	0.69	0.70	0.71	0.71	0.72	0.72	0.72
1	0.54	0.60	0.63	0.65	0.67	0.68	0.69	0.69
2	0.40	0.49	0.53	0.57	0.59	0.61	0.63	0.64

Table 4.2: Ratio of particle flux from non-commutative to Schwarzschild-Tangherlini black holes on the brane versus spin s and number of extra dimensions n at masses corresponding to the non-commutative black hole maximum temperature: $M_{\mathrm{e}M}$ for non-commutative and $M_{\mathrm{e}T}$ for Schwarzschild-Tangherlini black holes.

	n							
s	0	1	2	3	4	5	6	7
0	0.80	0.79	0.79	0.79	0.79	0.79	0.79	0.79
1/2	0.71	0.77	0.79	0.80	0.80	0.81	0.81	0.81
1	0.59	0.67	0.71	0.74	0.75	0.76	0.77	0.78
2	0.44	0.54	0.60	0.64	0.67	0.69	0.71	0.72

Table 4.3: Ratio of power emitted from non-commutative to Schwarzschild-Tangherlini black holes on the brane versus spin s and number of extra dimensions n at the mass of the non-commutative black hole of maximum temperature, $M_{\mathrm{e}M}$.

	n							
s	0	1	2	3	4	5	6	7
0	0.67	0.64	0.62	0.62	0.62	0.62	0.63	0.63
1/2	0.61	0.63	0.63	0.63	0.63	0.63	0.64	0.64
1	0.51	0.57	0.59	0.60	0.61	0.62	0.63	0.63
2	0.39	0.46	0.50	0.53	0.55	0.57	0.59	0.60

case shown in Table 4.5 and Table 4.6, respectively. Direct comparison with Ref. [69] of the results for ST black holes (not shown) is not possible since the black hole mass used is not stated. The results are however, similar.

Shown in Table 4.7 and Table 4.8 are the case of particle flux and power for each spin compared to the spin-0 case. Direct comparison with Ref. [69] of the results for ST black holes (not shown) is not possible since the black hole mass used is not

Table 4.4: Ratio of power emitted from non-commutative to Schwarzschild-Tangherlini black holes on the brane versus spin s and number of extra dimensions n at masses corresponding to the non-commutative black hole maximum temperature: M_{eM} for non-commutative and M_{eT} for Schwarzschild-Tangherlini black holes.

	n							
s	0	1	2	3	4	5	6	7
0	0.82	0.80	0.79	0.79	0.79	0.79	0.79	0.80
1/2	0.74	0.79	0.80	0.80	0.80	0.80	0.81	0.81
1	0.63	0.71	0.75	0.77	0.78	0.79	0.79	0.80
2	0.47	0.58	0.64	0.68	0.70	0.72	0.74	0.75

Table 4.5: Particle flux ratios on the brane for different number of extra dimensions n relative to $n = 0$ versus spin s for non-commutative black holes with the maximum temperature.

	n							
s	0	1	2	3	4	5	6	7
0	1	5	12	25	44	69	101	141
1/2	1	10	29	61	104	160	230	312
1	1	22	93	235	459	772	1179	1685
2	1	59	406	1354	3189	6149	10412	16131

Table 4.6: Power emission ratios on the brane for different number of extra dimensions n relative to $n = 0$ versus spin s for non-commutative black holes with the maximum temperature.

	n							
s	0	1	2	3	4	5	6	7
0	1	9	32	84	174	316	519	794
1/2	1	15	60	153	311	551	887	1334
1	1	30	160	469	1031	1916	3187	4899
2	1	82	668	2512	6494	13504	24379	39872

stated. However, the results are the same as Ref. [69] for most cases, except for a difference of 1% for some $n = 7$ spins.

Table 4.7: Particle flux ratios on the brane for different spin s relative to $s = 0$ versus number of extra dimensions n for non-commutative black holes with the maximum temperature.

n	$s = 0$	$s = 1/2$	$s = 1$	$s = 2$
0	1	0.33	0.08	0.005
1	1	0.68	0.38	0.06
2	1	0.78	0.62	0.15
3	1	0.79	0.77	0.25
4	1	0.78	0.87	0.33
5	1	0.76	0.93	0.41
6	1	0.74	0.97	0.47
7	1	0.73	0.99	0.53

Table 4.8: Power emission ratios on the brane for different spin s relative to $s = 0$ versus number of extra dimensions n for non-commutative black holes with the maximum temperature.

n	$s = 0$	$s = 1/2$	$s = 1$	$s = 2$
0	1	0.50	0.17	0.01
1	1	0.86	0.61	0.14
2	1	0.92	0.86	0.30
3	1	0.91	0.97	0.44
4	1	0.89	1.03	0.55
5	1	0.87	1.05	0.63
6	1	0.85	1.06	0.69
7	1	0.84	1.07	0.74

4.7 Isospectrality

Now we turn our attention to the matter of isospectrality for NC black holes. In four dimensions for Schwarzschild black holes, it is well known that the the scalar and vector perturbations for massless spin 2 fields produce the same emission spectra and quasi-normal modes [76]. Isospectrality does not generally hold for other metrics, such as for the higher dimensional ST case [61], and thus we would not expect it to hold for the higher-dimensional NC case. We are not aware of any literature that has reported on the isospectrality of NC black holes. In Figure 4.12, we plot the transmission coefficients in the NC case for scalar and vector spin 2 modes for $n = 0$

and $n = 7$ as a function of frequency for different ℓ modes. The solid lines are for vector spin 2 modes and the dashed lines for scalar spin 2 modes The quantum number ℓ increases from $\ell = s$ going from left to right. A black hole mass of $358M_D$ is used and corresponds to the NC black hole maximum temperature. We observe that in four dimensions, the transmissions coefficients for scalar and vector modes lie nearly on top of each other. In higher dimensions, we observe differences in the scalar and vector modes, particularly for the $s = \ell = 2$ mode. For $n > 3$, this may be explained by the appearance of the potential well in the potential for vector modes which causes the transmission coefficients to turn on sooner as compared to the scalar modes. Scalar modes do not feel a potential well in any mass or number of extra dimensions.

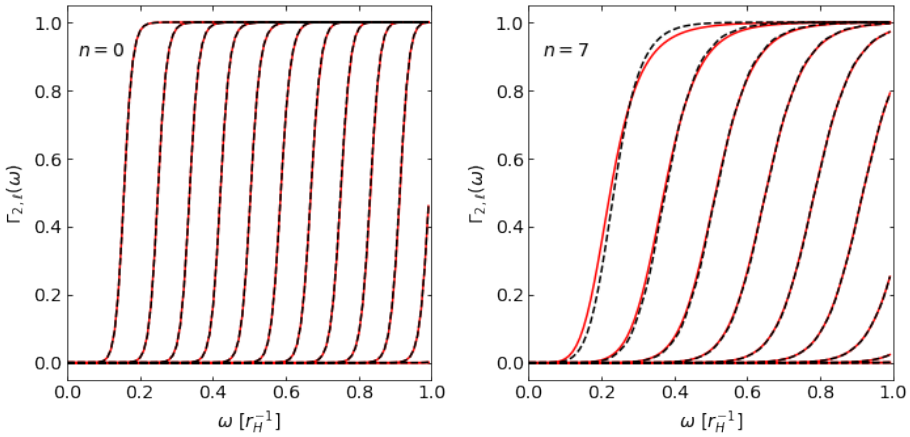

Figure 4.12: Transmission coefficients $\Gamma_{s,\ell}(\omega)$ for spin 2 scalar and vector modes on the brane from non-commutative black holes as a function of frequency ω for $n = 0$ (left) and $n = 7$ (right) extra dimensions. The quantum number ℓ increases from $\ell = s$ going from left to right. The red solid lines are for vector modes and the black dashed lines for scalar modes. A black hole mass of $358M_D$ has been used corresponding to the non-commutative maximum temperature. $M_D = \sqrt{\theta} = 1$ has been taken.

The absorption cross sections versus frequency for scalar and vector modes are shown in Figure 4.13. The solid lines are for vector modes and dashed lines for scalar modes. Black hole masses corresponding to the NC black hole maximum temperature have been used. In four dimensions, the cross sections appear to be exactly on top

of each other. In higher dimensions, differences in cross sections are observed at low frequencies. The high frequency behaviour is similar for both vector and scalar modes. At $\omega = 1$, we observe that the agreement between vector and scalar modes is better than 6×10^{-9} for $n = 0$ and 5×10^{-6} for $1 \leq n \leq 7$.

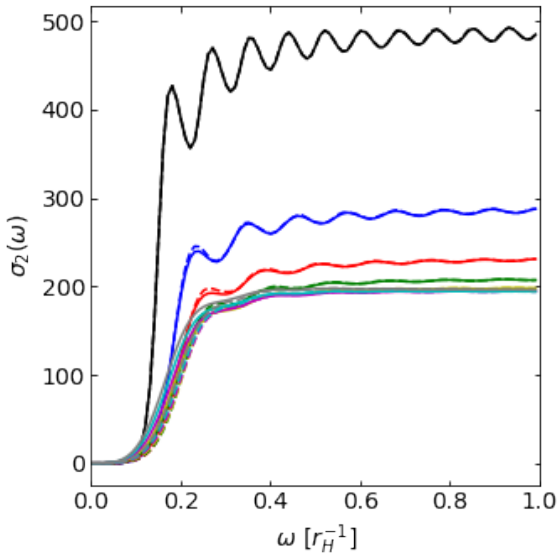

Figure 4.13: Absorption cross sections versus frequency ω for spin 2 scalar and vector modes on the brane from non-commutative black holes. The solid lines are for vector modes and the dashed lines for scalar modes. The number of extra dimensions increases from 0 to 7 as the curves moved from top to bottom at high ω. Black hole masses corresponding to the non-commutative black hole maximum temperature have been used. $M_D = \sqrt{\theta} = 1$ has been taken.

Figures 4.14 and 4.15 shows particle spectra and emission spectra, respectively, versus frequency for $s = 2$ scalar and vector modes from NC black holes. The solid lines are for vector modes and the dashed lines for scalar modes. The number of extra dimensions increases from 0 to 7 as the curves moved from bottom to top at high ω. Black hole masses corresponding to the NC black hole maximum temperature have been used. $M_D = \sqrt{\theta} = 1$ has been taken. Black hole masses M_{eM} corresponding to the NC black hole maximum temperature have been used, as shown in Table 2.2.

We find that for both the particle and energy spectra, the scalar and vector modes lie nearly exactly on top of each other in four dimensions. In higher dimensions, there

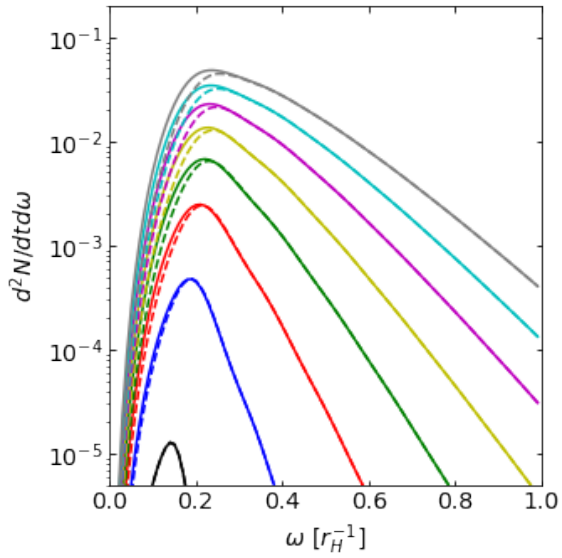

Figure 4.14: Particle spectra on the brane versus frequency ω for $s = 2$ scalar and vector modes. The solid lines are for vector modes and the dashed lines for scalar modes. The number of extra dimensions increases from 0 to 7 as the curves move from bottom to top. Black hole masses corresponding to the non-commutative black hole maximum temperature have been used. $M_D = \sqrt{\theta} = 1$ has been taken.

are differences between the scalar and vector modes at low frequencies, while the high frequency behaviour is similar. To make the comparison quantitative, we integrate the particle spectra over frequency out to $\omega = 1$ to obtain the particle flux and power, respectively. Table 4.9 shows the power emission ratios of spin 2 vector to scalar modes for the cases of equal mass from both ST and NC black holes. We observe that the ratio of vector to scalar modes for $n = 0$ is 1.0001 for ST black holes and 1.0004 for NC black holes. In higher dimensions, the ratios deviate slightly from unity with vector modes becoming slightly more dominant. It has been shown analytically that ST black holes are isospectral for $n = 0$, thus the precision on our numerical calculation is 1×10^{-4}. Given this precision, we conclude that the isospectrality of NC black holes may be broken for $n = 0$.

In four dimensions for $n = 0$, our numerical analysis hints that in contrast to the ST case, isospectrality may be broken for NC black holes. Similar to the ST case, we find that isospectrality is broken for $n > 0$. Further analytical work is required to

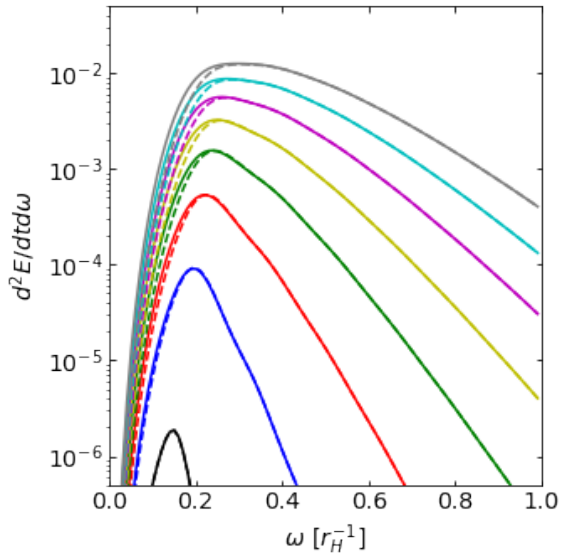

Figure 4.15: Energy spectra on the brane versus frequency ω for $s = 2$ scalar and vector modes. The solid lines are for vector modes and the dashed lines for scalar modes. The number of extra dimensions increases from 0 to 7 as the curves move from bottom to top. Black hole masses corresponding to the non-commutative black hole maximum temperature have been used. $M_D = \sqrt{\theta} = 1$ has been taken.

prove or disprove the isospectrality of NC black holes in four dimensions. A study of the isospectrality of quasi-normal modes for NC black holes may also be of interest.

Table 4.9: Power emission ratios on the brane of spin 2 vector to scalar modes for non-commutative (NC) and Schwarzschild Tangherlini (ST) black holes versus number of extra dimensions n at the mass of the non-commutative black hole of maximum temperature, M_{eM}.

	n							
	0	1	2	3	4	5	6	7
Ratio_{ST}	1.0001	1.010	1.028	1.038	1.042	1.043	1.043	1.042
Ratio_{NC}	1.0004	1.016	1.037	1.048	1.052	1.053	1.052	1.050

Chapter 5

Greybody Factors in the Bulk

In this section we present the calculations of transmission coefficients, absorption cross sections, and spectra for massless fields of spin 0, and spin 2 vector and tensor modes in the bulk. We note that there is no spin 2 tensor mode for $n = 0$. We leave out the results for scalar spin 2 modes due to the lack of a short-ranged potential for the NC case. We note however that Refs. [77, 78] found that the scalar spin 2 modes are the subdominant mode for higher values of n for the ST case. We have validated the method by comparing with the results for ST black holes [69, 77, 78] that we use for comparison with the NC results. We also compare our results for spin 0 emission from NC black holes with Ref. [11]. Throughout this section we consider black hole masses corresponding to the NC maximum temperature $M_{\mathrm{e}M}$ as shown in Table 2.2.

5.1 Transmission Coefficients

The fundamental calculated quantity is the transmission coefficient as a function of frequency for different black hole masses, number of extra dimensions, spin, and ℓ modes. Figure 5.1 shows transmission coefficients for $n = 7$ and $s = 0, 2$ as a function of frequency for different ℓ modes. The solid lines are for NC black holes and dashed lines for ST black holes. The quantum number ℓ increases from $\ell = s$ going from left to right. A black hole mass of $358M_D$ is used and corresponds to the NC black hole maximum temperature. The transmission coefficients in the bulk are

shifted significantly towards higher frequencies compared to those on the brane for the same ℓ mode. This is due to the increased height of the potential for bulk modes as compared to brane modes, which require higher frequencies to escape the potential barrier. Similar to results on the brane, we observe that the NC and ST black hole transmissions coefficients at this mass are very similar, differing slightly for higher ℓ.

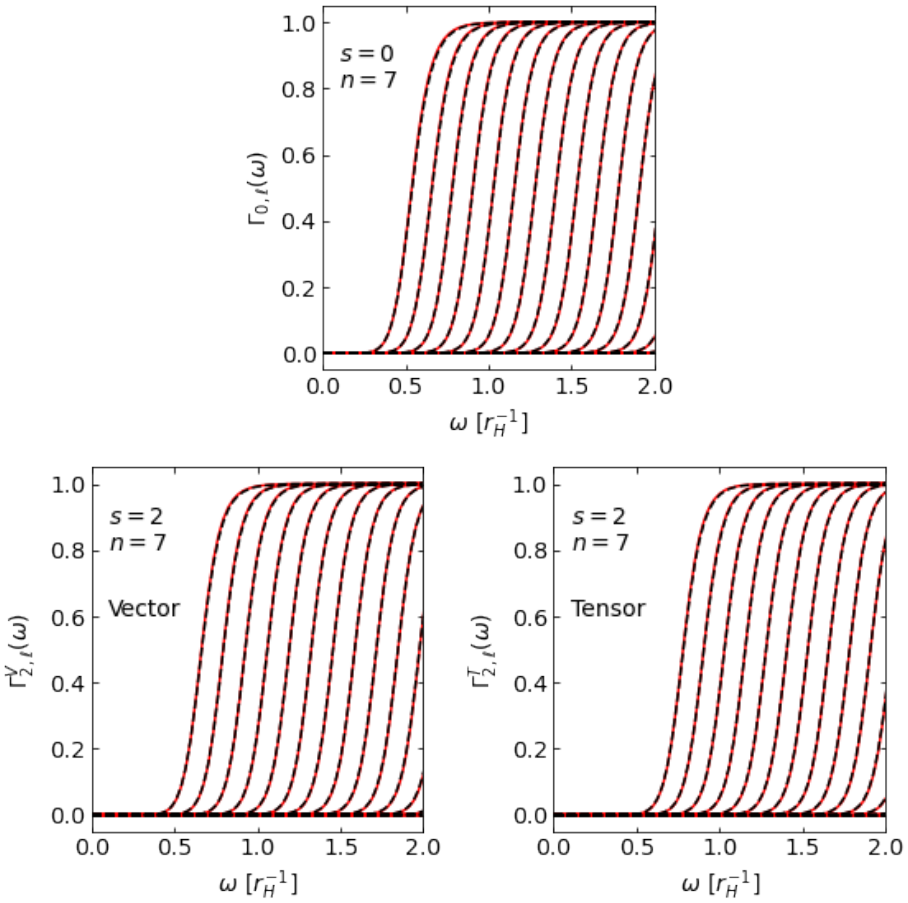

Figure 5.1: Transmission coefficients $\Gamma_{s,\ell}(\omega)$ in the bulk for $s = 0$ and $s = 2$ vector and tensor modes as a function of frequency ω. The quantum number ℓ increases from $\ell = s$ going from left to right. The red solid lines are for non-commutative black holes and black dashed lines for Schwarzschild-Tangherlini black holes. A black hole mass of $358M_D$ has been used corresponding to the non-commutative maximum temperature. $M_D = \sqrt{\theta} = 1$ has been taken.

5.2 Absorption Cross Sections

The absorption cross section in the bulk takes on a different form than the one on the brane as [77]

$$\sigma^{bulk}(\omega) = C(\omega) \sum_{\ell \geq s} N^P_{s,\ell} \Gamma_{s,\ell}(M;\omega), \tag{5.1}$$

where $C(\omega)$ is a normalization factor defined by

$$C(\omega) = \left(\frac{2\pi}{\omega}\right)^{\frac{n+2}{2}} \frac{1}{\Omega_{n+2}} = \frac{(4\pi)^{\frac{n+1}{2}} \Gamma\left(\frac{n+3}{2}\right)}{\omega^{n+2}}, \tag{5.2}$$

where we used the definition of the solid angle of the unit $(n+2)$-sphere

$$\Omega_{n+2} = \frac{2\pi^{\frac{n+3}{2}}}{\Gamma\left(\frac{n+3}{2}\right)}, \tag{5.3}$$

and Γ is the gamma function. We may explicitly write the bulk absorption cross section as

$$\sigma^{\text{bulk}}(\omega) = (4\pi)^{\frac{n+1}{2}} \Gamma\left(\frac{n+3}{2}\right) \frac{1}{\omega^{n+2}} \sum_{\ell \geq s} N^P_{s,\ell} \Gamma_{s,\ell}(\omega). \tag{5.4}$$

Most notably, there is now a dependence on $\omega^{-(n+2)}$ rather than ω^{-2}. In addition, we must normalize the spin 2 cross sections by a factor of $2/[(n+4)(n+1)]$ to account for the number of helicities in n extra dimensions [77].

Figure 5.2 shows cross sections versus frequency for $s = 0$ and the vector and tensor $s = 2$ modes. The solid lines are for NC black holes and dashed lines for ST black holes. Black hole masses corresponding to the NC black hole maximum temperature have been used, as shown in Table 2.2.

In contrast to the absorption cross sections on the brane, the absorption cross sections in the bulk increase with increasing number of extra dimensions. For ST black holes, the absorption cross section results are the same as Ref. [69]. The absorption cross section results for NC black holes and $s = 0$ agree qualitatively with Ref. [11], they are quantitatively different due to the use of different units. For spin 0, the low-frequency limit should correspond to the area of the higher dimensional black hole for both ST and NC black holes [11]

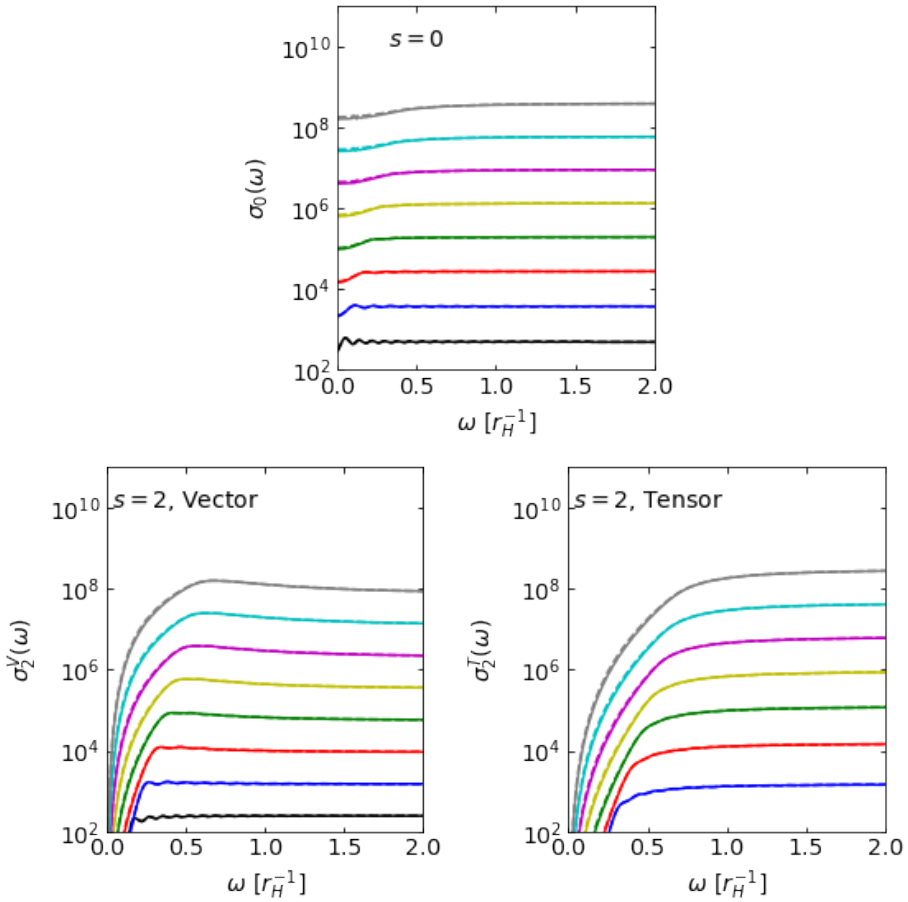

Figure 5.2: Absorption cross sections in the bulk versus frequency ω for $s = 0$ and the vector and tensor $s = 2$ modes. The solid lines are for non-commutative black holes and dashed lines for Schwarzschild-Tangherlini black holes. The number of extra dimensions increases from 0 to 7 as the curves moved from bottom to top at high ω. Black hole masses corresponding to the non-commutative black hole maximum temperature have been used. $M_D = \sqrt{\theta} = 1$ has been taken.

$$\sigma_0^{\rm bulk}(0) = \frac{2\pi^{\frac{n+3}{2}}}{\Gamma\left(\frac{n+3}{2}\right)} r_{\rm H}^{n+2}. \tag{5.5}$$

This is significantly larger in higher dimensions leading to larger absorption cross sections in the bulk as compared to the brane. Numerically, for $\omega = 0.001$, we obtain the black hole area to better than 1.7% for both ST and NC black holes for $0 \leq n \leq 4$ and to within 4.3% for $5 \leq n \leq 7$. The worse agreement for the $n \geq 5$ cases is likely due to round off errors arising from the machine precision since the cross section scales as $\omega^{-(n+2)}$. In the high frequency limit, it can be shown that the

absorption cross section approaches the projected area of an absorptive body with effective radius b_c [69]. The effective radius b_c is the same for both bulk and brane modes and is described in Section 4.3. Using the ST metric, the projected area in the bulk gives [69]

$$\sigma_{\infty}^{\text{bulk}} = \frac{\Omega_{n+1}}{n+2} b_c^{n+2} = \frac{2}{n+2} \frac{\pi^{\frac{n+2}{2}}}{\Gamma\left(\frac{n+2}{2}\right)} \left(\frac{n+3}{2}\right)^{\frac{n+2}{n+1}} \left(\frac{n+3}{n+1}\right)^{\frac{n+2}{2}} r_{\text{H,ST}}^{n+2}\,, \tag{5.6}$$

In the case of the NC metric, we have calculated $\sigma_{\infty}^{\text{bulk}}$ numerically. For $\omega = 3$, we obtain the expected high frequency behaviour of the spin 0 absorption cross section for ST and NC black holes to better than 1.2% for all number of dimensions. The spin 2 cross section requires the sum of scalar, vector and tensor modes to compare to the high frequency limit, however we are missing the scalar mode. However for high n where the scalar mode is the subdominant mode [77], we obtain the expected high frequency behaviour of the spin 2 absorption cross section by only accounting for the vector and tensor modes for ST and NC black holes to better than 5% for $n \geq 5$.

5.3 Particle Spectra

We compute the rate of particle emission per unit time and per unit frequency in the bulk as

$$\frac{d^2N}{dtd\omega} = \frac{1}{2\pi} \frac{1}{e^{\frac{\omega}{T_{\text{H}}}} - (-1)^{2s}} \sum_{\ell \geq s} N_{s,\ell}^{P} \Gamma_{s,\ell}(M;\omega). \tag{5.7}$$

We consider the case of equal mass which means the temperature of the ST black hole will be hotter, and hence lead to significantly more particle flux. Figure 5.3 shows particle spectra versus frequency for $s = 0$ and the vector and tensor $s = 2$ modes. The solid lines are for NC black holes and dashed lines for ST black holes. The number of extra dimensions increases from 0 to 7 as the curves move from bottom to top for the spin 2 cases. Black hole masses M_{eM} corresponding to the NC black hole maximum temperature have been used, as shown in Table 2.2.

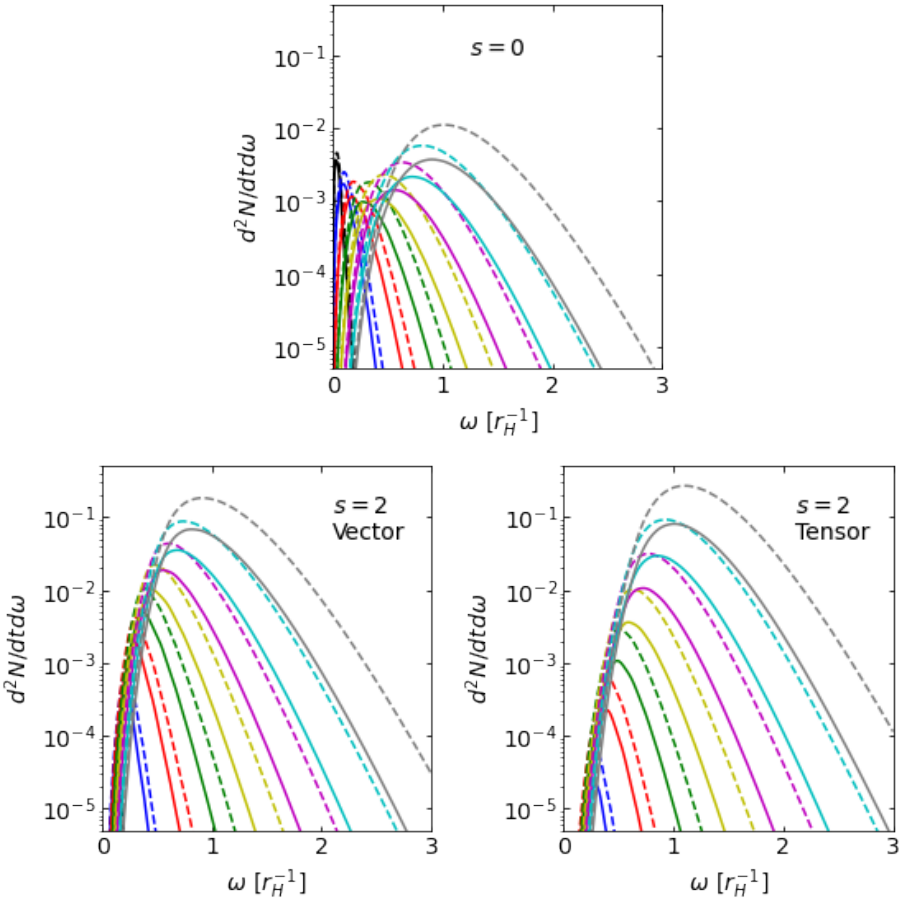

Figure 5.3: Particle spectra in the bulk versus frequency ω for $s = 0$ and the vector and tensor $s = 2$ modes. The solid lines are for non-commutative black holes and dashed lines for Schwarzschild-Tangherlini black holes. The number of extra dimensions increases from 0 to 7 as the curves move from bottom to top for the spin 2 cases. Black hole masses corresponding to the non-commutative black hole maximum temperature have been used. $M_D = \sqrt{\theta} = 1$ has been taken.

For the $s = 0$ case, an interesting phenomenon occurs for both the ST and NC case where the peak of the particle spectra decrease as n increases from 0 to 3, and then increases as n increases from 3 to 7. This is not seen in the results of Ref. [11], although a different definition of the higher dimensional Planck scale M_D is used.

5.4 Energy Spectra

As is the case for the brane, the energy spectra are similar to the particle spectra but include a multiplicative frequency factor

$$\frac{d^2E}{dtd\omega} = \frac{\omega}{2\pi}\frac{1}{e^{\frac{\omega}{T_{\rm H}}} - (-1)^{2s}}\sum_{\ell \geq s} N^P_{s,\ell}\Gamma_{s,\ell}(M;\omega). \tag{5.8}$$

Figure 5.4 shows particle spectra versus frequency for $s = 0$ and the vector and tensor $s = 2$ modes. The solid lines are for NC black holes and dashed lines for ST black holes. The number of extra dimensions increases from 0 to 7 as the curves move from bottom to top. Black hole masses $M_{{\rm e}M}$ corresponding to the NC black hole maximum temperature have been used, as shown in Table 2.2. For the spin 0 case, in contrast to the particle spectra the energy spectra increase with increasing n.

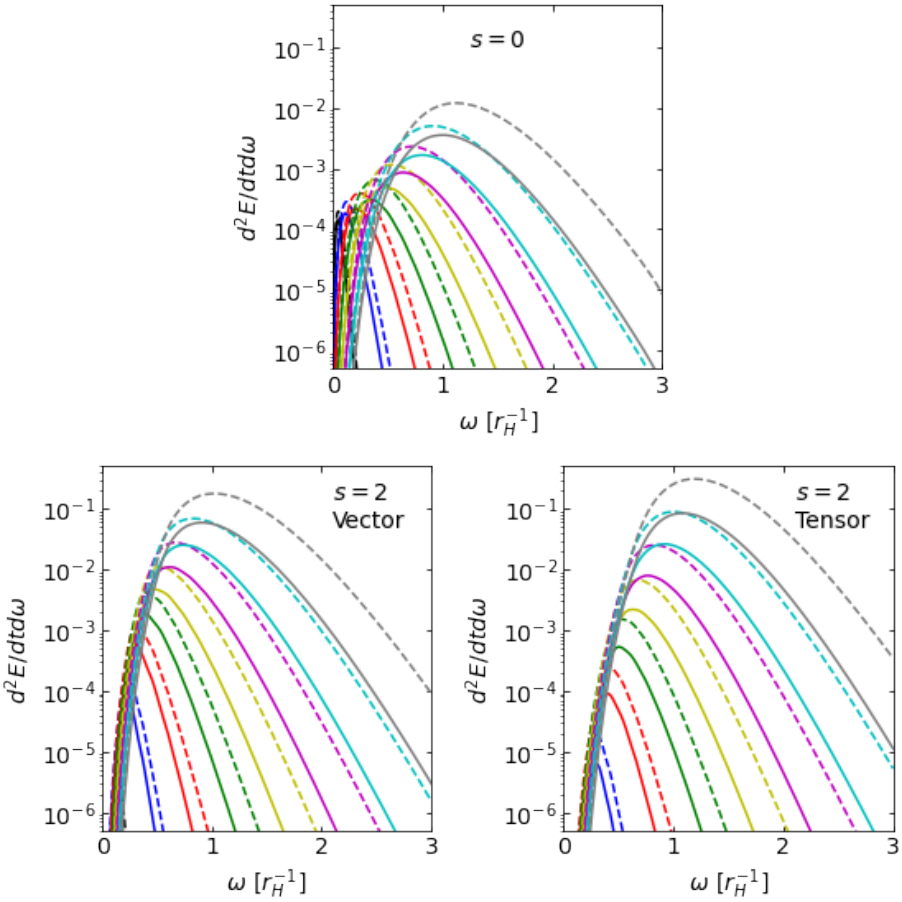

Figure 5.4: Energy spectra in the bulk versus frequency ω for $s = 0$ and the vector and tensor $s = 2$ modes. The solid lines are for non-commutative black holes and dashed lines for Schwarzschild-Tangherlini black holes. The number of extra dimensions increases from 0 to 7 as the curves move from bottom to top. Black hole masses corresponding to the non-commutative black hole maximum temperature have been used. $M_D = \sqrt{\theta} = 1$ has been taken.

5.5 Particle Flux and Total Power

To make the comparison quantitative, we integrate the particle spectra and energy spectra over frequency out to $\omega = 3$ to obtain the particle flux and power, respectively. Table 5.1 show the NC to ST particle flux ratios for the cases of equal mass at the NC maximum temperature. For all spins, the the NC particle flux is suppressed as compared to the ST particle flux and the suppression is enhanced for increasing number of extra dimensions.

Table 5.1: Ratio of particle flux from non-commutative to Schwarzschild-Tangherlini black holes in the bulk versus spin s and number of extra dimensions n at the mass of the non-commutative black hole of maximum temperature, $M_{\mathrm{e}M}$.

	n							
s	0	1	2	3	4	5	6	7
0	0.73	0.62	0.54	0.47	0.42	0.37	0.33	0.30
2 (vector)	0.40	0.43	0.42	0.41	0.39	0.37	0.34	0.31
2 (tensor)		0.34	0.33	0.33	0.31	0.30	0.28	0.26

Table 5.2 shows the NC to ST power ratios for the cases of equal mass. The same observations can be made as for the particle fluxes.

Table 5.2: Ratio of power emitted from non-commutative to Schwarzschild-Tangherlini black holes in the bulk versus spin s and number of extra dimensions n at the mass of the non-commutative black hole of maximum temperature, $M_{\mathrm{e}M}$.

	n							
s	0	1	2	3	4	5	6	7
0	0.67	0.56	0.48	0.42	0.37	0.33	0.29	0.26
2 (vector)	0.38	0.41	0.40	0.38	0.36	0.34	0.31	0.29
2 (tensor)		0.32	0.32	0.30	0.29	0.27	0.26	0.24

Concentrating on NC geometry inspired black holes, we calculate the particle flux and total power for each number of extra dimensions and compare it to the $n = 0$ case shown in Table 5.3 and Table 5.4, respectively. For the spin 2 case there is no $n = 0$ tensor mode so we can compare it to the $n = 0$ vector mode. Direct comparison with

Ref. [69] of the results for ST black holes in the spin 0 case (not shown) is not possible since the black hole mass used is not stated. The results are however, similar.

Table 5.3: Particle flux ratios in the bulk for different number of extra dimensions n relative to $n = 0$ versus spin s for non-commutative black holes with the maximum temperature. The spin 2 tensor modes are compared to the $n = 0$ vector mode.

	n							
s	0	1	2	3	4	5	6	7
0	1	1.08	1.22	1.56	2.27	3.72	6.82	13.83
2 (vector)	1	54	364	1288	3525	8662	20569	49199
2 (tensor)		3.41	52	332	1472	5461	18555	60759

Table 5.4: Power emission ratios in the bulk for different number of extra dimensions n relative to $n = 0$ versus spin s for non-commutative black holes with the maximum temperature. The spin 2 tensor modes are compared to the $n = 0$ vector mode.

	n							
s	0	1	2	3	4	5	6	7
0	1	3.00	6.25	12	26	56	129	323
2 (vector)	1	88	834	3885	13475	40952	118183	339146
2 (tensor)		7.11	153	1268	7010	31548	127641	491101

Shown in Table 5.5 and Table 5.6 are the case of particle flux and power for the vector and tensor spin 2 modes compared to the spin 0 case. Direct comparison with Ref. [78] of the results for ST black holes (not shown) is not possible since the black hole mass used is not stated. The results are however, similar.

Shown in Table 5.7 and Table 5.8 are the case of particle flux and power for tensor spin 2 modes relative to vector spin 2 modes. For a small number of extra dimensions the vector modes dominate. As n increases the tensor modes become comparable to the vector modes and dominate for the $n = 7$ case.

Table 5.5: Particle flux ratios in the bulk for vector and tensor spin 2 modes relative to $s = 0$ mode versus number of extra dimensions n for non-commutative black holes with the maximum temperature.

n	$s = 0$	$s = 2$ (vector)	$s = 2$ (tensor)
0	1	0.005	
1	1	0.23	0.01
2	1	1.36	0.19
3	1	3.77	0.97
4	1	7.10	2.96
5	1	10.63	6.70
6	1	13.77	12.42
7	1	16.25	20.06

Table 5.6: Power emission ratios in the bulk for vector and tensor spin 2 modes relative to $s = 0$ mode versus number of extra dimensions n for non-commutative black holes with the maximum temperature.

n	$s = 0$	$s = 2$ (vector)	$s = 2$ (tensor)
0	1	0.01	
1	1	0.43	0.03
2	1	1.96	0.36
3	1	4.59	1.50
4	1	7.75	4.03
5	1	10.82	8.34
6	1	13.42	14.50
7	1	15.44	22.35

Table 5.7: Particle flux ratios in the bulk for different number of extra dimensions n of tensor spin 2 modes relative to vector spin 2 modes for non-commutative black holes with the maximum temperature.

				n			
s	1	2	3	4	5	6	7
Ratio (T/V)	0.06	0.14	0.26	0.42	0.63	0.90	1.23

Table 5.8: Power emission ratios in the bulk for different number of extra dimensions n of tensor spin 2 modes relative to vector spin 2 modes for non-commutative black holes with the maximum temperature.

				n			
s	1	2	3	4	5	6	7
Ratio (T/V)	0.08	0.18	0.33	0.52	0.77	1.08	1.45

5.6 Bulk-to-brane Emission Ratios

It is of interest to compare the relative emission of fields in the bulk to those on the brane. Energy emitted into the bulk would be interpreted as missing energy by an observer on the brane. Therefore in Figure 5.5 we plot the ratios of particle flux and energy emission, respectively of bulk to brane modes for spin 0 and spin 2 fields from a NC black hole at the maximum temperature. For the spin 2 case we consider the ratios of vector spin 2 modes in the bulk to vector spin 2 modes on the brane, and tensor spin 2 modes in the bulk to vector spin 2 modes on the brane. The number of extra dimensions increases from top to bottom at low frequencies.

The plots for the scalar case agree qualitatively with Ref. [11, 69], despite the difference in definition of the higher dimensional Planck scale M_D. In the low frequency regime, the bulk modes are suppressed compared to the modes on the brane. This is due to the brane modes turning on at lower frequencies as compared to the bulk leading to higher emission rates of brane modes for lower frequencies. The suppression at low frequencies is larger for increasing number of dimensions. In the high frequency regime, the bulk modes dominate in all cases with the relative emission increasing with each number of extra dimension. For high frequencies, Figures 4.10 and 5.4 show that the emission is significantly suppressed on the brane for $\omega > 1$ and in the bulk for $\omega > 3$. Thus even though the bulk modes dominate for higher frequencies, the overall emission at these frequencies is suppressed for both spectra. To make the comparison quantitative, we integrate the emission spectra over frequency out to $\omega = 3$ to obtain the total ratio of bulk to brane emission for each number of extra dimensions n. Table 5.9 shows relative bulk to brane emission ratios for spin 0 and 2 fields from a NC black hole at the maximum temperature.

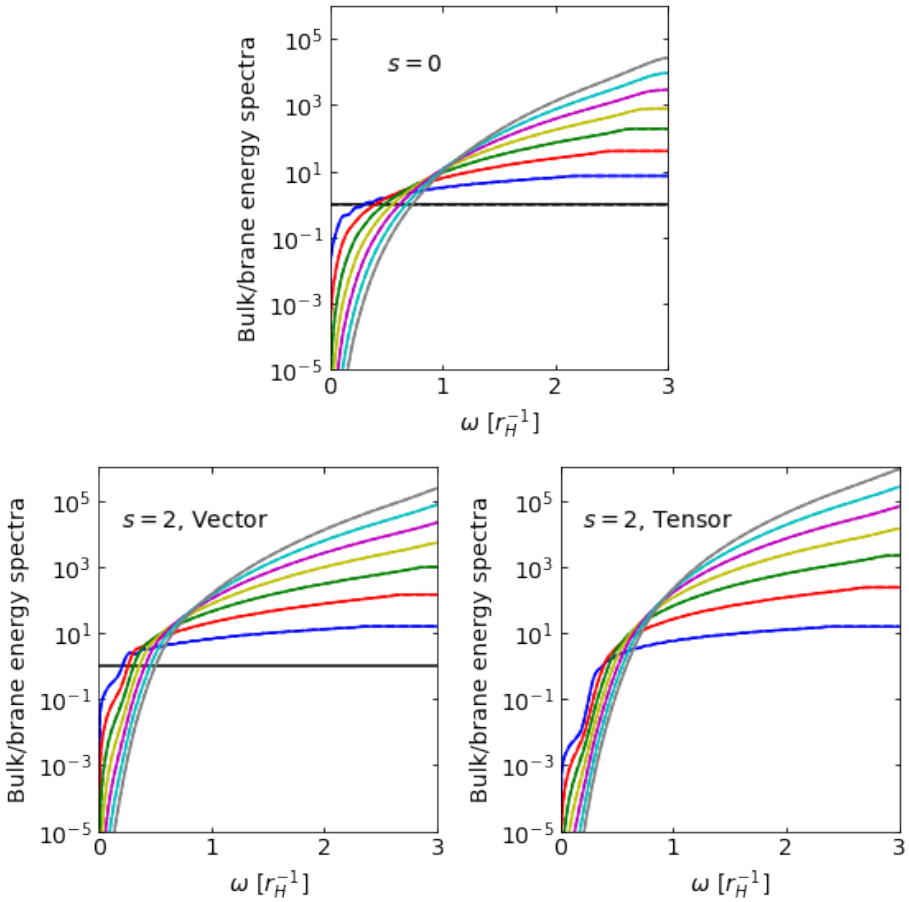

Figure 5.5: Ratios of bulk to brane emission versus frequency ω for different number of extra dimension n and for spin 0 and vector and tensor spin 2 modes. The number of extra dimensions increases from 0 to 7 as the curves move from top to bottom at low frequencies. There is no tensor mode for $n = 0$. Black hole masses corresponding to the non-commutative black hole maximum temperature have been used. $M_D = \sqrt{\theta} = 1$ has been taken.

Table 5.9: Ratios of bulk to brane power emission for different number of extra dimension n and for spin 0 and vector and tensor spin 2 modes. We compare the spin 2 tensor mode in the bulk to the spin 2 vector mode on the brane. Black hole masses corresponding to the non-commutative black hole maximum temperature have been used. $M_D = \sqrt{\theta} = 1$ has been taken.

	n							
s	0	1	2	3	4	5	6	7
0	1	0.35	0.19	0.15	0.14	0.18	0.24	0.40
2 (vector)	1	1.08	1.25	1.54	2.07	3.03	4.82	8.42
2 (tensor)		0.09	0.23	0.50	1.08	2.33	5.21	12.19

5.7 Relative Emissivities

It has long been argued that black holes will radiate mainly on the brane [75]. This claim is largely due to the fact that only the graviton is emitted in the bulk (ignoring the emission of a possible massless scalar field in the bulk), while all of the Standard model fields may be emitted on the brane. This claim has been supported for the ST case in Refs. [77], however it was noted that graviton emission is significant in the presence of extra dimensions. Here we will investigate the emission probabilities into the various channels for Standard Model fields plus the graviton for the NC case.

We consider the minimal $U(1) \times SU(2) \times SU(3)$ standard model with three families and one Higgs field. For temperatures above the spontaneous symmetry breaking scale $\sim$ 100 GeV, all Standard Model fields may be treated as massless fields [6, 77]. In Figure 2.3, we observe that NC black holes are generally below 100 GeV. The highest temperature is $\sim$ 98 GeV for the $n = 7$ case at the maximum temperature. Therefore we note that the following analysis may overestimate the available degrees of freedom on the brane using our choice of parameters of $M_D = \sqrt{\theta} = 1$. However we add that it has been shown that the main effect of mass on the emission spectra is to add a cut into the frequency range below which the emission spectra is significantly damped [79]. Higher temperatures may be achieved by choosing $\sqrt{\theta} < 1$. The number of degrees of freedom (dof) for each field is [15]

$$\text{dof} = n_Q \times n_S \times n_F \times n_C, \tag{5.9}$$

where n_Q is the number of charge states, n_S is the number of spin polarizations, n_F is the number of flavours, and n_C is the number of colours. For spin 0 fields on the brane there are 4 degrees of freedom arising from the complex Higgs doublet [77]. For spin 1/2 fields on the brane there are 90 degrees of freedom arising from quarks, charged leptons and neutrinos. For spin 1 fields on the brane there are 24 degrees of freedom from massless gauge bosons. For the bulk graviton the number of degrees of freedom (helicities) depends on the number of dimensions and is equal to $(n+4)(n+1)/2$ [77].

The probabilities of emission for different spin fields are [15]

$$P_i = \frac{\epsilon_i \times \text{dof}_i}{\sum_j \epsilon_j \times \text{dof}_j}, \tag{5.10}$$

where ϵ_i and dof_i are the particle fluxes and degrees of freedom of field i. Table 5.10 shows the probabilities of emission for the different spin fields from a NC black hole at the maximum temperature. We also plot the probabilities of emission for the different spin fields from a NC black hole at the maximum temperature against the number of extra dimensions in Figure 5.6. For spin 2 modes in the bulk we only account for the vector and tensor modes. We find that for both the ST (not shown) and the NC case, the spin 2 emission into the bulk is the dominant channel for $n \geq 5$. These results disagree with those from Ref. [77], however agree with Ref. [80]. A detailed study which includes the effect of spin 2 scalar modes from NC black holes is required before a conclusive statement can be made.

Table 5.10: Probability of emission for different spin fields from a non-commutative black hole at the maximum temperature. $M_D = \sqrt{\theta} = 1$ has been taken.

	n							
s	0	1	2	3	4	5	6	7
0	0.08	0.04	0.04	0.03	0.03	0.02	0.01	0.01
1/2	0.84	0.80	0.74	0.67	0.55	0.39	0.22	0.10
1	0.08	0.15	0.18	0.19	0.17	0.13	0.07	0.03
2 (brane)	0.00	0.01	0.01	0.01	0.01	0.01	0.00	0.00
2 (bulk)	0.00	0.00	0.03	0.10	0.24	0.45	0.70	0.86

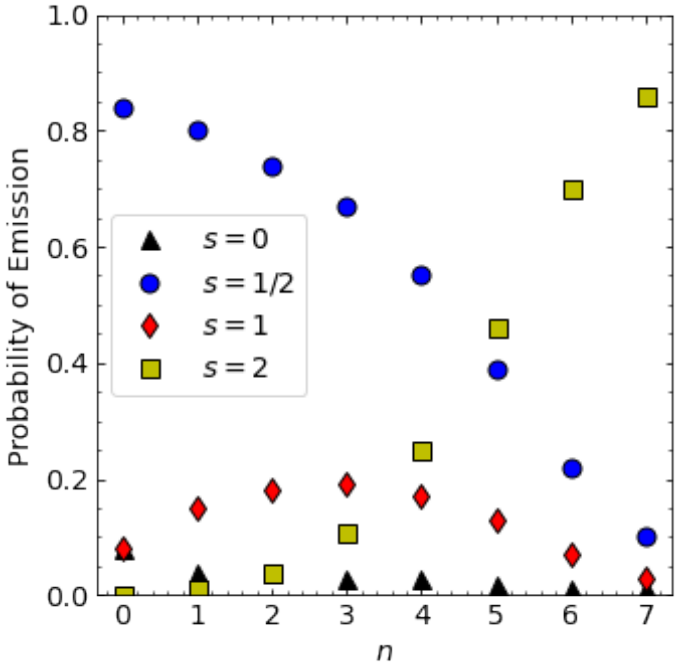

Figure 5.6: Probability of emission for different spin fields from a non-commutative black hole at the maximum temperature against the number of extra dimensions n. $M_D = \sqrt{\theta} = 1$ has been taken.

Chapter 6

Conclusion

In this thesis we have investigated the effect of non-commutativity on Hawking evaporation from higher dimensional spherically symmetric and static black holes both on the brane and in the bulk. We have presented greybody factors, absorption cross sections, and particle and energy spectra for massless fields of spin 0, 1/2, 1, and 2 from higher dimensional NC geometry inspired black holes. The calculations are numerical and thus valid over the entire frequency range.

The NC black hole transmission coefficients are similar to the ST black hole transmission coefficients when their horizon radius are similar. However, there are major differences when the black hole masses are similar but the horizon radius are significantly different. The major difference in transmission coefficients is that the NC black hole transmission coefficients turn-on at slightly higher frequency.

We observe significant differences in NC black hole and ST black hole absorption cross sections occur at low frequencies while the cross sections at high frequencies approach the geometrical optics limits. For masses near the minimum NC black hole mass, the differences are more apparent, particularly for higher dimensions. For equal masses, the NC black hole spectra are significantly lower than for ST black holes, mainly due to the lower temperature. However, at equal temperature the NC black hole spectra are still significantly lower than for ST black hole spectra.

For $n = 0$, we find that NC black holes are not isospectral which is in contrast to

the ST case. For NC black holes, we observe that isospectrality is broken in higher dimensions, similar to the ST case. The bulk to brane emission ratios are similar to those for the ST case, and spin 2 emission in the bulk becomes the dominant channel for high n.

The emission of higher spin fields is useful for relating possible experimental observation of black hole radiation to theory. The reduction in emission due to the greybody factors, not temperature, that we observe are hopefully independent of our choice of parameters. The results presented here may be useful in Monte Carlo simulations for searches of microscopic NC black holes at the Large Hadron Collider and future colliders. Future work should investigate the greybody factors for the spin 2 scalar modes in the bulk for NC black holes. It would also be interesting to study the effect of rotation on the greybody factors for NC black holes, particularly the effect of super-radiance. This work represents another step towards possibly elucidating some aspects of quantum gravity.

Bibliography

[1] Z. Cox and D. M. Gingrich. "Greybody factors for higher-dimensional non-commutative geometry inspired black holes". In: *Class. Quant. Grav.* 40.17 (2023), p. 175013. DOI: 10.1088/1361-6382/aceb46. arXiv: 2303.08309 [gr-qc].

[2] C. Montgomery, W. Orchiston, and I. Whittingham. "Michell, Laplace and the origin of the black hole concept". In: *Journal of Astronomical History and Heritage* 12 (2009), pp. 90–96. DOI: 10.3724/SP.J.1440-2807.2009.02.01".

[3] K. Schwarzschild. "On the gravitational field of a mass point according to Einstein's theory". In: *Sitzungsber. Preuss. Akad. Wiss. Berlin (Math. Phys.)* 1916 (1916), pp. 189–196. arXiv: physics/9905030.

[4] C. W. Misner, K. S. Thorne, and J. A. Wheeler. *Gravitation*. San Francisco: W. H. Freeman, 1973. ISBN: 978-0-7167-0344-0.

[5] S. W. Hawking. "Particle Creation by Black Holes". In: *Commun. Math. Phys.* 43 (1975). Ed. by G. W. Gibbons and S. W. Hawking. [Erratum: Commun.Math.Phys. 46, 206 (1976)], pp. 199–220. DOI: 10.1007/BF02345020.

[6] S. B. Giddings and S. D. Thomas. "High-energy colliders as black hole factories: The End of short distance physics". In: *Phys. Rev. D* 65 (2002), p. 056010. DOI: 10.1103/PhysRevD.65.056010. arXiv: hep-ph/0106219.

[7] C. M. Harris. "Physics beyond the standard model: Exotic leptons and black holes at future colliders". PhD thesis. Christ's College, Dec. 2004. arXiv: hep-ph/0502005.

[8] N. Arkani-Hamed, S. Dimopoulos, and G. R. Dvali. "The Hierarchy problem and new dimensions at a millimeter". In: *Phys. Lett. B* 429 (1998), pp. 263–272. DOI: 10.1016/S0370-2693(98)00466-3. arXiv: hep-ph/9803315.

[9] *Particle Data Group*. "Review of Particle Physics". In: *PTEP* 2022 (2022), p. 083C01. DOI: 10.1093/ptep/ptac097.

[10] D. M. Gingrich. "Black hole cross-section at the Large Hadron Collider". In: *Int. J. Mod. Phys. A* 21 (2006), pp. 6653–6676. DOI: 10.1142/S0217751X06035087. arXiv: hep-ph/0609055.

[11] P. Nicolini and E. Winstanley. "Hawking emission from quantum gravity black holes". In: *JHEP* 11 (2011), p. 075. DOI: 10.1007/JHEP11(2011)075. arXiv: 1108.4419 [hep-ph].

[12] T. G. Rizzo. "Noncommutative Inspired Black Holes in Extra Dimensions". In: *JHEP* 09 (2006), p. 021. DOI: 10.1088/1126-6708/2006/09/021. arXiv: hep-ph/0606051.

[13] V. P. Frolov and D. Stojkovic. "Black hole radiation in the brane world and recoil effect". In: *Phys. Rev. D* 66 (2002), p. 084002. DOI: 10.1103/PhysRevD.66.084002. arXiv: hep-th/0206046.

[14] D. M. Gingrich. "Black Hole Production at the Large Hadron Collider". In: *Int. J. Mod. Phys. A* 22 (2007). Ed. by S. Khalil, pp. 5685–5699. DOI: 10.1142/S0217751X0703892X. arXiv: 0706.0627 [hep-ph].

[15] D. M. Gingrich. "Missing energy in black hole production and decay at the Large Hadron Collider". In: *JHEP* 11 (2007), p. 064. DOI: 10.1088/1126-6708/2007/11/064. arXiv: 0706.0623 [hep-ph].

[16] P. Kanti and E. Winstanley. "Hawking Radiation from Higher-dimensional Black Holes". In: *Fundam. Theor. Phys.* 178 (2015), pp. 229–265. DOI: 10.1007/978-3-319-10852-0_8. arXiv: 1402.3952 [hep-th].

[17] S. W. Hawking. "Black hole explosions". In: *Nature* 248 (1974), pp. 30–31. DOI: 10.1038/248030a0.

[18] M. K. Parikh and F. Wilczek. "Hawking radiation as tunneling". In: *Phys. Rev. Lett.* 85 (2000), pp. 5042–5045. DOI: 10.1103/PhysRevLett.85.5042. arXiv: hep-th/9907001.

[19] J. Auffinger. "Primordial black holes as dark matter and Hawking radiation constraints with BlackHawk". PhD thesis. Université de Lyon, 2022.

[20] A. Arbey, J. Auffinger, and J. Silk. "Evolution of primordial black hole spin due to Hawking radiation". In: *Mon. Not. Roy. Astron. Soc.* 494.1 (2020), pp. 1257–1262. DOI: 10.1093/mnras/staa765. arXiv: 1906.04196 [astro-ph.CO].

[21] D. V. Ahluwalia. "Quantum measurements, gravitation, and locality". In: *Phys. Lett. B* 339 (1994), pp. 301–303. DOI: 10.1016/0370-2693(94)90622-X. arXiv: gr-qc/9308007.

[22] P. Nicolini. "Noncommutative Black Holes, The Final Appeal To Quantum Gravity: A Review". In: *Int. J. Mod. Phys. A* 24 (2009), pp. 1229–1308. DOI: 10.1142/S0217751X09043353. arXiv: 0807.1939 [hep-th].

[23] H. S. Snyder. "Quantized space-time". In: *Phys. Rev.* 71 (1947), pp. 38–41. DOI: 10.1103/PhysRev.71.38.

[24] A. Connes. *Noncommutative geometry*. 1994. ISBN: 978-0-12-185860-5.

[25] N. Seiberg and E. Witten. "String theory and noncommutative geometry". In: *JHEP* 09 (1999), p. 032. DOI: 10.1088/1126-6708/1999/09/032. arXiv: hep-th/9908142.

[26] C.-S. Chu and P.-M. Ho. "Noncommutative open string and D-brane". In: *Nucl. Phys. B* 550 (1999), pp. 151–168. DOI: 10.1016/S0550-3213(99)00199-6. arXiv: hep-th/9812219.

[27] D. M. Gingrich. "Noncommutative geometry inspired black holes in higher dimensions at the LHC". In: *JHEP* 05 (2010), p. 022. DOI: 10.1007/JHEP05(2010)022. arXiv: 1003.1798 [hep-ph].

[28] P. Tadros. "(1+1)-Dimensional Scalar Field Theory on q-Deformed Space". In: *LHEP* 2023 (2023), p. 392. DOI: 10.31526/lhep.2023.392. arXiv: 2301.03106 [hep-th].

[29] M. Chaichian, P. Presnajder, and A. Tureanu. "New concept of relativistic invariance in NC space-time: Twisted Poincare symmetry and its implications". In: *Phys. Rev. Lett.* 94 (2005), p. 151602. DOI: 10.1103/PhysRevLett.94.151602. arXiv: hep-th/0409096.

[30] A. Smailagic and E. Spallucci. "Feynman path integral on the noncommutative plane". In: *J. Phys. A* 36 (2003), p. L467. DOI: 10.1088/0305-4470/36/33/101. arXiv: hep-th/0307217.

[31] A. Smailagic and E. Spallucci. "Lorentz invariance, unitarity in UV-finite of QFT on noncommutative spacetime". In: *J. Phys. A* 37 (2004), p. 7169. DOI: 10.1088/0305-4470/37/28/008. arXiv: hep-th/0406174.

[32] V. P. Nair and A. P. Polychronakos. "Quantum mechanics on the noncommutative plane and sphere". In: *Phys. Lett. B* 505 (2001), pp. 267–274. DOI: 10.1016/S0370-2693(01)00339-2. arXiv: hep-th/0011172.

[33] A. Smailagic and E. Spallucci. "Noncommutative 3-D harmonic oscillator". In: *J. Phys. A* 35 (2002), pp. L363–L368. DOI: 10.1088/0305-4470/35/26/103. arXiv: hep-th/0205242.

[34] P. Nicolini, A. Smailagic, and E. Spallucci. "Noncommutative geometry inspired Schwarzschild black hole". In: *Phys. Lett. B* 632 (2006), pp. 547–551. DOI: 10.1016/j.physletb.2005.11.004. arXiv: gr-qc/0510112.

[35] S. Ansoldi, P. Nicolini, A. Smailagic, and E. Spallucci. "Noncommutative geometry inspired charged black holes". In: *Phys. Lett. B* 645 (2007), pp. 261–266. DOI: 10.1016/j.physletb.2006.12.020. arXiv: gr-qc/0612035.

[36] L. Modesto and P. Nicolini. "Charged rotating noncommutative black holes". In: *Physical Review D* 82.10 (2010), p. 104035.

[37] R. Banerjee, B. R. Majhi, and S. Samanta. "Noncommutative Black Hole Thermodynamics". In: *Phys. Rev. D* 77 (2008), p. 124035. DOI: 10.1103/PhysRevD.77.124035. arXiv: 0801.3583 [hep-th].

[38] K. Nozari and S. H. Mehdipour. "Hawking Radiation as Quantum Tunneling from Noncommutative Schwarzschild Black Hole". In: *Class. Quant. Grav.* 25 (2008), p. 175015. DOI: 10.1088/0264-9381/25/17/175015. arXiv: 0801.4074 [gr-qc].

[39] R. Banerjee, S. Gangopadhyay, and S. K. Modak. "Voros product, Noncommutative Schwarzschild Black Hole and Corrected Area Law". In: *Phys. Lett. B* 686 (2010), pp. 181–187. DOI: 10.1016/j.physletb.2010.02.034. arXiv: 0911.2123 [hep-th].

[40] P. R. Giri. "Asymptotic quasinormal modes of a noncommutative geometry inspired Schwarzschild black hole". In: *Int. J. Mod. Phys. A* 22 (2007), pp. 2047–2056. DOI: 10.1142/S0217751X07036245. arXiv: hep-th/0604188.

[41] D. Batic, N. G. Kelkar, M. Nowakowski, and K. Redway. "Perturbing microscopic black holes inspired by noncommutativity". In: *Eur. Phys. J. C* 79.7 (2019), p. 581. DOI: 10.1140/epjc/s10052-019-7084-x. arXiv: 1907.06463 [gr-qc].

[42] Y.-G. Miao, Z. Xue, and S.-J. Zhang. "Tunneling of massive particles from noncommutative inspired Schwarzschild black hole". In: *Gen. Rel. Grav.* 44 (2012), pp. 555–566. DOI: 10.1007/s10714-011-1290-7. arXiv: 1012.2426 [hep-th].

[43] K. Emelideme. "Study of Microscopic Black Holes at the LHC Using Noncommutative Inspired Geometry". MA thesis. University of Alberta, 2013.

[44] M.-I. Park. "Smeared hair and black holes in three-dimensional de Sitter spacetime". In: *Phys. Rev. D* 80 (2009), p. 084026. DOI: 10.1103/PhysRevD.80.084026. arXiv: 0811.2685 [hep-th].

[45] F. R. Tangherlini. "Schwarzschild field in n dimensions and the dimensionality of space problem". In: *Nuovo Cim.* 27 (1963), pp. 636–651. DOI: 10.1007/BF02784569.

[46] D. Batic and P. Nicolini. "Fuzziness at the horizon". In: *Phys. Lett. B* 692 (2010), pp. 32–35. DOI: 10.1016/j.physletb.2010.07.007. arXiv: 1001.1158 [gr-qc].

[47] E. Brown and R. B. Mann. "Instability of the Noncommutative Geometry Inspired Black Hole". In: *Phys. Lett. B* 694 (2011), pp. 440–445. DOI: 10.1016/j.physletb.2010.10.014. arXiv: 1012.4787 [hep-th].

[48] H. A. Borges, I. P. R. Baranov, F. C. Sobrinho, and S. Carneiro. "Remnant loop quantum black holes". In: *Class. Quant. Grav.* 41.5 (2024), 05LT01. DOI: 10.1088/1361-6382/ad210c. arXiv: 2310.01560 [gr-qc].

[49] V. Husain and R. B. Mann. "Thermodynamics and phases in quantum gravity". In: *Class. Quant. Grav.* 26 (2009), p. 075010. DOI: 10.1088/0264-9381/26/7/075010. arXiv: 0812.0399 [gr-qc].

[50] T. Regge and J. A. Wheeler. "Stability of a Schwarzschild singularity". In: *Phys. Rev.* 108 (1957), pp. 1063–1069. DOI: 10.1103/PhysRev.108.1063.

[51] F. J. Zerilli. "Effective potential for even parity Regge-Wheeler gravitational perturbation equations". In: *Phys. Rev. Lett.* 24 (1970), pp. 737–738. DOI: 10.1103/PhysRevLett.24.737.

[52] J. M. Bardeen and W. H. Press. "Radiation fields in the schwarzschild background". In: *J. Math. Phys.* 14 (1973), pp. 7–19. DOI: 10.1063/1.1666175.

[53] S. A. Teukolsky. "Perturbations of a rotating black hole. 1. Fundamental equations for gravitational electromagnetic and neutrino field perturbations". In: *Astrophys. J.* 185 (1973), pp. 635–647. DOI: 10.1086/152444.

[54] W. H. Press and S. A. Teukolsky. "Perturbations of a Rotating Black Hole. II. Dynamical Stability of the Kerr Metric". In: *Astrophys. J.* 185 (1973), pp. 649–674. DOI: 10.1086/152445.

[55] S. A. Teukolsky and W. H. Press. "Perturbations of a rotating black hole. III - Interaction of the hole with gravitational and electromagnet ic radiation". In: *Astrophys. J.* 193 (1974), pp. 443–461. DOI: 10.1086/153180.

[56] C. M. Harris and P. Kanti. "Hawking radiation from a (4+n)-dimensional rotating black hole". In: *Phys. Lett. B* 633 (2006), pp. 106–110. DOI: 10.1016/j.physletb.2005.10.025. arXiv: hep-th/0503010.

[57] R. A. Konoplya. "Gravitational quasinormal radiation of higher dimensional black holes". In: *Phys. Rev. D* 68 (2003), p. 124017. DOI: 10.1103/PhysRevD.68.124017. arXiv: hep-th/0309030.

[58] E. Berti, V. Cardoso, and A. O. Starinets. "Quasinormal modes of black holes and black branes". In: *Class. Quant. Grav.* 26 (2009), p. 163001. DOI: 10.1088/0264-9381/26/16/163001. arXiv: 0905.2975 [gr-qc].

[59] S. Chandrasekhar and S. L. Detweiler. "The quasi-normal modes of the Schwarzschild black hole". In: *Proc. Roy. Soc. Lond. A* 344 (1975), pp. 441–452. DOI: 10.1098/rspa.1975.0112.

[60] D. del-Corral and J. Olmedo. "Breaking of isospectrality of quasinormal modes in nonrotating loop quantum gravity black holes". In: *Phys. Rev. D* 105.6 (2022), p. 064053. DOI: 10.1103/PhysRevD.105.064053. arXiv: 2201.09584 [gr-qc].

[61] H. Kodama and A. Ishibashi. "A Master equation for gravitational perturbations of maximally symmetric black holes in higher dimensions". In: *Prog. Theor. Phys.* 110 (2003), pp. 701–722. DOI: 10.1143/PTP.110.701. arXiv: hep-th/0305147.

[62] S. Hossenfelder, L. Modesto, and I. Premont-Schwarz. "Emission spectra of self-dual black holes" (Feb. 2012). arXiv: 1202.0412 [gr-qc].

[63] A. Arbey, J. Auffinger, M. Geiller, E. R. Livine, and F. Sartini. "Hawking radiation by spherically-symmetric static black holes for all spins: Teukolsky equations and potentials". In: *Phys. Rev. D* 103.10 (2021), p. 104010. DOI: 10.1103/PhysRevD.103.104010. arXiv: 2101.02951 [gr-qc].

[64] D. Gingrich. unpublished. 2024.

[65] S. A. Hughes. "Computing radiation from Kerr black holes: Generalization of the Sasaki-Nakamura equation". In: *Phys. Rev. D* 62 (2000). [Erratum: Phys.Rev.D 67, 089902 (2003)], p. 044029. DOI: 10.1103/PhysRevD.62.044029. arXiv: gr-qc/0002043.

[66] S. Chandrasekhar. *The mathematical theory of black holes*. 1985.

[67] D. K. Park. "Hawking radiation of the brane-localized graviton from a (4+n)-dimensional black hole". In: *Class. Quant. Grav.* 23 (2006), pp. 4101–4110. DOI: 10.1088/0264-9381/23/12/007. arXiv: hep-th/0512021.

[68] J. N. Goldberg, A. J. MacFarlane, E. T. Newman, F. Rohrlich, and E. C. G. Sudarshan. "Spin s spherical harmonics and edth". In: *J. Math. Phys.* 8 (1967), p. 2155. DOI: 10.1063/1.1705135.

[69] C. M. Harris and P. Kanti. "Hawking radiation from a (4+n)-dimensional black hole: Exact results for the Schwarzschild phase". In: *JHEP* 10 (2003), p. 014. DOI: 10.1088/1126-6708/2003/10/014. arXiv: hep-ph/0309054.

[70] F. Gray and M. Visser. "Greybody Factors for Schwarzschild Black Holes: Path-Ordered Exponentials and Product Integrals". In: *Universe* 4.9 (2018), p. 93. DOI: 10.3390/universe4090093. arXiv: 1512.05018 [gr-qc].

[71] F. Gray. "Black Hole Radiation, Geybody Factors, and Generalised Wick Rotation". MA thesis. Victoria University of Wellington, 2016.

[72] F. Moulin, A. Barrau, and K. Martineau. "An overview of quasinormal modes in modified and extended gravity". In: *Universe* 5.9 (2019), p. 202. DOI: 10.3390/universe5090202. arXiv: 1908.06311 [gr-qc].

[73] P. Kanti and J. March-Russell. "Calculable corrections to brane black hole decay. 2. Greybody factors for spin 1/2 and 1". In: *Phys. Rev. D* 67 (2003), p. 104019. DOI: 10.1103/PhysRevD.67.104019. arXiv: hep-ph/0212199.

[74] Y. Decanini, G. Esposito-Farese, and A. Folacci. "Universality of high-energy absorption cross sections for black holes". In: *Phys. Rev. D* 83 (2011), p. 044032. DOI: 10.1103/PhysRevD.83.044032. arXiv: 1101.0781 [gr-qc].

[75] R. Emparan, G. T. Horowitz, and R. C. Myers. "Black holes radiate mainly on the brane". In: *Phys. Rev. Lett.* 85 (2000), pp. 499–502. DOI: 10.1103/PhysRevLett.85.499. arXiv: hep-th/0003118.

[76] F. Moulin and A. Barrau. "Analytical proof of the isospectrality of quasinormal modes for Schwarzschild-de Sitter and Schwarzschild-Anti de Sitter spacetimes". In: *Gen. Rel. Grav.* 52.8 (2020), p. 82. DOI: 10.1007/s10714-020-02737-4. arXiv: 1906.05633 [gr-qc].

[77] V. Cardoso, M. Cavaglia, and L. Gualtieri. "Hawking emission of gravitons in higher dimensions: Non-rotating black holes". In: *JHEP* 02 (2006), p. 021. DOI: 10.1088/1126-6708/2006/02/021. arXiv: hep-th/0512116.

[78] D. K. Park. "Emissivities for the various Graviton Modes in the Background of the Higher-Dimensional Black Hole". In: *Phys. Lett. B* 638 (2006), pp. 246–252. DOI: 10.1016/j.physletb.2006.05.043. arXiv: hep-th/0603224.

[79] D. N. Page. "Particle Emission Rates from a Black Hole. 3. Charged Leptons from a Nonrotating Hole". In: *Phys. Rev. D* 16 (1977), pp. 2402–2411. DOI: 10.1103/PhysRevD.16.2402.

[80] E. Jung and D. K. Park. "Validity of Emparan-Horowitz-Myers argument in Hawking radiation into massless spin-2 fields". In: *Mod. Phys. Lett. A* 22 (2007), pp. 1635–1642. DOI: 10.1142/S021773230702405X. arXiv: hep-th/0612043.

[81] R. C. Myers and M. J. Perry. "Black Holes in Higher Dimensional Space-Times". In: *Annals Phys.* 172 (1986), p. 304. DOI: 10.1016/0003-4916(86)90186-7.

[82] M. O. P. Sampaio. "Charge and mass effects on the evaporation of higher-dimensional rotating black holes". In: *JHEP* 10 (2009), p. 008. DOI: 10.1088/1126-6708/2009/10/008. arXiv: 0907.5107 [hep-th].

[83] E. Wasserstrom. "A new method for solving eigenvalue problems". In: *Journal of Computational Physics* 9.1 (1972), pp. 53–74.

[84] E. Berti, V. Cardoso, and M. Casals. "Eigenvalues and eigenfunctions of spin-weighted spheroidal harmonics in four and higher dimensions". In: *Phys. Rev. D* 73 (2006). [Erratum: Phys.Rev.D 73, 109902 (2006)], p. 024013. DOI: 10.1103/PhysRevD.73.109902. arXiv: gr-qc/0511111.

[85] S. Chandrasekhar. "On a Transformation of Teukolsky's Equation and the Electromagnetic Perturbations of the Kerr Black Hole". In: *"Proc. Roy. Soc. Lond. A"* 348 (1976), pp. 39–55. DOI: 10.1098/rspa.1976.0022.

[86] S. Chandrasekhar and S. L. Detweiler. "Equations governing gravitational perturbations of the Kerr black-hol e". In: *Proc. Roy. Soc. Lond. A* 350 (1976), pp. 165–174. DOI: 10.1098/rspa.1976.0101.

[87] S. Chandrasekhar and S. L. Detweiler. "On the Reflection and Transmission of Neutrino Waves by a Kerr Black Hole". In: *Proc. Roy. Soc. Lond. A* 352 (1977), pp. 325–338. DOI: 10.1098/rspa.1977.0002.

[88] G. Duffy, C. Harris, P. Kanti, and E. Winstanley. "Brane decay of a (4+n)-dimensional rotating black hole: Spin-0 particles". In: *JHEP* 09 (2005), p. 049. DOI: 10.1088/1126-6708/2005/09/049. arXiv: hep-th/0507274.

[89] M. Casals, P. Kanti, and E. Winstanley. "Brane decay of a (4+n)-dimensional rotating black hole. II. Spin-1 particles". In: *JHEP* 02 (2006), p. 051. DOI: 10.1088/1126-6708/2006/02/051. arXiv: hep-th/0511163.

[90] M. Casals, S. R. Dolan, P. Kanti, and E. Winstanley. "Brane Decay of a (4+n)-Dimensional Rotating Black Hole. III. Spin-1/2 particles". In: *JHEP* 03 (2007), p. 019. DOI: 10.1088/1126-6708/2007/03/019. arXiv: hep-th/0608193.

[91] M. Visser. "Some general bounds for 1-D scattering". In: *Phys. Rev. A* 59 (1999), pp. 427–438. DOI: 10.1103/PhysRevA.59.427. arXiv: quant-ph/9901030.

[92] A. Arbey, J. Auffinger, M. Geiller, E. R. Livine, and F. Sartini. "Hawking radiation by spherically-symmetric static black holes for all spins. II. Numerical emission rates, analytical limits, and new constraints". In: *Phys. Rev. D* 104.8 (2021), p. 084016. DOI: 10.1103/PhysRevD.104.084016. arXiv: 2107.03293 [gr-qc].

[93] *DØ*. "Search for large extra dimensions via single photon plus missing energy final states at $\sqrt{s} = 1.96$-TeV". In: *Phys. Rev. Lett.* 101 (2008), p. 011601. DOI: 10.1103/PhysRevLett.101.011601. arXiv: 0803.2137 [hep-ex].

[94] *ATLAS*. "Search for new phenomena in events with an energetic jet and missing transverse momentum in pp collisions at $\sqrt{s}$ =13 TeV with the ATLAS detector". In: *Phys. Rev. D* 103.11 (2021), p. 112006. DOI: 10.1103/PhysRevD.103.112006. arXiv: 2102.10874 [hep-ex].

Appendix A: Higher Dimensional Rotating Black Holes

For a single angular momentum parameter a, the general Myers-Perry metric describing the space-time around a higher dimensional rotating black hole becomes [81]

$$\begin{aligned} ds^2 &= -\left(1-\frac{\mu}{\Sigma r^{n-1}}\right)dt^2 - \frac{2a\mu\sin^2\theta}{\Sigma r^{n-1}}dtd\phi + \frac{\Sigma}{\Delta}dr^2 + \Sigma d\theta^2 \\ &\quad \left(r^2+a^2+\frac{a^2\mu\sin^2\theta}{\Sigma r^{n-1}}\right)\sin^2\theta d\phi^2 + r^2\cos^2\theta d\Omega_n^2, \end{aligned} \tag{A.1}$$

where $\Delta = r^2 + a^2 - \frac{\mu}{r^{n-1}}$, $\Sigma = r^2 + a^2\cos^2\theta$, $d\Omega_n^2$ is the metric of the (n)-dimensional unit sphere, and μ is a parameter related to the mass M of the black hole by

$$\mu = \frac{16\pi}{(n+2)A_{n+2}}M, \tag{A.2}$$

where A_{n+2} is the area of the $(n+2)$-dimensional unit sphere defined by

$$A_{n+2} = \frac{2\pi^{(n+3)/2}}{\Gamma[(n+3)/2]}, \tag{A.3}$$

and Γ is the gamma function. The horizon, $r_{\rm H}$ of the black hole is found from $\Delta(r_{\rm H}) = 0$ and can be written as:

$$r_{\rm H} = \frac{\mu}{(1+a_*^2)^{1/(n+1)}}, \tag{A.4}$$

where $a_* = a/r_{\rm H}$. The above metric reduces to the Schwarzschild-Tangherlini metric for $a = 0$ which is itself the higher dimensional extension of the Schwarzschild metric. For $n = 0$ we obtain the Kerr metric. To find the metric as seen by an observer on the brane, we again fix the extra angular coordinates to obtain [16]

$$\begin{aligned} ds^2 &= -\left(1-\frac{\mu}{\Sigma r^{n-1}}\right)dt^2 - \frac{2a\mu\sin^2\theta}{\Sigma r^{n-1}}dtd\phi + \frac{\Sigma}{\Delta}dr^2 + \Sigma d\theta^2 \\ &\quad \left(r^2+a^2+\frac{a^2\mu\sin^2\theta}{\Sigma r^{n-1}}\right)\sin^2\theta d\phi^2. \end{aligned} \tag{A.5}$$

It is important to note that while the Myers-Perry metric is a vacuum solution to the higher dimensional Einstein equations, the brane induced metric is not a solution to the four-dimensional vacuum Einstein equations [82].

The fundamental equations for massless spin 0, 1/2, 1 and 2 perturbations of a higher dimensional simply rotating black hole on the brane can be written as a single master equation [56]

$$\begin{aligned}&\left[\frac{(r^2+a^2)^2}{\Delta}-a^2\sin^2\theta\right]\frac{\partial^2\psi}{\partial t^2}+\frac{2a(r^2+a^2-\Delta)}{\Delta}\frac{\partial^2\psi}{\partial t\partial\phi}+\left[\frac{a^2}{\Delta}-\frac{1}{\sin^2\theta}\right]\frac{\partial^2\psi}{\partial\phi^2}\\&-\Delta^{-s}\frac{\partial}{\partial r}\left(\Delta^{s+1}\frac{\partial\psi}{\partial r}\right)-\frac{1}{\sin\theta}\frac{\partial}{\partial\theta}\left(\sin\theta\frac{\partial\psi}{\partial\theta}\right)-2s\left[\frac{a\Delta'}{2\Delta}+\frac{i\cos\theta}{\sin^2\theta}\right]\frac{\partial\psi}{\partial\phi}\\&+2s\left[\frac{2\Delta r-(r^2+a^2)\Delta'}{2\Delta}+r+ia\cos\theta\right]\frac{\partial\psi}{\partial t}+(s^2\cot^2\theta-s+s(2-\Delta''))\psi\\&=0.\end{aligned}\tag{A.6}$$

Similar to the spherically symmetric case, Eq. (A.6) can be separated by writing the ansatz

$$\psi_s=e^{-i\omega t}e^{im\phi}{}_sS^m_\ell(\theta)R_s(r),\tag{A.7}$$

where ${}_sS^m_\ell$ are the spin-weighted spheroidal harmonics [53]. We can now obtain a set of decoupled radial and angular equations [53]

$$\Delta^{-s}\frac{d}{dr}\left(\Delta^{s+1}\frac{dR_s}{dr}\right)+\left(\frac{K^2-isK\Delta'}{\Delta}+4is\omega r+s(\Delta''-2)-{}_s\lambda^m_l\right)R_s=0,\tag{A.8}$$

and

$$\begin{aligned}&\frac{1}{\sin\theta}\frac{d}{d\theta}\left(\sin\theta\frac{d_sS^m_l}{d\theta}\right)\\&+\left(a^2\omega^2\cos^2\theta-2a\omega s\cos\theta-\frac{m^2+s^2+2ms\cos\theta}{\sin^2\theta}+{}_s\lambda^m_\ell\right){}_sS^m_\ell=0,\end{aligned}\tag{A.9}$$

where $K=(r^2+a^2)\omega-am$. The radial and angular equations are related by the connection coefficient ${}_s\lambda^m_\ell={}_sE^m_\ell+a^2\omega^2-2am\omega$ where ${}_sE^m_\ell$ are the eigenvalues of the spheroidal harmonics obtained from the angular equation. For $a=0$, we have ${}_sE^m_\ell=\ell(\ell+1)-s(s+1)$. To calculate the greybody factors one needs to insert the eigenvalues from the angular equation into the radial equation and use the appropriate

boundary conditions to compute the transmission coefficients of the wave propagating from the horizon out to spatial infinity.

The angular equation can be written as an eigenvalue equation involving the sum of two operators [54]

$$(\mathfrak{H}_0 + \mathfrak{H}_1)S = -ES, \tag{A.10}$$

where

$$\mathfrak{H}_0 = \frac{1}{\sin\theta}\frac{d}{d\theta}\left(\sin\theta\frac{d}{d\theta}\right) - \left(\frac{m^2 + s^2 + 2ms\cos\theta}{\sin^2\theta}\right), \tag{A.11a}$$

$$\mathfrak{H}_1 = a^2\,\omega^2\cos^2\theta - 2a\,\omega\,s\cos\theta. \tag{A.11b}$$

In the case that $a\,\omega = 0$, we find that $\mathfrak{H}_1$ drops out and the solutions become the spin-weighted spherical harmonics with eigenvalues ${}_sE_\ell^m = \ell(\ell+1) - s(s+1)$ [54]. For $a\,\omega \neq 0$, we can treat $\mathfrak{H}_1$ as a perturbation operator which takes us from the spherical harmonics to the spheroidal harmonics [54]. Here, the eigenvalues are a function of $a\,\omega$ for which we do not have explicit analytic representations. For small $a\,\omega$, we can use perturbation theory to obtain

$${}_sE_\ell^m = \ell(\ell+1) - s(s+1) - \langle s\ell m|\mathfrak{H}_1|s\ell m\rangle + ..., \tag{A.12}$$

where we have

$$\langle s\ell' m|\mathfrak{H}_1|s\ell m\rangle = \int d\Omega({}_sY_{\ell'}^m)^*({}_sY_\ell^m)\mathfrak{H}_1, \tag{A.13}$$

and ${}_sY_\ell^m$ are the spin-weighted spherical harmonics which are related to the rotation matrix elements of quantum mechanics by the following useful identities

$$\langle s\ell' m|\cos^2\theta|s\ell m\rangle = \frac{1}{3}\delta_{\ell\ell'} + \frac{2}{3}\left(\frac{2\ell+1}{2\ell'+1}\right)^{1/2}\langle \ell m 20|\ell' m\rangle\langle \ell(-s)20|\ell'(-s)\rangle, \tag{A.14a}$$

$$\langle s\ell' m|\cos\theta|s\ell m\rangle = \left(\frac{2\ell+1}{2\ell'+1}\right)^{1/2}\langle \ell m 10|\ell' m\rangle\langle \ell(-s)10|\ell'(-s)\rangle. \tag{A.14b}$$

However we are mostly interested in arbitrarily large values of $a\,\omega$ over which the interesting physics occurs. For such cases, we employ the procedure introduced in Ref. [83] to solve for the eigenvalues numerically using a continuation method which is

an extension of the perturbation method for arbitrarily large values of $a\,\omega$ [54]. This is carried out by writing the spheroidal harmonics ${}_sS_\ell^m$ in the basis of the spherical harmonics ${}_sY_\ell^m$

$$ {}_sS_\ell^m(\theta, a\,\omega) = \sum_{\ell'} {}_sA_{\ell\ell'}(a\,\omega)\,{}_sY_\ell^m(\theta). \tag{A.15} $$

Differentiating Eq. (A.10) by $a\,\omega$ and applying techniques from perturbation theory, we obtain the following set of coupled differential equations:

$$ \frac{d_sA_{\ell\ell'}}{d(a\,\omega)} = -\sum_{\alpha,\beta,\gamma\neq\ell} \frac{{}_sA_{\gamma\alpha\,s}A_{\ell\beta}}{{}_sE_\ell^m - {}_sE_\gamma^m}\langle\alpha,\beta\rangle\,{}_sA_{\gamma\ell'}, \tag{A.16a} $$

$$ \frac{d_sE_\ell^m}{d(a\,\omega)} = -\sum_{\alpha,\beta} {}_sA_{\ell\alpha\,s}A_{\ell\beta}\langle\alpha,\beta\rangle, \tag{A.16b} $$

where $\langle\alpha,\beta\rangle$ is evaluated as

$$ \begin{aligned} \langle\alpha,\beta\rangle &= \left\langle s\alpha m\left|\frac{d\mathfrak{H}_1}{d(a\,\omega)}\right|s\beta m\right\rangle \\ &= 2a\,\omega\left(\frac{1}{3}\delta_{\alpha\beta} + \frac{2}{3}\left(\frac{2\beta+1}{2\alpha+1}\right)^{1/2}\langle\beta m20|\alpha m\rangle\langle\beta{-}s20|\alpha{-}s\rangle\right) \\ &\quad -2s\left(\left(\frac{2\beta+1}{2\alpha+1}\right)^{1/2}\langle\beta m10|\alpha m\rangle\langle\beta{-}s10|\alpha{-}s\rangle\right) \end{aligned} \tag{A.17} $$

and $\langle j_1m_1j_2m_2|JM\rangle$ is a Clebsch-Gordan coefficient. This set of coupled differential equations can be solved for each mode s, m to obtain the eigenvalues as a function of $a\,\omega$ for arbitrary values of ℓ. The initial conditions are

$$ {}_sA_{\ell\ell'}(0) = \delta_{\ell\ell'}, \tag{A.18a} $$

$$ {}_sE_\ell^m(0) = \ell(\ell+1) - s(s+1). \tag{A.18b} $$

We numerically integrate the system of coupled equations defined in Eq. (A.16) over the range $0 \leq a\,\omega \leq 3$ with a step-size of 10^{-2}. The size of the system is $N(N+1)$ where $N = \max(|m|,|s|) + \ell_{\max}$ and thus dependent on the number of modes of ℓ used. The system grows large very quickly, thus we truncate the summation over α, β, γ at $\ell = 6$ terms, at which point integration appeared to be stable.

In Figure A.1 we plot the first few ℓ modes for $s = 0$ and $m = 1$. We find them to be in good agreement with the sixth order polynomial expression given in Ref. [84] over the range $0 \leq a\,\omega \leq 3$. The polynomial expansion begins to show deviations from our numerical results near $a\,\omega = 3$ and cannot be used with accuracy for $a\,\omega > 3$. Our results also agree with those from Ref. [56].

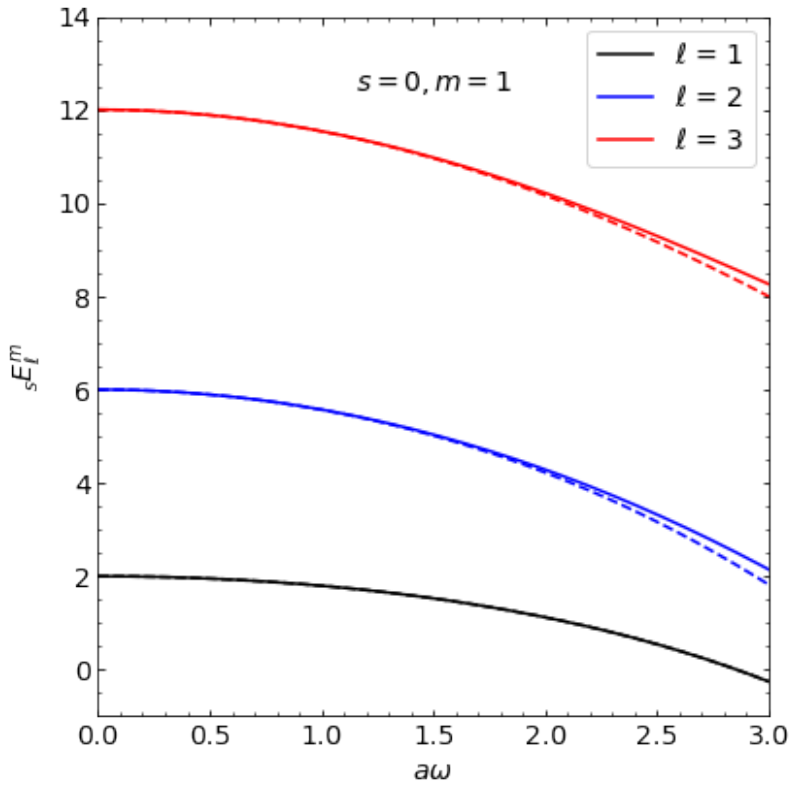

Figure A.1: Results of the numerical integration for the eigenvalues of the spin-weighted spheroidal harmonics for the first few ℓ modes for $s = 0$ and $m = 1$. The dashed lines offer a comparison with the sixth order polynomial expansion from Ref. [84].

In Figure A.2 we show the spheroidal harmonics for different values of $a\,\omega$ with $s = \ell = m = 0$.

Short-ranged Potentials

Short-ranged potentials in the rotating case are only known to exist in four dimensions and were found by Chandrasekhar [85–87]. The short-ranged potentials for spins 0,

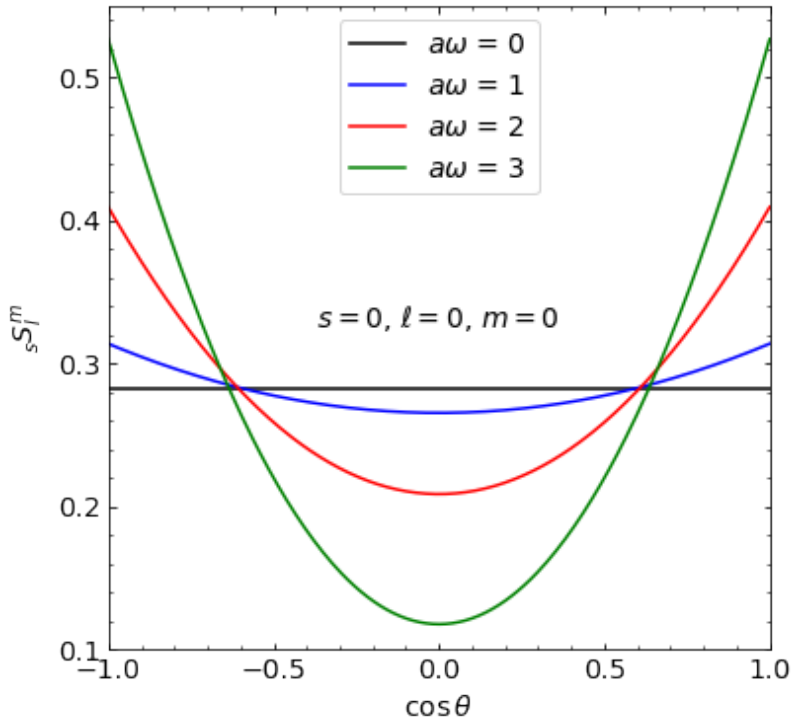

Figure A.2: Spheroidal harmonics for $s = \ell = m = 0$ for different values of $a\,\omega$

1/2, 1 and 2 are given as

$$V_0 = \frac{\Delta}{\rho^4}\left({}_0\lambda_\ell^m + \frac{\Delta + 2r(r-M)}{\rho^2} - \frac{3r^2\Delta}{\rho^4}\right), \tag{A.19a}$$

$$V_{1/2,\pm} = \frac{\Delta}{\rho^4}({}_{1/2}\lambda_\ell^m + 1) \mp \frac{\sqrt{({}_{1/2}\lambda_{\ell m}+1)\Delta}}{\rho^4}\left((r-M) - \frac{2r\Delta}{\rho^2}\right), \tag{A.19b}$$

$$V_{1,\pm} = \frac{\Delta}{\rho^4}\left({}_1\lambda_\ell^m + 2 - \alpha^2\frac{\Delta}{\rho^4} \mp i\alpha\rho^2\frac{d}{dr}\left(\frac{\Delta}{\rho^4}\right)\right), \tag{A.19c}$$

$$\begin{aligned} V_2 = \frac{\Delta}{\rho^8}\Bigg(& q - \frac{\rho^2}{(q-\beta\Delta)^2}(q-\beta\Delta)(\rho^2\Delta q'' - 2\rho^2 q - 2r(q'\Delta - \Delta' q)) \\ &+ \rho^2(\kappa\rho^2 - q' + \beta\Delta')(q'\Delta - \Delta' q)\Bigg), \end{aligned} \tag{A.19d}$$

where $q = \nu_2\rho^4 + 3\rho^2(r^2 - a^2) - 3r^2\Delta$, $\beta_\pm = \pm 3\alpha^2$,
$\kappa_\pm = \pm\sqrt{36M^2 - 2\nu_2(\alpha^2(5\nu_2+6) - 12a^2) + 2\beta\nu_2(\nu_2+2)}$ and $\nu_2 = {}_2\lambda_\ell^m + 4$. It should be noted that these potentials contain a dependence on ω through the connection coefficient ${}_s\lambda_\ell^m$. Here, the tortoise coordinate is defined as

$$\frac{dr_*}{dr} = \frac{\rho^2}{\Delta}, \tag{A.20}$$

where $\rho^2 = r^2 + a^2 - \frac{am}{w}$. These transformations do not easily extend to the higher dimensional rotating case. As a result, Eq. (A.8) must be integrated directly for $n > 0$. Details for dealing with such cases are given in Refs. [16, 88–90].

Numerical Methods

The transfer matrix method developed by Grey and Visser [70] cannot be used to compute greybody factors for rotating black holes in the formulation that we described in Chapter 3. Extending the method to the rotating case is non-trivial, for further details see Ref. [91].

Here, we will adopt the approach described by Chandrasekhar [66]. The radial equation given by Eq. (3.13) is a second order differential equation which can be broken up into a system of coupled first order differential equations

$$\frac{dZ(r_*)}{dr_*} = U(r_*), \tag{A.21}$$

and

$$\frac{dU(r_*)}{dr_*} = (V(r(r_*)) - \omega^2)Z(r_*). \tag{A.22}$$

We start with a plane wave at the horizon of the form $Z(r_*(r_{\rm H})) = e^{-i\,\omega\, r_*(r_{\rm H})}$, and integrate Eqs (A.21) and (A.22) out to infinity where the solution has the form

$$Z(r_*) = B_{\rm in} e^{-i\,\omega\, r_*} + B_{\rm out} e^{i\,\omega\, r_*}, \tag{A.23}$$

and $B_{\rm in}$ and $B_{\rm out}$ are complex coefficients. We solve for $B_{\rm in}$ and $B_{\rm out}$ in terms of the solutions at infinity by

$$B_{\rm in} = \left[\frac{1}{2e^{-i\,\omega\, r_*}}\left(Z(r_*) - \frac{U(r_*)}{i\,\omega}\right)\right]\Bigg|_{r_*=\infty}, \tag{A.24}$$

and

$$B_{\rm out} = \left[\frac{1}{2e^{i\,\omega\, r_*}}\left(Z(r_*) + \frac{U(r_*)}{i\,\omega}\right)\right]\Bigg|_{r_*=\infty}. \tag{A.25}$$

The transmission coefficient $\Gamma_{s\ell m}(\omega)$ is computed as

$$\Gamma_{s\ell m}(\omega) = 1 - \left|\frac{B_{\rm out}}{B_{\rm in}}\right|^2. \tag{A.26}$$

Results of Numerical Computations

The eigenvalues were interpolated by an interpolating polynomial of degree 6 and inserted into the short ranged potentials in Eq. (A.19a). The transmission coefficients were obtained for various values of a_* by numerically integrating Eq. (3.13) for values of $0.001 \leq \omega\, r_{\rm H} \leq 1$. We begin with the solution near the horizon at $r_{\rm H} + \epsilon$ where $\epsilon \sim 10^{-16}$ and integrate out to a large value of $r_* = 350$ approximating spatial infinity. We achieve sufficient convergence using a step size of 0.01. As a representative example, in Figure A.3 we show the spin 0 transmission coefficients as a function of frequency for different ℓ and m modes and for $a_* = 0.5$.

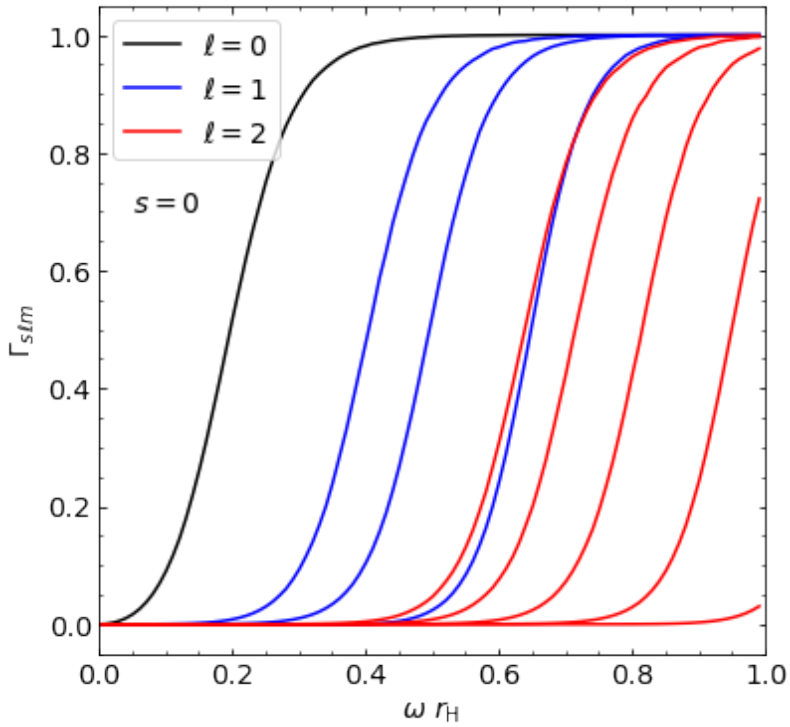

Figure A.3: Transmission coefficients $\Gamma_{s\ell m}(\omega)$ as a function of the frequency ω for $s = 0$ and $a_* = 0.5$ with $r_{\rm H} = 1$. For a given mode ℓ, the quantum number m increases from $m = -\ell$ to $m = \ell$ moving from left to right.

Since rotating black holes lose their spherical symmetry and are only axially symmetric, the transmission coefficients are different for each of the $2\ell + 1$ values of m. There is an observed spreading of the transmission coefficients for different values of

m centred around the transmission coefficient corresponding to $m = 0$. For a given value of ℓ, the value of m increases from $-\ell$ to ℓ moving from left to right.

An interesting property of rotating black holes is the effect of superradiance, where the transmission coefficient becomes negative corresponding to the amplification of a reflected wave [66]. Superradiance occurs for $\omega\, r_{\rm H} < m\Omega_{\rm H}$ where $\Omega_{\rm H} = a/(r_{\rm H}^2 + a^2)$ is the angular velocity of the horizon. In Figure A.4 we show a few of the superradiant modes for $s = 0$ and $a_* = 0.5$ versus frequency normalized to the superradiant regime. We compute the energy amplification as $(1 - \Gamma_{s\ell m}(\omega)) \times 100\%$ [56].

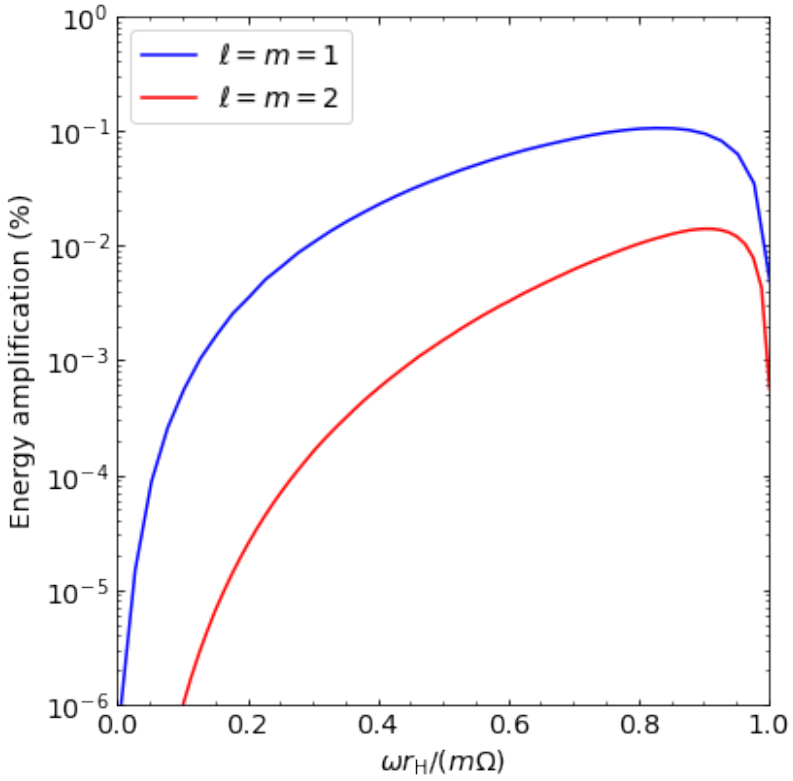

Figure A.4: Superradiant amplification of some spin 0 modes for $a_* = 0.5$ and with $r_{\rm H} = 1$.

Appendix B: Tortoise Coordinate

For a spherically symmetric metric with time-radius symmetry, such as the one given in Eq. (2.7), the tortoise coordinate is defined as

$$\frac{dr_*}{dr} = \frac{1}{h(r)}. \tag{B.1}$$

It turns out the for the Schwarzschild Tangherlini case, with the metric function $h_{ST}(r)$ is defined as

$$h_{ST}(r) = 1 - \frac{1}{k_n}\frac{M}{M_D}\frac{1}{(M_D r)^{n+1}}, \tag{B.2}$$

Eq. (B.1) can be integrated analytically for any n. The form of $r_{*ST,n}(r)$ is given in Ref. [92] for $0 \leq n \leq 6$. The tortoise coordinate takes on the following form for which we also provide the $n = 7$ case

$$\frac{r_{*ST,0}}{r_{\rm H}} = x + \ln x - 1, \tag{B.3a}$$

$$\frac{r_{ST,1}}{r_{\rm H}} = x + \frac{1}{2}\ln\frac{x-1}{x+1}, \tag{B.3b}$$

$$\frac{r_{*ST,2}}{r_{\rm H}} = x + \frac{1}{3}\ln x - 1 + \frac{1}{\sqrt{3}}\arctan\frac{\sqrt{3}}{1+2x} - \frac{1}{6}\ln x^2 + x + 1, \tag{B.3c}$$

$$\frac{r_{*ST,3}}{r_{\rm H}} = x + \frac{1}{4}\ln\frac{x-1}{x+1} + \frac{1}{2}\arctan\frac{1}{x}, \tag{B.3d}$$

$$\begin{aligned}\frac{r_{*ST,4}}{r_{\rm H}} = {} & x + \frac{1}{5}\ln x - 1 + \frac{1}{5^{-3/4}}\sqrt{\frac{1+\sqrt{5}}{2}}\arctan\frac{\sqrt{5+\sqrt{5}}/2}{2x+(1-\sqrt{5})/2} \\ & + \sqrt{\frac{\sqrt{5}-1}{2}}\arctan\frac{\sqrt{5-\sqrt{5}}/2}{2x+(1+\sqrt{5})/2} - \frac{1}{10}\left(\frac{1-\sqrt{5}}{2}\ln x^2 + \frac{1-\sqrt{5}}{2}x + 1\right. \\ & \left. + \frac{1+\sqrt{5}}{2}\ln x^2 + \frac{1+\sqrt{5}}{2}x + 1\right),\end{aligned} \tag{B.3e}$$

$$\frac{r_{*ST,5}}{r_{\rm H}} = x+\frac{1}{6}\ln\frac{x-1}{x+1}+\frac{1}{2\sqrt{3}}\left(\arctan\frac{\sqrt{3}}{2x+1}+\arctan\frac{\sqrt{3}}{2x-1}\right) + \frac{1}{12}\ln\frac{x^2-x+1}{x^2+x+1}, \tag{B.3f}$$

$$\begin{aligned}\frac{r_{*ST,6}}{r_{\rm H}} = {} & \frac{1}{7}\ln x - 1 + \frac{2}{7}\left(\cos\frac{\pi}{14}\arctan\frac{\cos\frac{\pi}{14}}{x+\sin\frac{\pi}{14}}+\cos\frac{3\pi}{14}\arctan\frac{\cos\frac{3\pi}{14}}{x-\sin\frac{3\pi}{14}}\right. \\ & \left.+\sin\frac{\pi}{7}\arctan\frac{\sin\frac{\pi}{7}}{x+\cos\frac{\pi}{7}}+\cos\frac{\pi}{14}\arctan\frac{\cos\frac{\pi}{14}}{x+\sin\frac{\pi}{14}}\right) \\ & +\frac{1}{7}\left(\sin\frac{3\pi}{14}\ln x^2-2\sin\frac{3\pi}{14}x+1-\sin\frac{\pi}{14}\ln x^2+2\sin\frac{\pi}{14}x+1\right. \\ & \left.-\cos\frac{\pi}{7}\ln x^2+2\cos\frac{3\pi}{7}x+1\right),\end{aligned} \tag{B.3g}$$

$$\begin{aligned}\frac{r_{*ST,7}}{r_{\rm H}} = {} & x+\frac{1}{16}\left[\sqrt{2}\ln\frac{x^2-\sqrt{2}x+1}{x^2+\sqrt{2}x+1}+2\ln\frac{x-1}{x+1}-4\arctan x\right. \\ & \left.-2\sqrt{2}\arctan\frac{x^2-1}{\sqrt{2}x}\right],\end{aligned} \tag{B.3h}$$

where we defined $x = r/r_{\rm H}$ with $r_{\rm H}$ being the horizon radius of the ST black hole.

Appendix C: Experimental Constraints

The experimental lower bounds on M_D and the maximum energy of the LHC will restrict the values of $\sqrt{\theta}$ that can be probed by experiments at the LHC. We do not expect black holes to form for masses much less than M_D. This gives a lower bound on M. We will consider only the hard limits on the Planck scale set by accelerator experiments [93, 94]: $M_D > 11.2$ TeV for $n = 2$, $M_D > 8.5$ TeV for $n = 3$, $M_D > 7.1$ TeV for $n = 4$, $M_D > 6.4$ TeV for $n = 5$, $M_D > 5.9$ TeV for $n = 6$, and $M_D > 0.8$ TeV for $n = 7$. The maximum mass of the black hole is likely to be limited by the statistics of the maximum parton energies in a proton-proton interaction but in no case can it be larger than the proton-proton centre-of-mass energy. Thus, we will only be interested in the case where the minimum black hole mass is below the LHC current maximum energy of 13.6 TeV and above the experimental lower bound on the Planck scale.

We obtain a valid range of $\sqrt{\theta}M_D$ for each number of extra dimensions by restricting the minimum black hole mass at the LHC to be in the range $1 < M_{\min}/M_D < 13.6\ \text{TeV}/M_D$, as discussed above. The results are given in Table C.1 and were computed by Doug Gingrich. We see that $\sqrt{\theta}$ is very restricted and there is no single value of $\sqrt{\theta}$ that lies in the allowed range for all number of extra dimensions.

To study the phenomenology of NC inspired black holes at the LHC experiments one can take M_D above the experimental limits and the following values $\sqrt{\theta} = 0.3$ for $n = 2$, $\sqrt{\theta} = 0.4$ for $n = 3$, $\sqrt{\theta} = 0.5$ for $n = 4$, $\sqrt{\theta} = 0.6$ for $n = 5$, $\sqrt{\theta} = 0.7$ for

Table C.1: Values of minimum horizon radius $(r_{\rm H})_{\rm min}$ in units of $\sqrt{\theta}$ and minimum mass $M_{\rm min}$ in units of $M_D(\sqrt{\theta}M_D)^{n+1}$. The last two columns show the range of $\sqrt{\theta}$ in units of $1/M_D$ that can be probed at the Large Hadron Collider.

n	$(r_{\rm H})_{\rm min}/\sqrt{\theta}$	$\frac{M_{\rm min}/M_D}{(\sqrt{\theta}M_D)^{n+1}}$	$\sqrt{\theta_{\rm min}}M_D$	$\sqrt{\theta_{\rm max}}M_D$
0	3.02	47.9		
1	2.68	63.2		
2	2.51	65.2	0.248	0.265
3	2.41	58.8	0.361	0.406
4	2.34	48.6	0.460	0.524
5	2.29	37.9	0.546	0.619
6	2.26	28.2	0.621	0.699
7	2.23	20.3	0.686	0.978

$n = 6$, and $\sqrt{\theta} = 0.8$ for $n = 7$.